Strong coupling effects and nonlinear dynamics in a THz-EIT metamaterial

By

Amit Haldar

PHYS11202104019

National Institute of Science Education and Research, Bhubaneswar

A thesis submitted to the

Board of Studies in Physical Sciences

in partial fulfillment of requirements

for the Degree of

DOCTOR OF PHILOSOPHY

of

HOMI BHABHA NATIONAL INSTITUTE

August, 2026

Homi Bhabha National Institute[1]

Recommendations of the Viva Voce Board

As members of the Viva Voce Board, we certify that we have read the dissertation prepared by **Amit Haldar** entitled **"Strong coupling effects and nonlinear dynamics in a THz-EIT metamaterial"** and recommend that it may be accepted as fulfilling the thesis requirement for the award of Degree of Doctor of Philosophy.

S. N.	Composition	Name	Signature with date	In-Person/ Online
1.	Chairman	Prof. Tapan Mishra	Tapan Mishra	In-person
2.	Guide/Convener	Prof. Shovon Pal	Shovon Pal 17/08/26	In-person.
3.	Co-Guide (if any)			
4.	Examiner	Prof. Sunil Kumar	17/08	In person
5.	Member - 1	Prof. Satyaprasad P Senanayak	Satya. Prasad	In Person
6.	Member - 2	Prof. Kush Saha	KSaha	In-person
7.	Member - 3	Prof. Shriganesh Prabhu	17/08/2026	Online
8.	Technology Advisor (if any)			

Final approval and acceptance of this thesis is contingent upon the candidate's submission of the final copies of the thesis to HBNI.

I/We hereby certify that I/we have read this thesis prepared under my/our direction and recommend that it may be accepted as fulfilling the thesis requirement.

Date: 17/08/2026

Place: NISER

Signature
Co-guide (if any)

Shovon Pal

Signature
Guide

[1] This page is to be included only for final submission after successful completion of viva voce.

STATEMENT BY AUTHOR

This dissertation has been submitted in partial fulfillment of requirements for an advanced degree at Homi Bhabha National Institute (HBNI) and is deposited in the Library to be made available to borrowers under rules of the HBNI.

Brief quotations from this dissertation are allowable without special permission, provided that accurate acknowledgement of source is made. Requests for permission for extended quotation from or reproduction of this manuscript in whole or in part may be granted by the Competent Authority of HBNI when in his or her judgment the proposed use of the material is in the interests of scholarship. In all other instances, however, permission must be obtained from the author.

Amit Haldar 17/08/25

Amit Haldar

DECLARATION

I, hereby declare that the investigation presented in the thesis has been carried out by me. The work is original and has not been submitted earlier as a whole or in part for a degree / diploma at this or any other Institution / University.

Amit Haldar 17/08/26

Amit Haldar

CERTIFICATION ON ACADEMIC INTEGRITY

Undertaking by the Student:

1. I, Amit Haldar, HBNI Enrolment No. PHYS11202104019 hereby undertake that the Thesis, titled "Strong coupling effects and nonlinear dynamics in a THz-EIT meta-material" is prepared by me and is the original work undertaken by me.

2. I also hereby undertake that this document has been duly checked through a plagiarism detection tool and the document is found to be plagiarism free as per the guidelines of the Institute/UGC.

3. I am aware and undertake that if plagiarism is detected in my thesis at any stage in the future, suitable penalty will be imposed as applicable as per the guidelines of the Institute/UGC.

Amit Haldar 17/08/26

Amit Haldar

Endorsed by the Thesis Supervisor:

I certify that the thesis written by the Researcher is plagiarism free as mentioned above by the student.

Signature of the Thesis Supervisor with date 17/8/2026

Name : Dr. Shovon Pal

Designation : Reader - F

Department/ Centre : School of Physical Sciences

Name of the CI/ OCC : National Institute of Science Education and Research

List of Publications arising from the thesis

Publications/Preprints

1. "Phonon-polariton mediated dual electromagnetically induced transparency-like response in a THz metamaterial", **Amit Haldar***, Kshitij V Goyal*, Ruturaj V Puranik, Vivek Dwij, Srijan Maity, Kanha Ram Khator, Subhashis Ghosh, Bhagwat S Chouhan, Gagan Kumar, Satyaprasad P Senanayak, Shriganesh Prabhu, and Shovon Pal, Adv. Quantum Technol., **2026**, 9, e00368. * equal contribution

2. "Unveiling nonlinearities of electromagnetically induced transparency in a THz metamaterial", **Amit Haldar**, Shriganesh Prabhu, and Shovon Pal, Adv. Funct. Mater., **2026**, e75422.

Conferences

1. Ultrafast Sciences (UFS) 2022
   November 3-5, 2022; IISER Trivandrum, India

2. IFCFPM 2023
   April 20-22, 2023; Mahindra University Hyderabad, India

3. Quantum Materials (QMAT) 2023
   November 27-30, 2023; NISER Bhubaneswar, India

4. Frontiers in Optics Laser Science (FIO+LS) 2024
   September 23-26, 2024; Denver, USA

5. HyPe 2024
   December 19-22, 2024; NISER Bhubaneswar, India

6. Career Accelerator Program 2025
   February 16-20, 2025; Washington, USA

7. MRS Fall Meeting & Exhibit 2025
   November 30-December 5, 2025; Boston, USA

8. SIS-II 2025
   November 20-22, 2025; NISER Bhubaneswar, India

9. MRSI-ICEM 2025
   December 17-20, 2025; NISER Bhubaneswar, India

Other Publications/Preprints

1. "Enhanced femtosecond nonlinear optical susceptibility and terahertz conductivity in $MoSe_2$-noble metal nanocomposites", Koushik Mondal, **Amit Haldar**, Ashim Pramanik, Rashbihari Layek, Dipanjan Banerjee, Venugopal Rao Soma, Shovon Pal, and Pathik Kumbhakar, Adv. Optical Mater., **2024**, 12, 2401138.

2. "2D-THz spectroscopy: exploring the nonlinear dynamics in quantum materials", Arpita Dutta, Payel Shee, **Amit Haldar**, and Shovon Pal, J. Phys.: Condens. Matter, **2025**, 37, 203002.

3. "Structural reorganization drives exciton relaxation pathways in layered 2D Ruddlesden Popper (RP) perovskite BA_2PbI_4", Boddeda Sai Kumar, Bikram Pal, Yedukondalu Potla, **Amit Haldar**, Mousumi Upadhyay Kahaly, Gergely Ferenc Samu, Amit S Pawbake, Shovon Pal, Soumen Ghosh, Sunil Suresh, and Sachin R. Rondiya, Small, **2025**, e09142.

4. "Nanoscale facet engineering stabilizes α-$FAPbI_3$ and suppresses ion migration to realize ambient stable perovskite transistors", Kanha Ram Khator, Debopam Acharejee, **Amit Haldar**, Devamrutha I S, Koushik Mondal, Asit Baran Mahato, Shovon Pal, Subhadip Ghosh, and Satyaprasad P Senanayak, Small, **2026**, e00022.

5. "Intensity-driven Mott-like transition in a 2D Ruddlesden-Popper perovskite", Koushik Mondal, **Amit Haldar**, Indrajit Mondal, Arpita Dutta, Himanshu Bhatt, Biswajit Mahata, Soumili Banerjee, Hirendra Nath Ghosh, Satyaprasad P Senanayak, and Shovon Pal, (Under review in Small).

Amit Haldar

Name & Signature of the Student

To my beloved parents

and in loving memory of my late uncle,

Sujit Haldar

ACKNOWLEDGEMENTS

"*In this path, no effort is ever lost, and no obstacle prevails. Even a little progress on this path protects one from great fear.*" *– Bhagavad Gita 2.40*

This dissertation reflects nearly five years of my journey – a path that often felt like climbing a steep peak, one step at a time, without always knowing what lay ahead. There were moments of doubt and exhaustion, but also moments of clarity and encouragement that kept me going. It was not an easy journey, but it has changed me in ways I will carry forward in life. It is difficult to fully express my gratitude to all those who have been part of this journey. In times when I felt lost, their support and belief helped me move forward. I sincerely thank everyone who stood by me and made this possible.

First and foremost, I would like to thank my thesis supervisor, Prof. Shovon Pal, for exposing me to a very exciting and interesting field of research. I am very thankful to Shovon Da for his constant guidance in scientific discussions, experimental work, and writing, as well as for his support in developing communication skills and creating a positive environment for growth in the UTHD lab. I also recall his words on my first day, which, in hindsight, reflect the demanding yet transformative nature of the research journey. I am truly thankful to him for guiding me through this process, which has significantly shaped my approach to research and learning.

I am sincerely thankful to Prof. Shriganesh Prabhu for providing me the opportunity to carry out experiments in his lab, and for his valuable inputs and guidance during my PhD. I also thank Prof. Satyaprasad P. Senanayak for granting access to his lab facilities for the thermal vapor deposition of the metamaterials, and for his support as a member of my doctoral committee.

I am grateful to my doctoral committee members, Prof. Kush Saha and Prof. Tapan Mishra (Chairman), for their guidance and helpful discussions. I would like to particularly thank Prof. Kush Saha for his insightful theoretical inputs, which greatly helped to shape my understanding of the work. I also thank Prof. Ritwick Das, my previous committee chairman, for his valuable suggestions during the earlier stages of my PhD.

I am thankful to all my collaborators for their contributions and discussions, which

have enriched this work. I also gratefully acknowledge the Department of Atomic Energy, Government of India, for financial support, and thank the Homi Bhabha National Institute and the National Institute of Science Education and Research (NISER) for providing the necessary platform and resources.

I would like to sincerely thank my mentor, Dr. Ranjana R. Das, for her constant support and guidance throughout my PhD journey and beyond. From the very beginning, Ranjana Di stood by me, especially during the initial days when I often felt confused, exhausted, and unsure of myself. She patiently guided me and helped me move forward. Her support was never limited to academics; she was always there with both professional and personal advice whenever needed. One of the most valuable lessons I learned from her is to stay positive even in difficult situations beyond my control. Thank you, Didi, for your guidance, encouragement, and for always believing in me.

I would like to express my heartfelt thanks to Payel Shee and Arpita Dutta for their constant support and encouragement throughout this journey, and for always being there when I needed it the most.

I would like to especially thank Arpita, whose cheerful and lively nature brought a unique energy to our group. Her spontaneous and often unintentionally humorous remarks, along with her enthusiastic attempts to learn Hindi, created many light-hearted and memorable moments in the UTHD lab. Beyond that, her kindness and genuine nature have always stood out. I have learned many things from her, and her simplicity and childlike enthusiasm make her truly special to me, like a younger sister.

I would also like to especially thank Payel for her constant support and friendship throughout this journey. She has been one of the few people with whom I could share things freely, and I deeply value the trust we share. Her lively and sometimes mischievous nature brought many light-hearted moments to the UTHD lab, adding warmth to this journey. I admire her confidence in handling both personal and professional challenges, and I am truly grateful for her support and companionship.

I would also like to thank all the members of the UTHD lab, from seniors to juniors, for their support, discussions, and for creating a friendly and motivating environment throughout my PhD. I am especially grateful to Dr. Koushik Mondal, Debankit Priyadarshi, Ashish

Panigrahi, Jyotiprakash Satapathy, Aditi Pradhan, Kshitij V Goyal, Swosti Prakash Sarangi, Nainish Tickoo, Swayam Panda, Monalisa Pattanaik, Biswajit Mahata, Soumili Banerjee, Soumya Prakash Jena, Srijan Maity, Subham Mandal, Mousumi Sarkar, and Sushmita Raj for their help, encouragement, and the many interactions that made the journey more enjoyable.

I would also like to thank Mr. Arun Kumar PR, the laser engineer, for his technical support and assistance with the laser system, which was essential for carrying out the experiments. I am equally grateful to the workshop staff, especially Umakant Bhaiya and Basudev Bhaiya, for their help and kind support.

I am fortunate to have made many good friends and batchmates during this journey, including Sagnik Misra, Dr. Debopam Acharjee, Dr. Manas Debnath, Dr. Akash Dey, Sayan Gupta, Kanha Ram Khator, Md. Tousif Alam, Mahadeb Dey, Ayan Nanda, Soham Mondal, Nandini Mondal, Debashree Nayak, Radhamadhab Chandra, and Indrajit Mondal, whose support and companionship made this experience more enjoyable.

I would like to thank my childhood friend and my college friends from my B.Sc and M.Sc days, Dipon Sutradhar, Prokash Das, Sanatan Halder, Firoz Alam, Salini Dutta, Meghasree Basu, Santosh Roy, Dr. Amlan Chakraborty, Arvind Agrahari and Dr. Debamalya Dutta, along with the friends I met along the way, for their continued support and friendship throughout this journey.

Last but not least, words are not enough to express my gratitude to my family, especially my father, Jogeshwar Haldar, and my mother, Jogmaya Haldar, who have always stood by me, even from miles away. I also remember my late uncle, Sujit Haldar, with deep respect and gratitude for his support and blessings. I am equally thankful to my sisters, Sipra Haldar, Shikha Haldar, and Dipika Haldar, for their constant encouragement and support throughout this journey. Whatever I am today is because of their unconditional love, care, guidance, encouragement, and constant support. In many ways, this journey would not have been possible without their sacrifices.

Lastly, if I have missed anyone here, it was my memory that failed, never my gratitude. Thank you all.

ABSTRACT

The interaction of electromagnetic radiation with matter is central to modern physics and underpins a wide range of technologies, from spectroscopy and sensing to communication and quantum information processing. While the optical and microwave frequency regimes have been extensively explored, the terahertz (THz) spectral range offers unique access to low-energy excitations such as phonons, collective charge dynamics, superconducting gaps, and other many-body phenomena that remain difficult to probe using conventional techniques. Despite major advances in ultrafast THz spectroscopy, achieving strong, coherent, and tunable THz light-matter interaction remains challenging due to weak intrinsic dipole coupling, poor field confinement, dissipative losses, short coherence times, and limited tunability in natural materials.

In this thesis, these challenges are addressed using artificially engineered THz metamaterials that enable tailored resonances, strong field confinement, and interference-based control of light-matter interactions. Electromagnetically induced transparency (EIT)-*like* responses are investigated in metamaterial systems where destructive interference between a radiative bright mode and a weakly radiative dark mode produces a narrow transparency window. The work extends beyond conventional EIT metamaterials by introducing strong coupling between the EIT resonances and phonon modes, leading to the formation of hybrid phonon-polariton states.

A hybrid system consisting of a THz-EIT metamaterial integrated with a phonon-active $MAPbI_3$ perovskite layer is developed and characterized. Strong coupling between the metamaterial resonances and the perovskite phonon mode is demonstrated through clear avoided crossings and Rabi splitting in the transmission spectra, with an interaction potential of $V = 0.538\,\text{meV}$ exceeding the dissipative strong coupling threshold of $V_{\text{st}} = 0.294\,\text{meV}$. Rabi splittings of 0.26 THz are observed for the SRR-phonon subsystem, and the original transparency window at 1.3 THz splits into two distinct transparency peaks near 0.9 THz and 1.2 THz. This hybridization fundamentally reshapes the interference pathways responsible for transparency, replacing a single window with a dual EIT-*like* response originating from interference between hybridized upper and lower polaritonic modes rather than from purely geometric resonances. Rotational and translational tunability of the structure

further enables reversible switching between the dual-EIT and conventional Rabi splitting regimes without any modification to the device geometry.

To uncover the dynamical origin of the original transparency window, two-dimensional coherent THz spectroscopy is applied to the EIT metamaterial. This phase-resolved technique provides direct access to the coupled resonator dynamics through pump-probe and photon-echo signals. From the temporal decay of the pump-probe signal, a bright-mode population relaxation time of $T_1 = 1.96\,\text{ps}$ is extracted. From the oscillatory decay of the photon-echo signal, a phase coherence lifetime of $T_2 = 1.0\,\text{ps}$ is determined. The inequality $T_2 < 2T_1$ indicates the presence of pure dephasing with $T_\varphi = 1.34\,\text{ps}$, primarily attributed to structural inhomogeneity arising from lithographic dimensional variations across the fabricated array. These results establish that inter-mode coherence between the bright and dark resonator modes persists on the picosecond timescale but decays faster than energy relaxation. The multi-peak structure of the photon-echo signal in the 2D frequency domain directly visualizes the dressed-state doublet underlying the EIT window and enables a quantitative separation of homogeneous and inhomogeneous broadening contributions, identifying structural disorder as the dominant limit on EIT linewidth in lithographically fabricated metamaterials.

The thesis establishes a unified framework linking spectral interference, strong coupling, and ultrafast coherence dynamics in THz metamaterials, and demonstrates that the coherence quality of EIT metamaterials is directly measurable and addressable through controlled fabrication improvements.

Contents

List of Figures

List of Tables

List of acronyms

2D-THz	Two-Dimensional THz Spectroscopy
Al	Aluminum
BPD	Balanced Photodiode
CAD	Computer-Aided Design
CCO	Conventional Coupled Oscillator
CST	Computer Simulation Technology
CW	Continuous Wave
DC	Direct Current
DFG	Difference-Frequency Generation
DMF	Dimethylformamide
DMSO	Dimethyl Sulfoxide
DNG	Double Negative Medium
ECO	Extended Coupled Oscillator
EIT	Electromagnetically Induced Transparency
EM	Electromagnetic
EO	Electro-Optic
EOS	Electro-Optic Sampling
FDTD	Finite Difference Time Domain
FFT	Fast Fourier Transformation
FID	Free Induction Decay
FIT	Finite Integration Technique
HWHM	Half-Width at Half-Maximum

IR	Infrared
LO	Longitudinal Optical
LP	Lower Polariton
MAI	Methylammonium Iodide
$MAPbI_3$	Methylammonium Lead Iodide
MM	Metamaterial
NMP	N-Methyl-2-Pyrrolidone
OPTP	Optical Pump THz Probe
OR	Optical Rectification
PTFE	Polytetrafluoroethylene
QCL	Quantum Cascade Laser
QED	Quantum Electrodynamics
QME	Quantum Master Equation
RWA	Rotating-Wave Approximation
SFG	Sum-Frequency Generation
SHG	Second-Harmonic Generation
SRR	Split-Ring Resonator
THz	Terahertz
THz-TDS	Terahertz Time-Domain Spectroscopy
Ti:Sa	Titanium-Sapphire
TO	Transverse Optical
UP	Upper Polariton
ZnTe	Zinc Telluride

Chapter 1

Introduction

The interaction of light with matter is one of the most consequential subjects in modern physics. It underpins quantum optics, drives the development of photonic technologies, and continues to reveal unexpected phenomena even in systems that appear well understood [1–4]. Among the most striking of these surprises is electromagnetically induced transparency (EIT) [5,6]. A medium that should absorb a probe beam completely is made transparent, not by removing the absorbing transition, but by adding a second coherent field that forces two excitation pathways into destructive interference. The absorption vanishes. In its place, the medium acquires a sharp dispersion that slows light dramatically [7, 8], enhances nonlinear interactions [9], and enables coherent storage [10] and retrieval of optical information [11, 12]. These properties have made EIT a cornerstone of quantum memory [12], precision spectroscopy, and slow-light [7, 8] research for decades. Yet the conditions required to observe it in atomic systems are severe. Ultracold temperatures, phase-locked control fields tuned to exact atomic transitions, and near-perfect isolation from environmental noise are all necessary [13, 14]. This has sustained a long-standing question: how much of this physics survives when the atomic system is replaced by something simpler and more accessible?

It turns out that the essential mechanism does survive. The destructive interference underlying EIT can be reproduced in classical coupled resonator systems, though the underlying physics differs from true quantum coherence in atomic vapors. What is needed is not a set of quantized energy levels but two coupled excitation pathways with different radiative characters, one that couples strongly to the incident field and one that does not. In a metamaterial, a metallic rod resonator plays the role of the radiative bright mode, coupling directly

to the incident terahertz (THz) pulse and absorbing broadly. A pair of split-ring resonators (SRRs) placed nearby acts as the dark mode, shielded from direct excitation by structural symmetry [15]. The near-field of the rod drives the dark mode indirectly, and the interference between the two responses opens a transparency window in the THz transmittance spectrum. The window can be positioned and shaped by lithographic design alone, without requiring any specific atomic transition or cryogenic environment. Nevertheless, despite the classical nature of the interference, the formal analogy with the three-level atomic system is close enough that the density matrix formalism provides a useful and quantitatively accurate framework for describing the coupled resonator dynamics, as demonstrated in Chapter 6. This metamaterial analogue of EIT has attracted sustained attention for its promise in THz sensing, slow-light devices, and modulators [16–18]. But beneath the clean spectral picture it presents, a set of deeper questions have remained unresolved.

The first concerns what happens when this metamaterial is no longer isolated. The near-field of a metallic THz resonator, particularly within the capacitive gap of a split-ring geometry, confines electromagnetic energy into volumes approaching or below the diffraction limit. The coupling strengths accessible in those volumes can far exceed what free-space propagation allows. When a material carrying a resonance in the same frequency range is brought into contact with the metamaterial, the photonic and material degrees of freedom can hybridize into polaritons whose properties belong to neither partner individually [19–23]. Phonon-polariton coupling has been demonstrated in individual THz resonators coupled to polar crystals and perovskite films [19, 22, 23], but those studies addressed isolated resonators with a single spectral feature. The consequences of introducing such coupling within an EIT configuration, where the transparency window itself arises from bright-dark mode interference, have not been explored. Whether this hybridization can be steered to produce qualitatively new spectral functionality, and whether the result can be switched without modifying the device itself, is the first open question this thesis

takes up directly. The second question concerns the dynamics operating within the bare metamaterial itself. A linear transmittance spectrum is a time-averaged quantity. It reveals where the transparency window sits and how wide it is, but it cannot separately resolve the population relaxation time of the bright mode, the inter-mode coherence lifetime, or the pure dephasing contribution that structural disorder adds to the total linewidth. Each of these timescales has direct consequences for device performance. The achievable group delay, the modulation depth, and the switching speed of any EIT-based device are all bounded by them. For all-metallic metamaterials on insulating substrates such as quartz, optical pump-THz probe (OPTP) spectroscopy cannot address this problem cleanly. In those methods, the optical pump couples primarily to substrate defects or any integrated photoactive layer rather than to the metallic resonators directly, convolving substrate and resonator dynamics in the measured signal [24–27]. The only approach that avoids this complication is to drive the metamaterial with THz fields alone, whose photon energies lie far below the quartz bandgap, and to read out what the nonlinear response reveals about the coherent timescales. This is the second question the thesis addresses.

Both questions point toward the same platform and the same experimental philosophy: a metamaterial whose geometry is fixed, interrogated first through the lens of strong phonon-polariton coupling and then through the lens of nonlinear coherent THz spectroscopy. The choice of the THz frequency range is not incidental. The TO phonon of $MAPbI_3$ perovskite, the material used in this work, lies at 1 THz [19, 22, 23], placing it directly within the accessible spectral window of THz time-domain spectroscopy and within reach of the metamaterial resonances. Equally, in the THz metamaterial system, the relevant coherent timescales, population lifetimes, and inter-mode dephasing occur on the order of one to two picoseconds. These timescales fall naturally within the temporal resolution of phase-locked THz pulse pairs, making two-dimensional (2D) THz spectroscopy an appropriate tool for extracting them.

This thesis addresses both questions through two closely connected experimental studies on the same platform: a micron-scale array of aluminum rod and SRR pairs fabricated on a *z*-cut quartz substrate [15]. The first study integrates this system with a phonon-active $MAPbI_3$ perovskite film and examines the spectral, field-distribution, and dispersion consequences of strong phonon-polariton coupling within the EIT configuration [15]. The second drives the bare metamaterial into the nonlinear regime using phase-locked THz pulse pairs and extracts, from the third-order signals that emerge, the coherent timescales that linear spectroscopy cannot separately resolve [28]. The questions posed above are not left open; they are systematically investigated and answered through the experimental and theoretical work presented in the chapters that follow.

Outline of the Thesis

The thesis is organised into seven chapters. Each addresses a distinct aspect of the problem, building from foundational concepts through experimental and computational methods and into the two original research contributions.

Chapter 2: Scientific Background. This chapter builds the theoretical foundation for the rest of the thesis. It covers light-matter interaction, the distinction between weak and strong coupling, polariton formation, and the threshold condition for coherent hybridization. EIT is developed from its quantum mechanical origin and its classical analogue in coupled resonator systems. The chapter also introduces the density matrix formalism and the Lindblad master equation, and defines the population relaxation time T_1, the coherence lifetime T_2, and the pure dephasing time T_φ, which are the central quantities extracted in Chapter 6.

Chapter 3: Experimental Approaches. This chapter describes all the experimental techniques used in this work. It covers THz pulse generation via photoconductive antennas and optical rectification, detection via electro-optic sampling, and the principles of THz

time-domain spectroscopy. It then develops 2D THz spectroscopy, including the three-measurement subtraction protocol, the two-dimensional Fourier analysis, and the identification of the four third-order nonlinear signals and the timescales they encode.

Chapter 4: Numerical Simulation and Fabrication. This chapter covers the computational and fabrication methods used throughout the thesis. The finite integration technique implemented in CST Microwave Studio is described, including the unit cell setup, material parameters, boundary conditions, and the extraction of transmittance spectra and field distributions. The fabrication of the metamaterial by maskless photolithography and aluminum deposition is then described, followed by the spin-coating procedure for the $MAPbI_3$ perovskite film and the Lorentz oscillator model used to represent its phonon mode in simulation.

Chapter 5: Phonon-Polariton Coupled Dual EIT. This chapter presents the first original research contribution. It examines what happens when the EIT metamaterial is coupled to the TO phonon mode of a $MAPbI_3$ thin film. Strong coupling is confirmed through avoided crossings and Rabi splitting that exceed the dissipative threshold, with an interaction potential of $V = 0.538\,\text{meV}$ against a threshold of $V_{\text{st}} = 0.294\,\text{meV}$. The hybridization transforms the single EIT transparency window into a dual EIT-like response with peaks near 0.9 THz and 1.2 THz, and field distribution analysis confirms that both windows retain genuine EIT character. Group delay measurements show that slow-light behavior is preserved at both transparency windows. The chapter also demonstrates reversible switching between the dual-EIT and conventional Rabi splitting regimes through rotational and translational tuning of the device geometry, without any structural modification.

Chapter 6: Nonlinear EIT Dynamics via 2D-THz Spectroscopy. This chapter presents the second original research contribution. 2D-THz spectroscopy is applied to the bare EIT metamaterial to extract the bright-mode relaxation time $T_1 = 1.96\,\text{ps}$ and the coherence lifetime $T_2 = 1.0\,\text{ps}$ from the pump-probe and photon-echo signals. The

inequality $T_2 < 2T_1$ indicates the presence of pure dephasing with $T_\varphi = 1.34\,\mathrm{ps}$, attributed to structural inhomogeneity arising from lithographic dimensional variations across the array. The multi-peak photon-echo structure directly visualizes the dressed-state doublet underlying the EIT window and enables a quantitative separation of homogeneous and inhomogeneous broadening, identifying structural disorder as the dominant limit on EIT linewidth in this system.

Chapter 7: Conclusion and Outlook. The final chapter brings together the findings of both studies and considers what they reveal collectively about EIT in THz metamaterials. It revisits the questions posed in this introduction and summarises how each one was answered. The chapter closes by identifying the open questions this work raises, including the prospect of applying 2D-THz spectroscopy to the phonon-hybridized system of Chapter 5.

Chapter 2

Scientific Background

2.1 Light-Matter Interaction

The interaction between an electromagnetic field and matter is one of the most fundamental processes in physics. When an oscillating electric field encounters a material, it exerts forces on the charged particles within that material. These forces drive the charges into motion, and the moving charges in turn exchange energy with the field [29, 30]. This exchange underlies every spectroscopic observable we measure, from absorption and emission to scattering and dispersion. Describing this process quantitatively requires a framework that handles both the field and the matter consistently. The full quantum electrodynamical treatment does this, but it is more general than what most spectroscopy experiments require. For the purposes of this thesis, a semi-classical approach is sufficient [29, 30]. In this approach, the matter is treated quantum mechanically while the electromagnetic field is treated as a classical oscillating wave. This simplification captures all the physics relevant to the experiments described in the following chapters.

The simplest quantum mechanical model for a material resonance is the two-level system. It consists of a ground state $|0\rangle$ with energy E_0 and an excited state $|1\rangle$ with energy E_1. The transition frequency between the two states is $\omega_0 = (E_1 - E_0)/\hbar$. When an oscillating electric field $E(t) = E_0 \cos(\omega t)$ is applied, the coupling between the field and the matter is described by the electric dipole Hamiltonian,

$$\hat{H}_{\text{int}} = -\hat{\mu} \cdot \mathbf{E}(t), \tag{2.1}$$

where $\hat{\mu} = e\hat{\mathbf{r}}$ is the electric dipole moment operator. This expression is written within the dipole approximation, which assumes that the wavelength of the field is much larger than the spatial extent of the quantum system. In the THz frequency range, this condition is well satisfied for both atomic systems and metallic resonators whose dimensions are on the order of tens of micrometers. The total Hamiltonian of the driven system is $\hat{H} = \hat{H}_0 + \hat{H}_{\mathrm{int}}$, where $\hat{H}_0$ is the bare Hamiltonian of the unperturbed two-level system.

To find how the system evolves under this Hamiltonian, we write the state as a superposition $\left|\psi(t)\right\rangle = c_0(t)\left|0\right\rangle + c_1(t)\left|1\right\rangle$ and apply the time-dependent Schrödinger equation. After invoking the rotating-wave approximation (RWA) to remove terms oscillating much faster than the resonance frequency, the equations of motion reduce to the optical Bloch equations. These are most naturally written in terms of the density matrix $\hat{\rho}$, whose elements are $\rho_{ij} = c_i c_j^*$. The diagonal elements ρ_{00} and ρ_{11} are the populations of the two states. The off-diagonal elements ρ_{01} and ρ_{10} are the coherences, carrying the phase information about the superposition. In the presence of dissipation, the Bloch equations take the form

$$\frac{d\rho_{11}}{dt} = \frac{i\Omega}{2}\left(\rho_{10} - \rho_{01}\right) - \gamma_1\rho_{11}, \tag{2.2}$$

$$\frac{d\rho_{01}}{dt} = \frac{i\Omega}{2}\left(\rho_{00} - \rho_{11}\right) + i\Delta\,\rho_{01} - \gamma_2\rho_{01}, \tag{2.3}$$

where $\Omega = \mu_{10}E_0/\hbar$ is the Rabi frequency, $\Delta = \omega - \omega_0$ is the detuning of the driving field from the transition, $\gamma_1 = 1/T_1$ is the population relaxation rate, and $\gamma_2 = 1/T_2$ is the coherence decay rate.

The steady-state solution of the Bloch equations yields the complex susceptibility $\chi(\omega)$, which connects the macroscopic polarization of the medium to the applied field through $P = \varepsilon_0\chi E$. The real part of χ describes the dispersive response and controls how the phase velocity of light changes near resonance. The imaginary part describes absorption and determines how much energy the field deposits into the medium. On resonance ($\Delta = 0$),

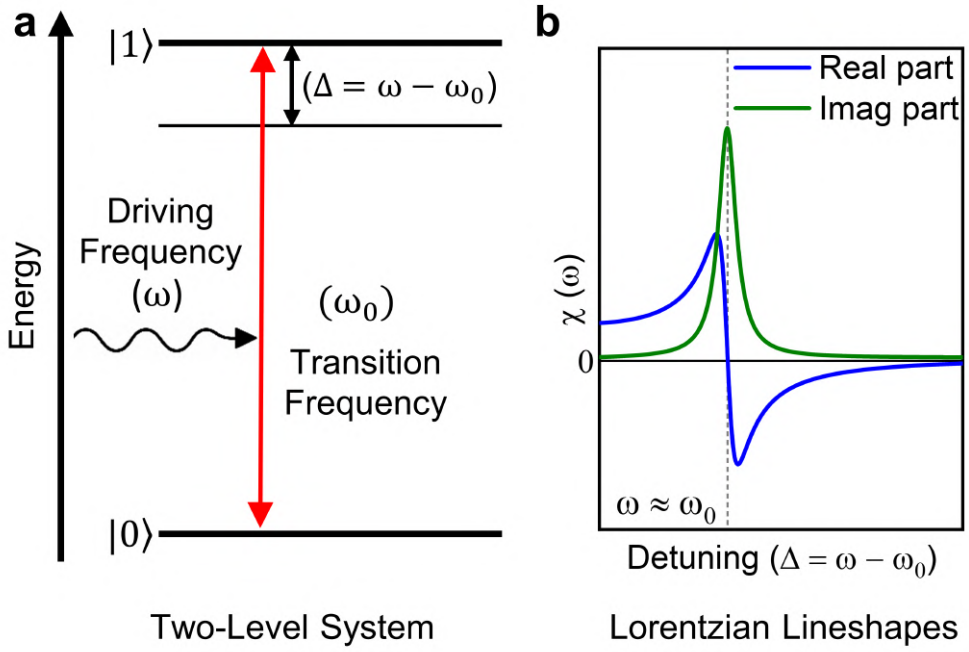

Figure 2.1: Linear response of a two-level system. **(a)** Energy level diagram showing the ground state $|0\rangle$ and excited state $|1\rangle$ separated by the transition frequency ω_0. A driving field at frequency ω interacts with the system with detuning $\Delta = \omega - \omega_0$. **(b)** Corresponding complex susceptibility $\chi(\omega)$ as a function of detuning. The imaginary part (green-curve) follows a Lorentzian lineshape centred at ω_0, representing resonant absorption, while the real part (blue-curve) shows the characteristic dispersive profile associated with anomalous dispersion near resonance.

absorption reaches its maximum and dispersion passes through zero. Both quantities follow a Lorentzian profile away from resonance, as illustrated in Figure 2.1.

In a THz spectroscopy experiment, what is directly measured is the transmitted electric field transient as a function of time. The complex transmittance is obtained from the ratio of the Fourier spectrum of the field through the sample to that through a bare reference substrate. The connection to material properties runs through the complex refractive index $\tilde{n} = n + i\kappa$, where n derives from the real part of χ and κ from the imaginary part. The intensity transmittance follows as $T(\omega) = \exp(-\alpha d)$, where d is the sample thickness and $\alpha = 2\kappa\omega/c$ is the absorption coefficient. This is the Beer-Lambert relation. Because THz-

TDS measures the electric field amplitude directly, the measured field transmittance goes as $\exp(-\alpha d/2)$, and the intensity transmittance is obtained by squaring the spectral amplitude ratio.

The picture described so far assumes a weak driving field, where $\Omega \ll \gamma_1$ and $\Omega \ll \gamma_2$. In this limit, the excited-state population remains small, perturbation theory is valid, and the response is linear. This is the regime in which conventional THz-TDS operates. When the interaction between two distinct physical systems becomes large enough, something qualitatively different can happen: the systems hybridize and form new joint eigenstates. Whether this hybridization occurs or not depends on how the inter-system coupling strength compares to the individual decay rates. The next section develops this point precisely.

2.2 Weak and Strong Coupling

The distinction between weak and strong coupling is one of the central organizing concepts in quantum photonics [2, 4]. It determines the qualitative character of a coupled system and shapes the interpretation of nearly every experiment discussed in this thesis. To understand what the two regimes mean, it helps to start with the simplest possible case: two coupled harmonic oscillators, one representing an electromagnetic mode and the other a material excitation, such as a phonon [19, 21–23], an exciton [31], or a mechanical resonance [2, 4]. Each oscillator has its own resonance frequency and decay rate. The photonic mode has decay rate κ, the material mode has decay rate γ, and when the two interact, energy flows between them at a rate set by the coupling constant g.

If g is small relative to both decay rates, energy transferred from one oscillator to the other is quickly dissipated before it can return. The two subsystems retain their separate identities. The coupling produces only small shifts of the resonance frequencies and slight changes in linewidths. This is the weak coupling regime [32, 33]. Nothing qualitatively

new emerges. In contrast, when g is large enough that coherent energy exchange outpaces the losses, the two modes hybridize completely. Their individual identities are lost and the eigenstates of the coupled system become superpositions of the original modes. The eigenfrequencies split apart, and this splitting is the defining signature of strong coupling. The two new eigenstates are called the upper polariton (UP) and lower polariton (LP), and the energy separation between them at zero detuning is the vacuum Rabi splitting [2–4, 34],

$$\Omega_{\mathrm{R}} = 2g. \tag{2.4}$$

This splitting appears as a pair of resolved peaks in the transmittance or reflection spectrum. The standard spectroscopic criterion for strong coupling is [4, 35]

$$\Omega_{\mathrm{R}} > \frac{\kappa + \gamma}{2}, \tag{2.5}$$

meaning the Rabi splitting must exceed the average linewidth of the two modes for the peaks to be individually resolved. When this condition is met, the two resonances no longer merge into a single feature, and the avoided crossing of the polariton branches as a function of detuning becomes the clearest experimental proof of strong coupling, as shown in Figure 2.2.

The Hamiltonian of the coupled system makes this picture precise. The photonic mode has energy $\hbar\omega_{\mathrm{c}}$ and the material mode has energy $\hbar\omega_{\mathrm{m}}$. The total Hamiltonian in the RWA is [2, 36]

$$\hat{H} = \hbar\omega_{\mathrm{c}}\hat{a}^{\dagger}\hat{a} + \hbar\omega_{\mathrm{m}}\hat{b}^{\dagger}\hat{b} + \hbar g\left(\hat{a}^{\dagger}\hat{b} + \hat{a}\hat{b}^{\dagger}\right), \tag{2.6}$$

where $\hat{a}^{\dagger}$, $\hat{a}$ and $\hat{b}^{\dagger}$, $\hat{b}$ are the creation and annihilation operators for the photonic and material modes respectively. Diagonalizing at zero detuning ($\omega_{\mathrm{c}} = \omega_{\mathrm{m}} = \omega_0$) gives two eigenstates with energies $\hbar(\omega_0 \pm g)$:

$$|\mathrm{UP}\rangle = \frac{1}{\sqrt{2}}\big(|\mathrm{photon}\rangle + |\mathrm{matter}\rangle\big), \tag{2.7}$$

$$|\mathrm{LP}\rangle = \frac{1}{\sqrt{2}}\big(|\mathrm{photon}\rangle - |\mathrm{matter}\rangle\big). \tag{2.8}$$

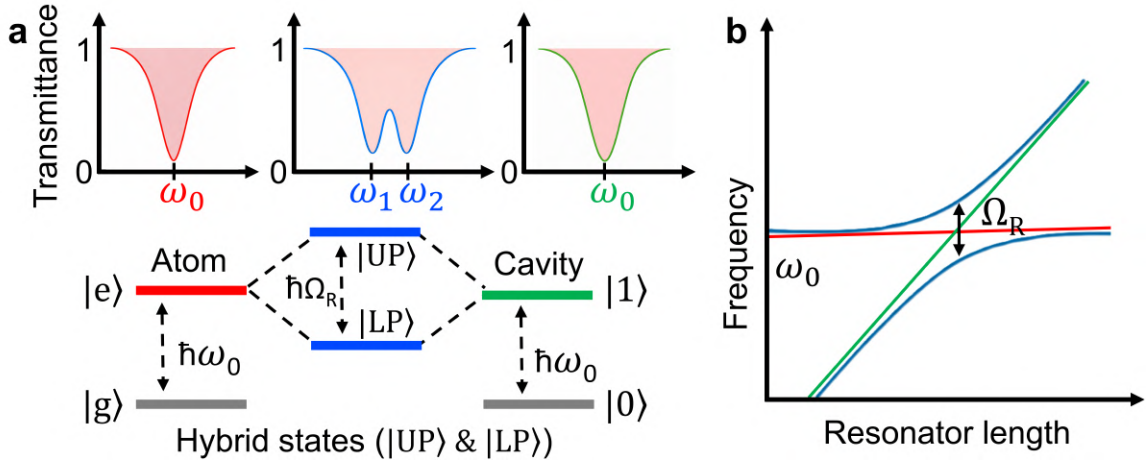

Figure 2.2: Strong coupling between a two-level atom and an optical cavity. **(a)** When the atom and cavity are brought into resonance, their interaction leads to two new hybrid states split by the Rabi frequency $\hbar\Omega_{\mathrm{R}}$. These two new hybrid states are upper polariton (UP) and lower polariton (LP), respectively. The transmission spectrum evolves from a single absorption dip to a double-dip profile, a direct signature of strong coupling. **(b)** Avoided crossing in the eigenfrequency dispersion as a function of resonator length. The two branches repel each other rather than cross, with the minimum separation equal to Ω_{R}.

At non-zero detuning $\Delta = \omega_{\mathrm{c}} - \omega_{\mathrm{m}}$, the photonic and material fractions of each polariton branch are no longer equal but are described by Hopfield coefficients [37–39], which evolve continuously as the detuning is swept. Tracking this evolution produces the avoided crossing diagram discussed further in Chapter 5.

The coupling constant g depends on both the geometry of the system and the properties of the material excitation [2, 4]. In cavity quantum electrodynamics (cQED), g is proportional to the vacuum electric field amplitude E_{vac} at the location of the emitter [40],

$$E_{\mathrm{vac}} = \sqrt{\frac{\hbar\omega}{2\varepsilon_0 V_{\mathrm{eff}}}}, \tag{2.9}$$

where V_{eff} is the effective mode volume. A smaller mode volume produces a larger vacuum field and therefore a stronger coupling. This is why metallic THz resonators are well suited to strong coupling experiments: their sub-wavelength geometry, and especially the capacitive gap of the SRR, confines the electromagnetic field into volumes approaching or

below the diffraction limit, producing vacuum fields large enough to drive coupling rates that exceed the decay rates of both modes at room temperature.

In the experiments described in Chapter 5, the material excitation is the TO phonon of a $MAPbI_3$ perovskite film. In a polar crystal, certain phonon modes involve the relative displacement of oppositely charged sublattices, creating an oscillating electric dipole moment that allows the phonon to interact with the electromagnetic near-field of the metallic resonators. The TO phonon of $MAPbI_3$ lies at 0.97 THz, placing it within reach of the metamaterial resonances. Whether the coupling satisfies the strong coupling criterion of Eq.(2.5) is verified in Chapter 5 using an interaction potential formalism, where $V > V_{\mathrm{st}}$ plays the role of the condition $\Omega_{\mathrm{R}} > (\kappa + \gamma)/2$. The connection between the two criteria is discussed there in detail.

Both strong coupling and EIT, the topic of Sections 2.6 and 2.7, involve a competition between coherent coupling and dissipation. Both produce spectral features that are direct signatures of that competition. Understanding strong coupling first therefore provides the conceptual and mathematical foundation needed to approach EIT in what follows.

2.3 Density Matrix Formalism and Lindblad Master Equation

The optical Bloch equations of Section 2.1 describe a single two-level system driven by a coherent field. For the more general problem of a multi-level system coupled to both a driving field and a dissipative environment, a more complete framework is needed. The density matrix formalism provides this. It handles pure states and statistical mixtures on equal footing and extends naturally to systems with any number of levels and multiple relaxation channels.

The density matrix $\hat{\rho}$ is a Hermitian operator whose diagonal elements ρ_{ii} give the population of state $|i\rangle$ and whose off-diagonal elements ρ_{ij} $(i \neq j)$ describe the coherence between

states $|i\rangle$ and $|j\rangle$. The populations satisfy $\sum_i \rho_{ii} = 1$, reflecting probability conservation. The coherences carry phase information about the superposition of different states and decay as the system loses its phase relationship with the driving field.

In the absence of dissipation, the time evolution of $\hat{\rho}$ is governed by the Liouville-von Neumann equation [41],

$$\frac{d\hat{\rho}}{dt} = -\frac{i}{\hbar}\left[\hat{H}(t),\, \hat{\rho}\right]. \tag{2.10}$$

This equation is exact for a closed system but does not account for the inevitable coupling of any real system to its environment. The standard way to include environmental dissipation while preserving the positivity and trace of $\hat{\rho}$ is to add a Lindblad superoperator $\mathcal{L}(\hat{\rho})$ to the right-hand side of Eq.(2.10). The resulting Lindblad master equation [42–44] is

$$\frac{d\hat{\rho}}{dt} = -\frac{i}{\hbar}\left[\hat{H}(t),\, \hat{\rho}\right] + \mathcal{L}(\hat{\rho}), \tag{2.11}$$

where the Lindblad superoperator sums over all dissipation channels,

$$\mathcal{L}(\hat{\rho}) = \sum_k \gamma_k \left(\hat{L}_k \hat{\rho} \hat{L}_k^\dagger - \tfrac{1}{2}\hat{L}_k^\dagger \hat{L}_k \hat{\rho} - \tfrac{1}{2}\hat{\rho}\hat{L}_k^\dagger \hat{L}_k\right) = \sum_k \gamma_k \left(\hat{L}_k \hat{\rho} \hat{L}_k^\dagger - \tfrac{1}{2}\left\{\hat{L}_k^\dagger \hat{L}_k,\, \hat{\rho}\right\}\right). \tag{2.12}$$

The two forms on the right are equivalent; the anticommutator notation $\{A, B\} = AB + BA$ is used in Chapter 6 for compactness. Each $\hat{L}_k$ is a Lindblad operator describing a specific dissipation process and γ_k is the corresponding rate.

Two classes of dissipation are particularly important here. The first is population relaxation. When a system in state $|i\rangle$ decays to state $|j\rangle$, the Lindblad operator is $\hat{L} = |j\rangle\langle i|$, which reduces the population of $|i\rangle$ at rate γ_1 and damps coherences involving $|i\rangle$ at rate $\gamma_1/2$. The second is pure dephasing, described by a diagonal operator $\hat{L} = |i\rangle\langle i|$ at rate γ_φ. Pure dephasing randomizes the phase of the quantum state without transferring any population between levels, attenuating only the off-diagonal elements of $\hat{\rho}$.

For the three-level Λ system [45] used to model the EIT metamaterial in Chapter 6, the Lindblad master equation provides the complete theoretical description of the nonlinear

dynamics. The total Hamiltonian is $\hat{H}(t) = \hat{H}_0 + \hat{H}_c + \hat{H}_{int}(t)$ [46], where $\hat{H}_0$ is the bare system Hamiltonian, $\hat{H}_c$ is the structural coupling between the bright and dark resonator modes, and $\hat{H}_{int}(t)$ is the interaction with the driving THz field. Numerical integration using a fourth-order Runge-Kutta algorithm yields the time evolution of all density matrix elements. The macroscopic current response of the metamaterial is then computed as

$$j(t) = \frac{iN}{\hbar} \sum_{k,l} \rho_{kl}(t) \left(E_k - E_l\right) d_{kl}, \tag{2.13}$$

where d_{kl} are the dipole matrix elements and N is the number density of resonators. The factor of i arises from the time derivative of the macroscopic polarization $P = N \sum_{kl} \rho_{kl} d_{kl}$ under the Liouville equation, so that $j = \dot{P}$ acquires this factor. This current connects the density matrix directly to the measurable THz electric field.

2.4 Population Relaxation, Coherence Lifetime, and Pure Dephasing

The Lindblad master equation introduces three distinct timescales that characterize how a system loses its excited-state energy and phase coherence. These timescales are the central quantities extracted from the 2D-THz experiment in Chapter 6, so it is important to define them carefully here.

The first is the population relaxation time T_1. It measures how long the excited-state population persists before decaying to the ground state. For a general two-level system, T_1 is determined by all energy loss channels, including radiative emission and non-radiative dissipation. The population relaxation rate is $\gamma_1 = 1/T_1$.

The second is the coherence lifetime T_2. It measures how long an off-diagonal density matrix element ρ_{ij} remains non-zero. The coherence decays whenever either the population relaxes or the phase of the oscillation is randomized by any process. The coherence decay rate is $\gamma_2 = 1/T_2$. In the specific context of the EIT metamaterial studied in Chapter 5

and 6, the T_1 and T_2 measures the lifetime of the bright-mode relaxation and the coherent superposition between the bright and dark resonator modes that sustains the transparency window, respectively.

The third is the pure dephasing time T_φ. It captures all phase-randomizing processes that do not involve population transfer. Examples include collisions in atomic systems, charge noise in solid-state qubits, and frequency disorder across an ensemble of oscillators. In any fabricated structure measured as an ensemble, the spread of resonance frequencies across individual units is a natural source of pure dephasing: contributions from different members accumulate different phases over time, degrading the ensemble coherence without dissipating any individual unit's energy. The pure dephasing rate is $\gamma_\varphi = 1/T_\varphi$.

The three timescales are connected by the relation [47]

$$\frac{1}{T_2} = \frac{1}{2T_1} + \frac{1}{T_\varphi}. \tag{2.14}$$

Coherence is destroyed either by population relaxation, contributing at half the rate γ_1, or by pure dephasing acting directly on the phase. The total coherence decay rate is the sum of both contributions.

2.5 Metamaterials

The preceding sections developed the theoretical language of light-matter interaction, coupling, and decoherence. What those sections left open is a practical question: where does one find a room-temperature platform that can sustain strong coupling and EIT-like responses at THz frequencies? The answer lies in a class of engineered structures called metamaterials.

Metamaterials are artificially constructed materials whose electromagnetic properties are not determined by their chemical composition but by the geometry of their structural units. These units, called meta-atoms, are kept well below the wavelength of the radiation

they interact with [48–51]. Because the wavelength is much larger than each meta-atom, the radiation responds to the average electromagnetic properties of the composite [52–54]. This average response is described by two effective medium parameters: the electric permittivity $\varepsilon(\omega)$ and the magnetic permeability $\mu(\omega)$. By designing the meta-atom geometry, both can be engineered independently and pushed into ranges that no naturally occurring material occupies [55, 56].

To appreciate what this means, consider the four quadrants of the ε–μ parameter space as shown in Figure 2.3. Conventional dielectrics have $\varepsilon > 0$ and $\mu > 0$; waves propagate forward and the medium is right-handed. Metals below the plasma frequency have $\varepsilon < 0$ and $\mu > 0$; waves decay evanescently. Ferrites occupy $\varepsilon > 0$, $\mu < 0$ and are similarly evanescent. The fourth quadrant, $\varepsilon < 0$ and $\mu < 0$ simultaneously, does not occur in nature [56,57]. A medium there supports propagation but with the phase velocity and energy flow antiparallel, reversing Snell's law and producing a negative refractive index. Only artificial construction can access this quadrant.

The optical response of any medium is governed by Maxwell's equations. For a linear, isotropic medium, these can be written in differential form as

$$\nabla \cdot \mathbf{E} = \rho/\varepsilon, \tag{2.15}$$

$$\nabla \cdot \mathbf{B} = 0, \tag{2.16}$$

$$\nabla \times \mathbf{E} = -\frac{\partial \mathbf{B}}{\partial t}, \tag{2.17}$$

$$\nabla \times \mathbf{B} = \mu\mathbf{J} + \varepsilon\mu\frac{\partial \mathbf{E}}{\partial t}, \tag{2.18}$$

where $\mathbf{E}$ and $\mathbf{B}$ are the electric field and magnetic flux density, and ρ and $\mathbf{J}$ are the free charge and current densities. The parameters ε and μ correspond to the permittivity and permeability of the medium. In metamaterials, these electromagnetic parameters are not solely determined by the intrinsic properties of the constituent materials, but arise from

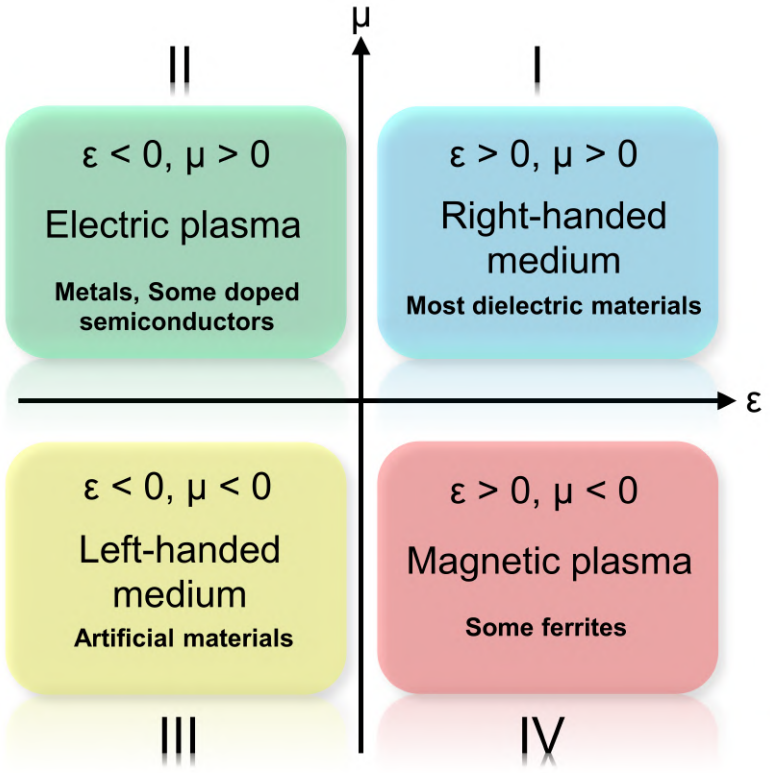

Figure 2.3: Classification of electromagnetic materials in the ε–μ parameter space.

the subwavelength structural design of the system. As a result, the effective permittivity $\varepsilon(\omega)$ and permeability $\mu(\omega)$ become strongly frequency-dependent and can be engineered to achieve tailored electromagnetic responses. These equations are solved numerically in Chapter 4 using the finite integration technique (FIT) in CST Microwave Studio.

The history of metamaterials traces back further than the modern terminology suggests. In 1898, J. C. Bose demonstrated the rotation of microwave polarization using twisted jute structures [58, 59], now recognized as artificial chiral media. In 1968, V. G. Veselago theoretically predicted the behavior of a hypothetical medium with simultaneously negative ε and μ [57]. The experimental realization came decades later, when J. B. Pendry showed that thin metallic wire arrays produce a negative effective permittivity [60, 61], and D. R. Smith demonstrated negative refractive index in a composite of split-ring resonators and

thin wires [62, 63]. These demonstrations confirmed what Veselago had predicted, and the field grew rapidly from that point.

One of the most important building blocks in this field is the SRR [48,62,63]. It consists of a metallic ring with a small gap. The ring provides inductance through its circular current path, and the gap provides capacitance through charge accumulation at its edges. Together they form an LC resonant circuit with resonance frequency [64]

$$\omega_{\mathrm{R}} = \frac{1}{\sqrt{LC}}, \tag{2.19}$$

where the effective inductance is $L = \mu_0 l^2/t$ and the effective capacitance is $C = \varepsilon_0 wt/d$. Here l is the side length, t is the metal thickness, w is the linewidth, and d is the gap size. Substituting gives

$$\omega_{\mathrm{R}} = \frac{c}{l}\sqrt{\frac{d}{w}}, \tag{2.20}$$

which shows that the resonance frequency scales inversely with the side length l and increases with the gap-to-linewidth ratio d/w. Reducing the physical dimensions of the SRR to the micron range shifts its resonance into the THz window, and the same scaling principle applies to other resonator geometries including cut wires, circular rings, and asymmetric SRRs. This scalability makes metallic resonators extremely versatile building blocks for THz devices.

When multiple resonators with different radiative properties are combined in a single unit cell, they can interact through their overlapping near-fields [65–67], enabling the engineering of interference effects in metamaterials. In particular, this near-field coupling is the mechanism through which EIT-*like* responses are realized [68–70]. The following section introduces EIT from its quantum mechanical origin before returning to the metamaterial implementation.

2.6 Electromagnetically Induced Transparency

Electromagnetically induced transparency was first observed in a laser-driven atomic vapor by Boller, Imamoğlu, and Harris in 1991 [71]. A strong control field was applied to one transition of a three-level system while a weak probe field scanned across another. In the absence of the control field, the probe was strongly absorbed at the atomic resonance. With the control field present, a narrow transparency window appeared within the absorption band. The transparency did not result from any shift of the energy levels. It arose from the quantum mechanical interference between two distinct excitation amplitudes for reaching the excited state from the ground state.

To understand this interference, consider the three-level Λ system shown in Figure 2.4. The ground state is $|1\rangle$, the excited state is $|3\rangle$, and $|2\rangle$ is a metastable state. The transition $|1\rangle \leftrightarrow |3\rangle$ is dipole-allowed and couples to the probe field. The transition $|1\rangle \leftrightarrow |2\rangle$ is dipole-forbidden. The control field drives the $|3\rangle \leftrightarrow |2\rangle$ transition, creating a dressed state that mixes $|2\rangle$ and $|3\rangle$. There are now two quantum mechanical amplitudes by which the probe photon can excite the system to state $|3\rangle$: one through the bare transition $|1\rangle \rightarrow |3\rangle$, and one through the control-field-dressed pathway involving $|2\rangle$. When both fields are on resonance, these two amplitudes are equal in magnitude and opposite in phase. They cancel, and the total transition probability to the excited state drops to zero [5, 72, 73]. The medium becomes transparent.

The transparency window is accompanied by a dramatic change in dispersion. Within the window, the real part of the susceptibility varies steeply with frequency. This steep variation produces a large group index n_g and reduces the group velocity to values far below the speed of light,

$$v_g = \frac{c}{n_g} = \frac{c}{n + \omega \frac{dn}{d\omega}}, \tag{2.21}$$

where the large derivative $dn/d\omega$ within the EIT window reduces v_g dramatically. This

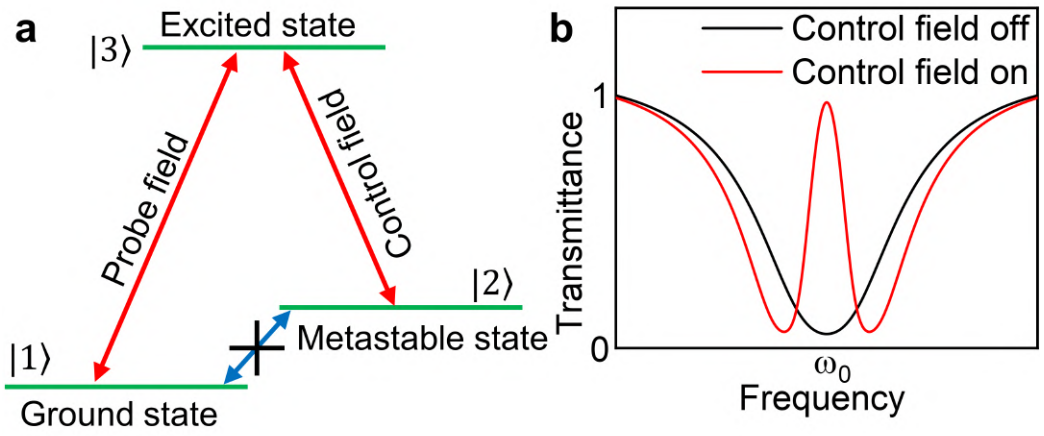

Figure 2.4: Electromagnetically induced transparency in a three-level Λ-system. **(a)** Energy level diagram showing ground state $|1\rangle$, metastable state $|2\rangle$, and excited state $|3\rangle$. The probe field couples $|1\rangle \rightarrow |3\rangle$, the control field drives $|2\rangle \rightarrow |3\rangle$, and the direct transition $|1\rangle \leftrightarrow |2\rangle$ is forbidden. **(b)** Transmission spectra with the control field off (black-curve) and on (red-curve), showing the emergence of a narrow transparency window within the broad absorption profile.

slow-light effect [7, 8] is what first attracted attention to EIT for applications in optical delay lines and quantum memory, where controllable pulse delay and coherent storage are required.

The width and depth of the transparency window are governed by the balance between coherent coupling and decoherence. The control field Rabi frequency Ω_c sets the width: a stronger control field opens a wider window [74, 75]. The coherence decay rate γ_{32} between states $|3\rangle$ and $|2\rangle$ governs how completely the absorption is suppressed. In cold atomic systems, γ_{32} can be made extremely small, producing a very narrow and deep window. At room temperature, collisions and dephasing processes increase γ_{32}, degrading both the depth and width. This sensitivity to decoherence is what makes atomic EIT challenging to translate into practical devices.

2.7 EIT in Metamaterials

The conditions required for atomic EIT are demanding: cold atoms, narrow-linewidth lasers, and cryogenic isolation. A natural question is therefore whether the interference mechanism responsible for EIT can be reproduced in a simpler, room-temperature platform. The answer is yes, provided the platform supports two resonances with different radiative damping rates and a controllable near-field coupling between them. Metamaterials satisfy both conditions without any specialized optical source [16–18].

In a metamaterial EIT system, the roles of the atomic levels are taken by electromagnetic resonances of the metallic structure. One resonator couples strongly to the incident field and radiates efficiently. This is the bright mode, with a broad linewidth due to large radiation losses. The other resonator couples weakly or not at all under the given polarization condition. This is the dark mode, with a narrow linewidth because its radiative losses are suppressed [76–79]. In close proximity, the near fields of the two resonators overlap, establishing a coupling between them. The bright mode is excited directly by the incident THz pulse and transfers energy to the dark mode. The back-action of the dark mode on the bright mode creates a second excitation amplitude that interferes destructively with the directly excited amplitude in the radiative channel, suppressing far-field emission from the bright mode at a specific frequency. This suppression appears in the transmittance spectrum as a narrow transparency window [68–70].

The analogy with the Λ system of Section 2.6 is direct. The unexcited metamaterial maps onto the ground state $|1\rangle$. The dipole resonance of the bright resonator maps onto the excited state $|3\rangle$. The sub-radiant resonance of the dark resonator maps onto the metastable state $|2\rangle$. The near-field coupling between the resonators plays the role of the control field, but with one important difference: it is built into the geometry of the unit cell and requires no external field. Note that the state labels used here ($|1\rangle$, $|2\rangle$, $|3\rangle$) follow the convention of

atomic EIT; in Chapter 6, where the density matrix model is developed for the metamaterial, the labels are shifted to $|0\rangle$, $|1\rangle$, $|2\rangle$ following the convention standard in the quantum optics literature for a three-level Λ system with a ground state.

The most commonly used configuration, and the one on which this thesis is based, consists of a metallic rod resonator positioned symmetrically between a pair of SRRs on a dielectric substrate. Under THz illumination with the electric field polarized along the rod, the rod supports a dipole resonance and acts as the bright mode. The structural symmetry prevents the SRR pair from being driven directly by this polarization, but the x-component of the near-field produced by the excited rod drives the LC resonance of the SRR pair. This is the dark mode. When the two resonances are close in frequency, near-field coupling opens the EIT transparency window [15, 80].

The transmittance of this system is described analytically by the coupled oscillator model. The equations of motion for the bright mode amplitude x_b and dark mode amplitude x_d are [16, 70]

$$\ddot{x}_\mathrm{b} + \gamma_\mathrm{b}\dot{x}_\mathrm{b} + \omega_\mathrm{b}^2 x_\mathrm{b} + \kappa^2 x_\mathrm{d} = g_\mathrm{dr}\, E(t), \tag{2.22}$$

$$\ddot{x}_\mathrm{d} + \gamma_\mathrm{d}\dot{x}_\mathrm{d} + \omega_\mathrm{d}^2 x_\mathrm{d} + \kappa^2 x_\mathrm{b} = 0, \tag{2.23}$$

where ω_b and ω_d are the resonance frequencies, γ_b and γ_d are the linewidths (FWHM), κ is the near-field coupling coefficient, and g_dr is the driving efficiency of the bright mode. The quantity g_dr is not the same as the coupling constant g of Section 2.2: g describes coherent energy exchange between two modes in a quantum Hamiltonian, while g_dr is a classical driving amplitude measuring how efficiently the incident field excites the bright resonator. The near-field coupling κ is the classical analogue of g, quantifying the rate of coherent energy exchange between the two resonators. In the density matrix description of Chapter 6, κ maps onto the structural coupling parameter g_s in the three-level Hamiltonian, with both governing the hybridized mode splitting that produces the EIT window.

The dark mode has no direct driving term because it cannot be excited by the incident field under the given polarization. The steady-state solution of Eqs. 2.22 and 2.23 gives the transmittance [81]

$$T = 1 - \left| \frac{g_{\mathrm{dr}}(\omega - \omega_d + i\gamma_d)}{(\omega - \omega_b + i\gamma_b)(\omega - \omega_d + i\gamma_d) + \kappa^2} \right|^2 , \tag{2.24}$$

where γ_b and γ_d are the half-width at half-maximum linewidths of the bright and dark modes, κ is the near-field coupling coefficient, and g_{dr} is the radiative coupling amplitude. When $\kappa = 0$, this reduces to a single Lorentzian dip at ω_{b}, the bare absorption of the bright mode. When $\kappa \neq 0$ and the two resonances are close in frequency, the coupling redistributes spectral weight and opens the EIT transparency window. The width of this window narrows as γ_{d} decreases, mirroring the role of the coherence decay rate in the atomic system.

The coupling coefficient κ is set entirely by the unit cell geometry: the gap between the rod and the SRR pair, the lateral offset of the SRRs, and the orientation relative to the incident polarization. This tunability allows the transparency window to be repositioned and reshaped through lithographic design alone, without any active element.

Tunability can also be achieved dynamically after fabrication by integrating a photoactive or phase-change material into the unit cell to modify either the coupling or the resonance frequencies [24, 82–85]. Active EIT metamaterials of this kind have been realized using graphene [83, 86], vanadium dioxide [84], and superconducting films [85]. A single bright mode coupled to a single dark mode produces one transparency window, but adding a second dark mode at a different frequency introduces a second coupling pathway and opens a second window within the same absorption band [24, 87]. This dual-band EIT response is the starting point for the more complex phonon-hybridized system studied in Chapter 5.

In all of these configurations, the key mechanism is the same: destructive interference between a direct and a dark-mode-mediated excitation amplitude suppresses radiation from the bright resonator at a specific frequency, opening a transparency window whose prop-

erties mirror those of atomic EIT almost exactly. This correspondence is not coincidental. Both systems are governed by the same three-level interference physics, expressed in classical language for the metamaterial and in quantum mechanical language for the atom. The density matrix and Bloch equation framework introduced in the preceding sections therefore applies directly to the metamaterial system, with the bright and dark resonator modes taking the place of the atomic states. This equivalence is the foundation on which the theoretical models of Chapters 5 and 6 are built.

The two experimental studies in this thesis approach the EIT metamaterial from complementary directions. Chapter 5 adds a new degree of coupling by hybridizing the resonators with a phonon mode, asking what strong light-matter interaction produces when the EIT interference is already in place. Chapter 6 removes any external perturbation and probes the bare system with phase-locked THz pulse pairs, asking what the nonlinear response reveals about the timescales that linear spectroscopy cannot separate. Together they map both the spectral and dynamical properties of THz EIT metamaterials within a single unified framework.

2.8 Connection to Broader Strong Coupling Platforms

The strong coupling physics demonstrated in this thesis is not unique to THz metamaterials. The same mathematical framework, in which two coupled oscillators hybridise into upper and lower polariton branches separated by a vacuum Rabi splitting, applies across a wide range of energy scales and material platforms. Placing the present work within this broader context clarifies both what is shared and what is distinctive about the metamaterial approach.

The idea of using planar metallic metamaterials to reproduce quantum optical phenomena classically has a substantial history. One of the earliest experimental demonstrations showed that coupled THz metamaterial resonators can reproduce the spectral characteristics

of electromagnetically induced transparency observed in atomic systems through classical near-field interference [79]. The EIT metamaterial used throughout this thesis is a direct descendant of that concept: the rod serves as the bright mode and the SRR pair as the dark mode. Meanwhile, the transparency window arises from the same bright-dark interference mechanism. What this thesis adds to that foundation is the integration of a phonon active material to achieve genuine strong-coupling (Chapter 5) and the application of 2D-THz spectroscopy to extract the coherent timescales that govern the EIT dynamics (Chapter 6).

In cavity quantum electrodynamics (cQED), strong-coupling was first achieved between single atoms and optical cavity modes [88, 89]. The coupling strength g in those systems is proportional to the vacuum electric field amplitude within the cavity, which scales inversely with the square root of the mode volume (Eq. 2.9). The same threshold condition $\Omega_R > (\kappa + \gamma)/2$ that governs polariton formation in this thesis (Eq. 2.5) appears throughout cQED, from single atom cavities to semiconductor quantum dot microcavities [90] and superconducting circuits [91]. In circuit QED, superconducting qubits play the role of artificial atoms coupled to microwave resonators, and the decoherence is characterised by precisely the same T_1, T_2, and T_φ timescales extracted in Chapter 6 of this thesis. The pure dephasing rate γ_φ in those systems, typically caused by charge noise or flux noise, is the circuit analogue of the structural inhomogeneity identified in Chapter 6 as the dominant source of dephasing in the metamaterial.

In cavity phononics, strong-coupling between lattice vibrations and confined photonic modes has recently become accessible. Recent studies have demonstrated the evolution from weak to ultrastrong phonon photon coupling in phonon polaritonic microcavities, highlighting the universal nature of hybrid light matter interaction across different material platforms [92]. Strong phonon polariton coupling has also been observed in topological insulator thin films integrated with THz metamaterials, further establishing metamaterial based platforms as versatile systems for investigating coherent light matter interaction in the ter-

ahertz regime [93]. The phonon polariton coupling presented in Chapter 5 of this thesis belongs to this same family, with the distinctive feature that the phonon mode hybridises with a metamaterial that already supports an EIT interference pathway, giving rise to dual transparency windows rather than a simple avoided crossing.

What distinguishes the THz metamaterial approach from these other platforms is the combination of room temperature operation, lithographic tunability, and sub-wavelength mode confinement provided by the metallic resonator geometry. The capacitive gap of the SRR confines the electromagnetic field into volumes far below the diffraction limit, producing vacuum field amplitudes large enough to achieve strong coupling at room temperature without cryogenic infrastructure.

The 2D-THz spectroscopic approach used in Chapter 6 connects to a broader family of multidimensional coherent spectroscopies. The $T_1/T_2/T_\varphi$ framework used here to characterise the metamaterial decoherence is directly borrowed from the decoherence analysis of superconducting qubits and from older spectroscopic traditions in NMR and 2D infrared spectroscopy [94]. Two-dimensional THz spectroscopy has emerged as a powerful technique for investigating coherent dynamics in quantum materials by providing direct access to population relaxation, coherence decay, and many-body interactions [95]. Recent perspectives have further highlighted the importance of multidimensional THz spectroscopy for probing ultrafast coherent phenomena and nonequilibrium dynamics in complex quantum materials [96].

Chapter 3

Experimental Approaches

3.1 THz Time-Domain Spectroscopy

THz time-domain spectroscopy (THz-TDS) has established itself as one of the most powerful and versatile tools for characterizing the electromagnetic response of materials in the frequency range from roughly 0.1 to 10 THz [97]. This spectral window, illustrated in Figure 3.1, sits between the microwave and infrared regimes and provides unique access to low-energy excitations including lattice phonons [98,99], collective charge dynamics [100,101], and polaritons [19,22] that are directly relevant to the metamaterial systems studied in this thesis. Unlike intensity-based spectroscopic methods, THz-TDS measures the electric field of the transmitted pulse directly as a function of time. The Fourier transform of this time-domain waveform yields the complex transmission function of the sample at once, giving access to both the real and imaginary parts of the dielectric response without requiring Kramers-Kronig analysis, provided the measurement is performed in transmission geometry with a well-characterized reference.

The phase-sensitive nature of THz-TDS is its defining advantage for metamaterial characterization. Whereas a power detector would return only $|T(\omega)|^2$, the field measurement gives the complex transmittance

$$\tilde{T}(\omega) = \frac{\tilde{E}_{\mathrm{sample}}(\omega)}{\tilde{E}_{\mathrm{ref}}(\omega)}, \tag{3.1}$$

where $\tilde{E}_{\mathrm{sample}}(\omega)$ and $\tilde{E}_{\mathrm{ref}}(\omega)$ are the Fourier spectra of the field transmitted through the sample and through a bare reference substrate, respectively. From $\tilde{T}(\omega)$, the amplitude and

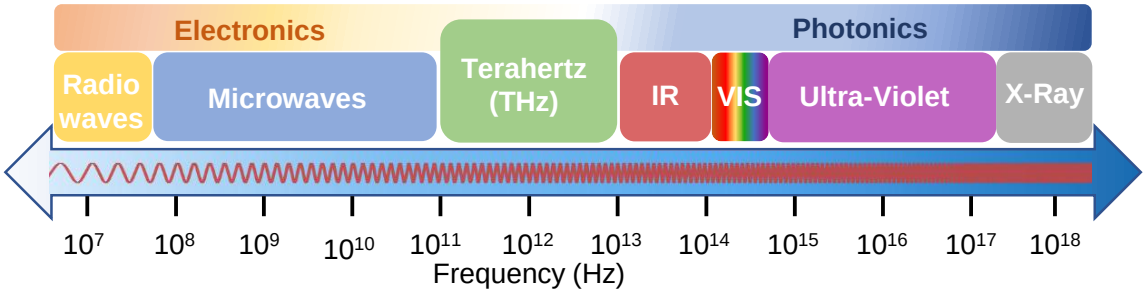

Figure 3.1: The electromagnetic spectrum spanning radio waves to X-rays, illustrating the position of the THz gap (0.1-10 THz) at the boundary between conventional electronics and photonics.

phase of the transmittance are extracted simultaneously, enabling direct determination of the complex refractive index, absorption coefficient, and conductivity. For the EIT metamaterial samples studied here, this phase-sensitive measurement is essential: both the position and the shape of the transparency window, and the group delay associated with it, are encoded in the complex transmittance rather than in the amplitude alone.

3.1.1 Experimental Setup

The THz-TDS setup, as shown in Figure 3.2, used for this thesis is based on a Ti:Sapphire laser system operating at a wavelength of 800 nm, with a pulse duration of 10 fs, repetition rate of 80 MHz, and pulse energy of 3.75 nJ/pulse. This system is distinct from the regeneratively amplified Ti:Sapphire laser used in the 2D-THz experiment described in Section 3.2. In this THz-TDS setup, approximately 90% of the fundamental beam is used for generating THz radiation via an LT-GaAs based photoconductive antenna. The remaining 10% serves as the sampling beam for free-space electro-optic sampling to measure the THz electric field. A pair of parabolic mirrors collimates and focuses the generated THz pulses onto the sample. A second pair of parabolic mirrors focuses the transmitted THz pulses onto a 2 mm thick (110)-cut ZnTe crystal. The sampling beam and the THz beam are aligned collinearly on the detection crystal. The THz-induced birefringence in the crystal rotates the polariza-

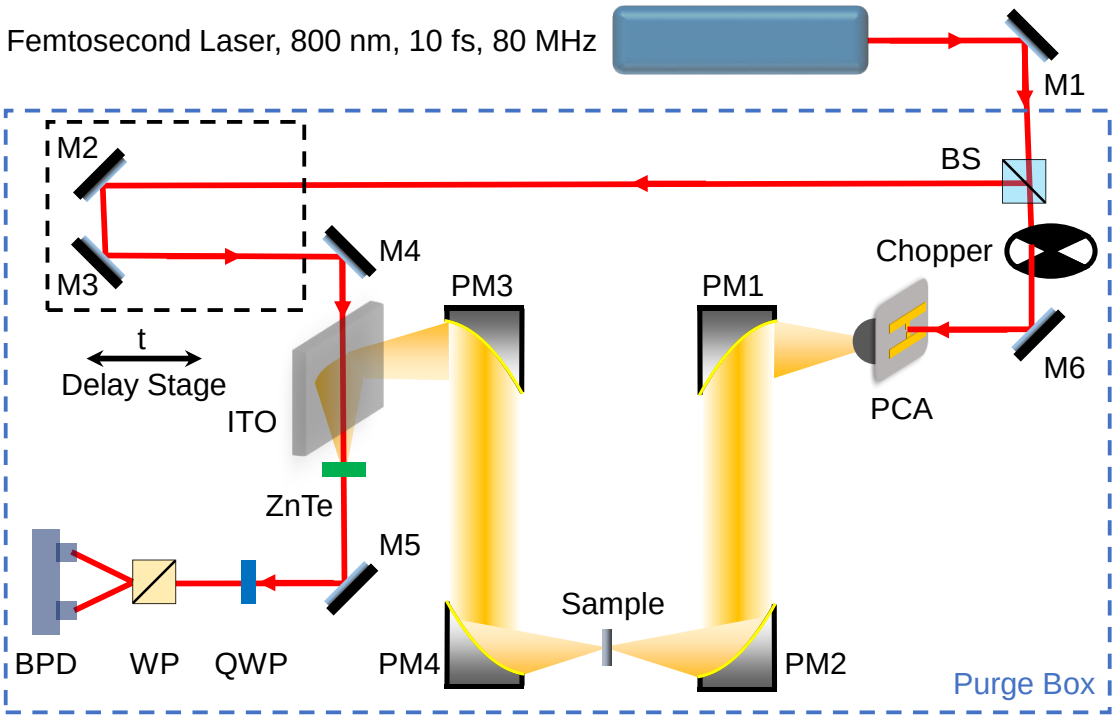

Figure 3.2: Schematic of the THz time-domain spectroscopy setup: M1-6 (mirrors); BS (beamsplitters); PCA (photoconductive antenna); PM1-4 (parabolic mirrors); ITO (indium tin oxide); $\lambda/4$ (quarter-wave plate); WP (Wollaston prism); BPD (balanced photodiode); ZnTe (Zinc Telluride detection crystals); t (real time); Blue-dashed line (Purge box).

tion of the sampling beam. This change in polarization is measured using a quarter-wave plate, a Wollaston prism, and a balanced photodiode via the electro-optic sampling method. From the ellipticity of the sampling beam, the amplitude and phase of the THz pulse are extracted. All measurements are performed in a nitrogen-purged enclosure to suppress water vapor absorption lines across the THz band and, for the phonon-hybridization measurements in Chapter 5, to protect the moisture-sensitive $MAPbI_3$ perovskite film.

3.1.2 THz Generation via Photoconductive Antenna

THz radiation has been generated using a wide variety of techniques developed over several decades. Early tabletop methods, including photoconductive antennas [102, 103] and optical rectification in nonlinear crystals [104–106], emerged in the 1980s and remain the

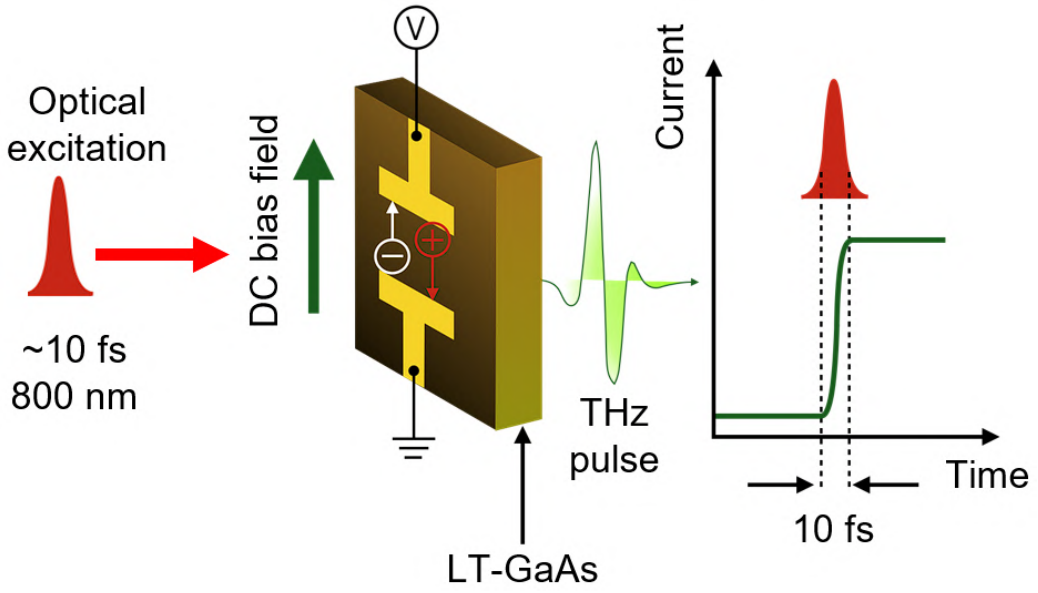

Figure 3.3: Schematic of a photoconductive antenna (PCA) used for THz pulse generation. A femtosecond optical pump pulse (∼10 fs, 800 nm) excites the LT-GaAs substrate, generating free carriers in the gap between the two electrodes. A static bias field accelerates these carriers, producing a transient photocurrent that radiates a THz pulse. The right panel shows the temporal evolution of the photocurrent: the fast rise (∼10 fs) follows the optical excitation, while the slower decay is governed by the carrier lifetime in the substrate.

most widely used approaches in ultrafast spectroscopy today. Other sources, such as free-electron lasers [107] and quantum cascade lasers [108,109], followed in subsequent decades and extended the accessible frequency range and output power well beyond what tabletop systems could achieve. In this thesis, both the photoconductive antenna (PCA) and the optical rectification method are used, as these are the most common THz generation methods employed in tabletop ultrafast experiments.

The fundamental mechanism of THz generation in PCAs relies on creating and accelerating photocarriers within a semiconductor material, driven by an ultrafast optical pulse and an applied bias electric field [110]. A typical photoconductive switch consists of a semiconductor substrate with a metallic dipole or stripline antenna structure. The substrate is a highly resistive direct bandgap material such as low-temperature-grown gallium arsenide

(LT-GaAs), InGaAs, or SI-GaAs. When an ultrafast femtosecond laser pulse illuminates the antenna gap with photon energy exceeding the semiconductor bandgap, photoexcited electron-hole pairs are generated within the photoconductive material, as shown in Figure 3.3. These photocarriers are immediately accelerated by the applied DC bias electric field $\mathbf{E}_\mathrm{b}$ across the antenna gap. This acceleration creates a transient photocurrent density $\mathbf{J}(t)$ given by

$$\mathbf{J}(t) = N(t)\, e\mu_e\, \mathbf{E}_\mathrm{b}, \tag{3.2}$$

where e is the elementary charge, μ_e is the electron mobility, and $N(t)$ is the photogenerated carrier density. The contribution of holes is neglected because the electron mobility in LT-GaAs is approximately an order of magnitude larger than the hole mobility, even accounting for the defect-induced reduction in LT-GaAs relative to bulk GaAs. The time-varying current radiates in the far field with an electric field proportional to its time derivative,

$$\mathbf{E}_\mathrm{THz}(t) \approx \frac{Ae}{4\pi\varepsilon_0 c^2 z} \frac{\partial N(t)}{\partial t}\, \mu_e\, \mathbf{E}_\mathrm{b}, \tag{3.3}$$

where A is the illuminated area, z is the far-field distance, c is the speed of light, and ε_0 is the permittivity of free space. The THz bandwidth is governed by the dynamics of $N(t)$. The fast rise of the photocarrier density, set by the laser pulse duration (10 fs here), produces high-frequency components. Meanwhile, the carrier recombination time in LT-GaAs (0.3 ps) sets the long-time decay and thereby limits the low-frequency bandwidth of the emitted pulse. Together these give a THz spectrum spanning approximately 0.1 to 3 THz for the oscillator parameters used here.

3.1.3 THz Generation via Optical Rectification

Optical rectification is a second-order nonlinear optical process in which a pulsed optical field generates a quasi-static or low-frequency polarization within a non-centrosymmetric crystal, as shown in Figure 3.4. In the linear regime, the material polarization is proportional

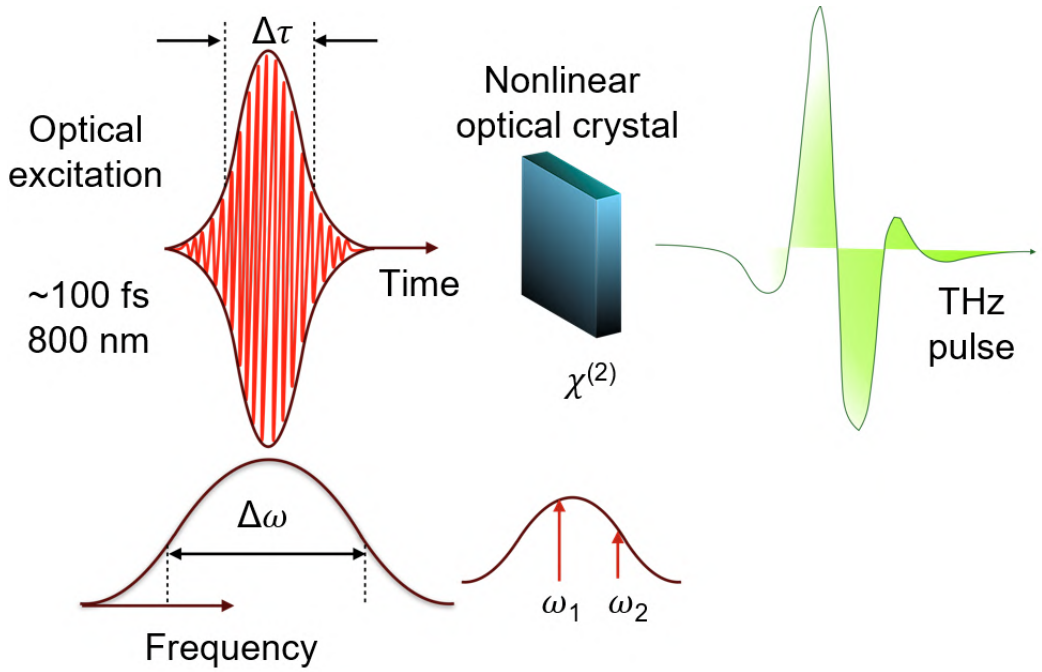

Figure 3.4: Schematic of THz pulse generation via optical rectification (OR) in a second-order nonlinear optical crystal. A femtosecond laser pulse (∼100 fs, 800 nm) with a broad optical bandwidth $\Delta\omega$ drives a $\chi^{(2)}$ nonlinear interaction within the crystal. The difference-frequency mixing between spectral components ω_1 and ω_2 within the pulse envelope produces a THz-frequency polarization that radiates a THz pulse. The temporal duration of the optical pump ($\Delta\tau$) and its spectral bandwidth ($\Delta\omega$) together determine the bandwidth and central frequency of the emitted THz radiation.

to the applied field:

$$\tilde{P}^{(1)}(t) = \varepsilon_0 \chi^{(1)} \tilde{E}(t). \tag{3.4}$$

For sufficiently strong fields, higher-order contributions become relevant and the polarization is expanded as [111]

$$\tilde{P}(t) = \varepsilon_0 \left[\chi^{(1)} \tilde{E}(t) + \chi^{(2)} \tilde{E}^2(t) + \chi^{(3)} \tilde{E}^3(t) + \cdots \right], \tag{3.5}$$

where $\chi^{(1)}$ is dimensionless, and $\chi^{(2)}$ and $\chi^{(3)}$ carry units of m/V and m^2/V^2 respectively, reflecting the different field orders they multiply. This $\chi^{(2)}$ and $\chi^{(3)}$ are the second- and third-order susceptibilities. Optical rectification is governed by $\chi^{(2)}$. For a field containing two frequency components ω_1 and ω_2, the second-order polarization contains terms at their

sum ($\omega_1 + \omega_2$), difference ($\omega_1 - \omega_2$), and second harmonics ($2\omega_1$, $2\omega_2$), as well as a DC term [111, 112],

$$\tilde{P}^{(2)}(t) = \varepsilon_0 \chi^{(2)} E_0^2 \Big[\underbrace{1}_{\text{DC}} + \underbrace{\tfrac{1}{2}\cos(2\omega_1 t) + \tfrac{1}{2}\cos(2\omega_2 t)}_{\text{SHG}} + \underbrace{\cos\big((\omega_1+\omega_2)t\big)}_{\text{SFG}} + \underbrace{\cos\big((\omega_1-\omega_2)t\big)}_{\text{DFG}} \Big]. \tag{3.6}$$

Optical rectification is the special case of difference frequency generation where $\omega_1 \approx \omega_2$. This produces a quasi-DC or low-frequency polarization that is the origin of THz radiation. The THz spectrum generated by this method is inversely proportional to the temporal pulse width of the fundamental beam.

Efficient THz generation via optical rectification requires three conditions. First, the phase-matching condition must be satisfied: the group velocity of the optical pump at frequency ω_{opt} must match the phase velocity of the generated THz wave, i.e., $n_{\text{g}}(\omega_{\text{opt}}) = n(\omega_{\text{THz}})$, so that THz contributions generated at different points in the crystal add constructively [113,114]. Second, the crystal must be non-centrosymmetric to ensure a non-zero $\chi^{(2)}$. Third, absorption in both the optical and THz ranges must be low. (110)-oriented ZnTe satisfies all three conditions for 800 nm excitation and is therefore used for THz generation in the 2D-THz experiment [115]. The generated spectrum spans 0.1 to 3 THz.

3.1.4 THz Detection via Electro-Optic Sampling

There are many ways to detect THz radiation. Bolometers and pyroelectric detectors capture the irradiated power but discard all phase information. To preserve the phase, electro-optic sampling (EOS) is used. EOS is a phase-sensitive detection technique. A THz pulse and a near-infrared probe pulse are spatially and temporally overlapped in an electro-optic crystal. By scanning their relative delay, the THz waveform is measured stroboscopically in the time domain with subpicosecond resolution.

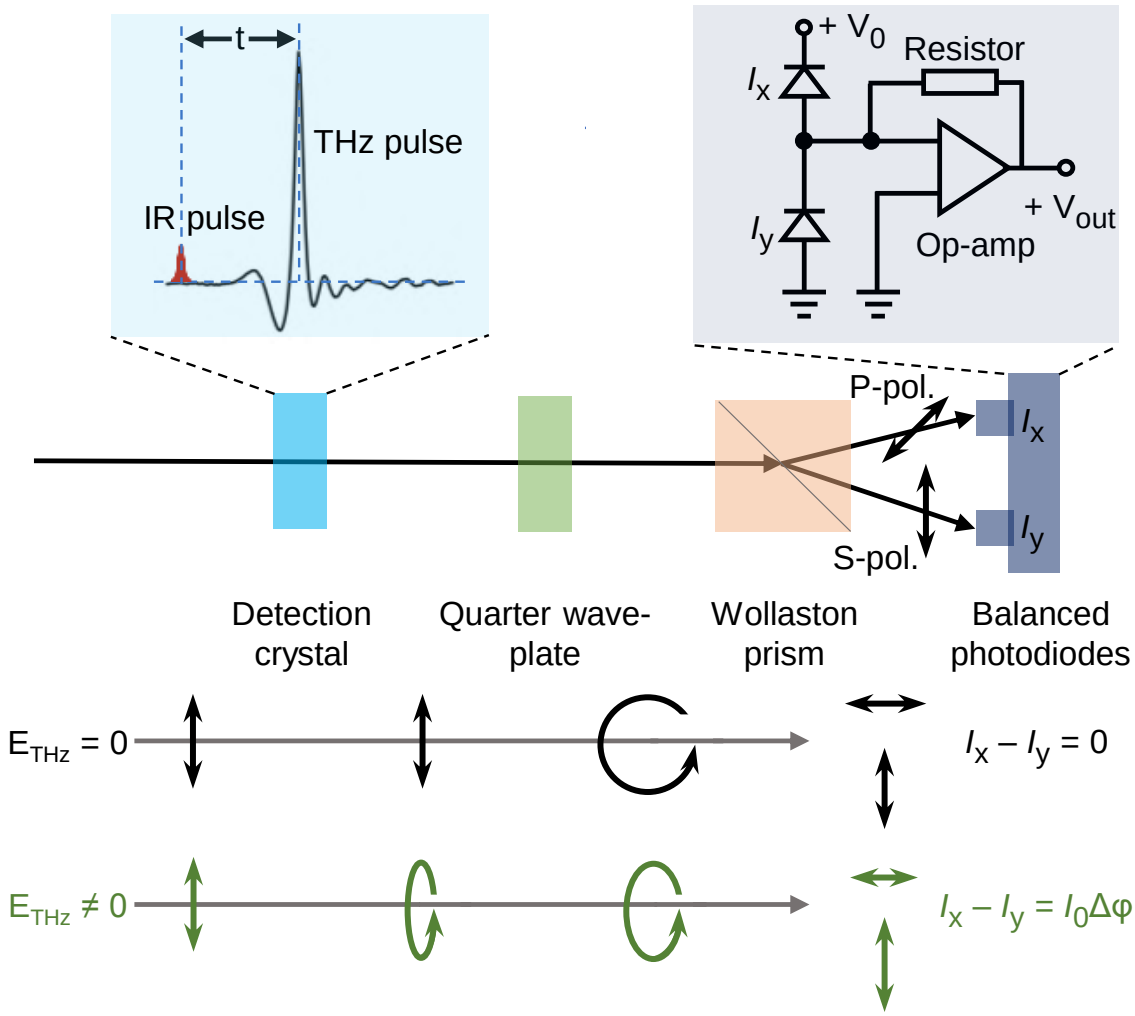

Figure 3.5: Schematic of electro-optic (EO) sampling for THz pulse detection. The probe (IR) pulse and THz pulse are temporally overlapped in the detection crystal, where the THz electric field induces a birefringence proportional to its instantaneous amplitude. The resulting ellipticity of the probe beam is analysed by a quarter-wave plate and Wollaston prism, which split the beam into its p- and s-polarised components directed onto a pair of balanced photodiodes. The difference signal $I_x - I_y$ is zero in the absence of a THz field ($E_{\mathrm{THz}} = 0$) and becomes proportional to the induced phase shift $I_0\Delta\varphi$ when the THz field is present ($E_{\mathrm{THz}} \neq 0$). By scanning the time delay t between the IR and THz pulses, the complete THz waveform is reconstructed point by point.

The Pockels effect is the cornerstone of EOS [115]. When the THz electric field E_{THz} is applied to the electro-optic crystal, it induces a birefringence that modifies the refractive

index as

$$\Delta n = n_0^3 \, r^{\mathrm{EO}} \, E_{\mathrm{THz}}, \tag{3.7}$$

where n_0 is the unmodified refractive index and r^{EO} is the effective electro-optic tensor coefficient. Only non-centrosymmetric crystals have a non-zero r^{EO}.

In the absence of a THz pulse, the polarization of the sampling beam remains unchanged after passing through the detection crystal. The quarter-wave plate, aligned with its optic axis at 45° to the probe polarization, converts the linearly polarized sampling beam into a circularly polarized beam. The Wollaston prism then splits this into two orthogonally polarized beams of equal intensity, measured by a balanced photodiode. The output of the balanced photodiode is zero. When a THz pulse is present, the induced birefringence converts the circular polarization into an elliptical one, creating an imbalance between the two polarization components. The balanced photodiode output becomes non-zero. The amplitude and phase of the THz electric field are related to the measured imbalance by [113]

$$E_{\mathrm{THz}} = \frac{\Delta I}{I} \cdot \frac{\lambda_{\mathrm{L}}}{2\pi L \, r^{\mathrm{EO}} \, n_0^3}, \tag{3.8}$$

where ΔI is the difference signal between the two photodiodes, I is the total intensity of the sampling beam, L is the thickness of the detection crystal, and λ_{L} is the wavelength of the sampling beam.

The THz-TDS technique described in this section gives access to the linear electromagnetic response of the metamaterial samples studied in this thesis. It provides the transmittance spectra used to identify the EIT window, extract the coupled oscillator parameters, and characterize the phonon resonance of the $MAPbI_3$ film. However, the linear transmittance is a time-averaged quantity. It cannot reveal how long the coherence between the bright and dark resonator modes persists, or separate the contributions of energy relaxation and dephasing to the EIT linewidth. Accessing those quantities requires driving the system into the nonlinear regime and measuring the response with a phase-sensitive two-dimensional

technique. This is what two-dimensional THz spectroscopy achieves, and it is described in the following section.

3.2 Two-Dimensional Terahertz Spectroscopy

Two-dimensional coherent THz spectroscopy is a nonlinear optical technique that maps the third-order response of a system onto a two-dimensional frequency plane [95, 115]. It was first demonstrated in the context of semiconductor quantum wells [116, 117] and has since been extended to quantum cascade structures [118], magnons [119, 120], superconductors [121, 122], and other quantum materials [95, 123, 124]. Unlike conventional pump-probe spectroscopy, which collapses all dynamics onto a single time axis, 2D-THz spectroscopy correlates two independent time variables. This correlation separates different nonlinear interaction channels into distinct spectral positions and allows the population relaxation time and the coherence lifetime to be extracted from the same measurement, on the same sample, under the same excitation conditions.

A key advantage of driving the system with THz pulses rather than optical pulses is substrate transparency. THz photon energies lie far below the bandgap of common substrates such as quartz and silicon. No free carriers are generated in the substrate during the measurement. The nonlinear signals therefore originate entirely from the metallic resonators of the metamaterial. This is fundamentally different from optical pump-THz probe (OPTP) spectroscopy, where the optical pump excites substrate carriers and the measured signal is a convolution of substrate and resonator dynamics. The 2D-THz approach provides a substrate-free window into the coherent dynamics of the coupled resonator system.

3.2.1 Experimental Setup

The 2D-THz experiment is carried out by generating two co-propagating, phase-locked THz pulses separated by a controllable delay time τ. Both pulses, denoted $\mathbf{E}_{\mathrm{A}}^{\mathrm{in}}(t,\tau)$ and $\mathbf{E}_{\mathrm{B}}^{\mathrm{in}}(t)$,

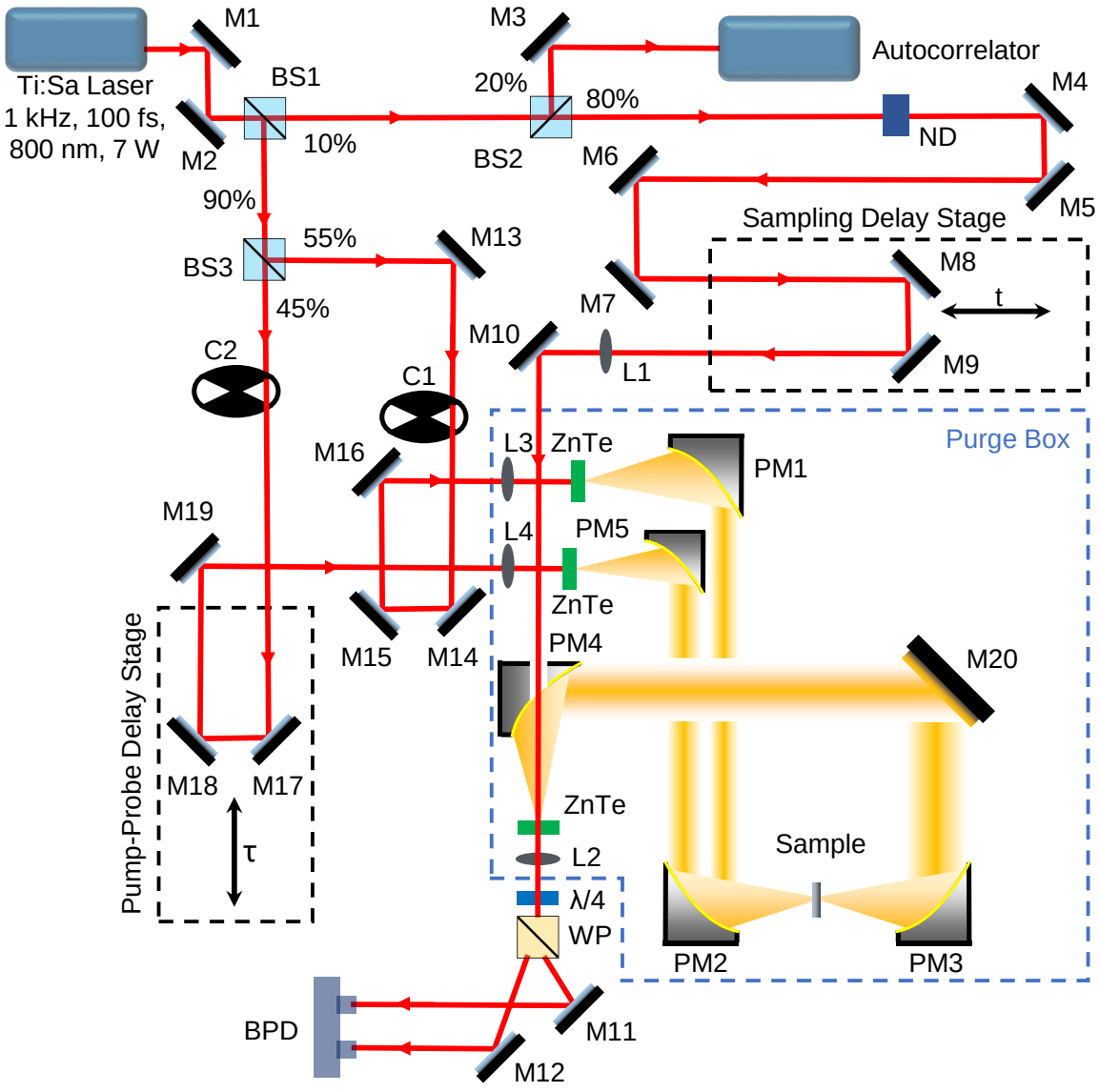

Figure 3.6: Schematic of the 2D THz experimental setup: M1-20 (mirrors); BS1-3 (beam-splitters); ND: (Neutral density filter); PM1-5 (parabolic mirrors); L1-4 (plano-convex lenses); C1-2 (choppers); DS1-2 (delay stages); HDP (High-Density Polyethylene); $\lambda/4$ (quarter-wave plate); WP (Wollaston prism); BPD (balanced photodiode); ZnTe (Zinc Telluride generation and detection crystals); t (real time); τ (delay time); Blue-dashed line (Purge box).

are produced by optical rectification of 100 fs laser pulses centred at 800 nm in two separate (110)-oriented ZnTe crystals of 0.5 mm thickness. The two driving optical pulses are derived from the same Ti:Sapphire laser and are therefore phase-locked. The generated THz

pulses maintain a well-defined and stable phase relationship throughout the measurement. The relative delay τ between the arrival of the two THz pulses at the sample is controlled by a precision mechanical delay stage. Pulse A is scanned from large negative delays (arriving well before pulse B) through zero delay and into the positive regime (pulse B arriving first).

The two pulses interact with the EIT metamaterial sample in a collinear geometry. In non-collinear optical 2D spectroscopy, the four third-order signals are emitted in distinct phase-matched directions, which separates them spatially. At THz frequencies, however, the long wavelength makes phase-matched beam separation geometrically impractical. The collinear configuration is therefore the standard choice for THz experiments. In this geometry, all nonlinear signal components are emitted in the forward direction alongside the transmitted linear signals. They are separated from each other in the two-dimensional frequency plane after Fourier analysis, rather than spatially.

Detection is performed by free-space electro-optic sampling in a composite ZnTe crystal consisting of a 0.5 mm thick (110)-oriented crystal optically bonded to a 2 mm thick (100)-oriented ZnTe crystal. The thin (110) layer provides the electro-optic sensitivity needed for THz detection. The amplitude condition $|\mathbf{E}_\mathrm{B}| > |\mathbf{E}_\mathrm{A}|$ is maintained throughout the experiment. All measurements are performed at room temperature in a nitrogen-purged enclosure to eliminate water vapour absorption lines.

3.2.2 Extraction of the Nonlinear Signal

For delay times $\tau < 0$, when pulse A arrives at the sample well before pulse B, each THz pulse independently excites the EIT metamaterial. The system responds linearly to each pulse separately, and no interaction between them occurs. When both pulses are present simultaneously near $\tau = 0$, the combined field drives the system into the nonlinear regime. Nonlinear currents are induced in the coupled resonator system that depend on the simultaneous presence of both fields. The nonlinear signal $\mathbf{E}_\mathrm{NL}(t, \tau)$ is isolated from the total trans-

mitted waveform using the three-measurement subtraction scheme. At each delay value τ, three separate waveforms are recorded in sequence. The first is $\mathbf{E}_{\mathrm{A}}(t,\tau)$, the transmitted field when only pulse A is incident on the sample. The second is $\mathbf{E}_{\mathrm{B}}(t)$, the transmitted field when only pulse B is incident. The third is $\mathbf{E}_{\mathrm{AB}}(t,\tau)$, the transmitted field when both pulses are incident simultaneously. The nonlinear signal is then constructed as [95]

$$\mathbf{E}_{\mathrm{NL}}(t,\tau) = \mathbf{E}_{\mathrm{AB}}(t,\tau) - \mathbf{E}_{\mathrm{A}}(t,\tau) - \mathbf{E}_{\mathrm{B}}(t). \tag{3.9}$$

This subtraction is exact under the assumption that the linear responses to each individual pulse are additive. All terms that arise from single-pulse interactions are cancelled. What remains are only the terms that require the simultaneous presence of both pulses. These are the third-order $\chi^{(3)}$ nonlinear contributions that encode the mutual perturbation of the resonator dynamics by the two-pulse sequence.

The subtraction in Eq. 3.9 removes the entire linear response to each pulse by construction. The residual $\mathbf{E}_{\mathrm{NL}}$ therefore contains only those contributions that require the simultaneous presence of both pulses. Three conditions ensure that this residual is dominated by the third-order nonlinear susceptibility $\chi^{(3)}$.

First, even order nonlinearities vanish by symmetry. The rod SRR unit cell is centrosymmetric along the polarisation direction of the incident THz field. The rod is a straight bar symmetric under inversion along the $\mathbf{E}$ field axis, and the SRR pair is placed symmetrically on either side. For any centrosymmetric structure the polarisation obeys $P(-E) = -P(E)$, which forces all even order susceptibilities $\chi^{(2)}$, $\chi^{(4)}$, and so on to vanish identically. This is a geometric property of the unit cell and does not depend on whether the rod and SRR resonate at the same frequency or at different frequencies.

Second, higher odd-order terms ($\chi^{(5)}$, $\chi^{(7)}$, and so on) are negligible at the incident field strengths used in this work. As discussed in Section 6.5, the third-order nonlinearity in this system does not originate from any anharmonic term in the Hamiltonian. It emerges from

the repeated action of the field matter commutator $[\hat{H}_{\text{int}}, \hat{\rho}]$ in the Liouville von Neumann equation: three successive field interactions produce the third-order signal, and five would be required to produce a fifth-order signal. As noted in Section 2.1, the density matrix perturbation theory underlying this treatment is valid when the Rabi frequency Ω_{R} remains well below the damping rates γ of the system ($\Omega_{\text{R}} \ll \gamma$). At the peak field strengths used here ($|\mathbf{E}_{\text{A}}| = 20\,\text{kV/cm}$, $|\mathbf{E}_{\text{B}}| = 40\,\text{kV/cm}$), this condition is comfortably satisfied. This is confirmed directly by the measured 2D Fourier spectrum, which shows no signal at any frequency coordinate where a fifth order process would appear, such as $(3\nu_0,\, \nu_0)$ or $(\nu_0,\, 3\nu_0)$.

Third, each individual pulse drives only a linear response. Both $\mathbf{E}_{\text{A}}(\omega)$ and $\mathbf{E}_{\text{B}}(\omega)$ are quantitatively reproduced by the linear coupled oscillator model of Chapter 2 with no free parameters beyond those obtained from the reference measurement. This confirms that no single beam nonlinear artefact contaminates the subtraction.

The coupled system's eigenstates are the bright and dark modes of the EIT response, described by the three-level Λ type Hamiltonian of Chapter 6. The subtraction scheme operates on this coupled system as a whole. Changing the bare frequencies of the individual resonators shifts the positions of the $\chi^{(3)}$ peaks in the 2D frequency map $(\nu_t,\, \nu_\tau)$ by modifying the dressed state splitting, but it does not create any new nonlinear order. This is confirmed by the data: all four observed nonlinear peaks sit at the coupled EIT frequency $\nu_0 = 1.27\,\text{THz}$ along the detection axis and at $\nu_\tau = 0$, $-\nu_0$, $+\nu_0$, and $-2\nu_0$ along the excitation axis, exactly as predicted by the third-order density matrix simulation of Section 6.5. No additional peaks appear anywhere in the 2D map.

3.2.3 Two-Dimensional Fourier Analysis

The nonlinear signal $\mathbf{E}_{\mathrm{NL}}(t,\tau)$ depends on two independent time variables: the real time t and the inter-pulse delay τ. A two-dimensional Fourier transform with respect to both gives

$$\tilde{\mathbf{E}}_{\mathrm{NL}}(\nu_t,\nu_\tau) = \int_{-\tau}^{\tau}\int_{-t}^{t} \mathbf{E}_{\mathrm{NL}}(t,\tau)\, e^{-i2\pi\nu_t t}\, e^{-i2\pi\nu_\tau \tau}\, dt\, d\tau, \tag{3.10}$$

where ν_t is the detection frequency and ν_τ is the excitation frequency. Because the two axes are independent, each nonlinear interaction appears at a distinct coordinate (ν_t,ν_τ) in the 2D plane. This separation is the central advantage of the method: a conventional one-dimensional pump-probe spectrum collapses the τ axis and mixes contributions from all nonlinear signals into a single spectrum in ν_t, while the 2D map resolves them simultaneously. The four third-order nonlinear signals accessible in this collinear geometry can be identified from their positions along the excitation axis. Two pump-probe signals appear at $\nu_\tau = 0$ and $\nu_\tau = -\nu_0$ respectively; both encode the population relaxation time T_1 in the decay of their envelope along τ. Two photon-echo signals appear at $\nu_\tau = +\nu_0$ and $\nu_\tau = -2\nu_0$; both encode the coherence lifetime T_2 in the decay of their oscillatory envelope along τ. The physical origin of each signal, the specific pulse-ordering sequences that generate them, and the quantitative extraction of T_1, T_2, and the pure dephasing time T_φ from their time-domain traces are discussed in detail in Chapter 6.

The two techniques described in this chapter are used at different stages of the experimental work. THz-TDS provides the linear characterization of the metamaterial resonances and the phonon mode that forms the basis of Chapter 5. 2D-THz spectroscopy is then applied to the bare EIT metamaterial in Chapter 6 to access the coherent dynamics that the linear measurement cannot resolve. Together they give a complete picture of both the spectral and dynamical properties of the system.

Chapter 4

Numerical Simulation and Fabrication

4.1 Numerical Simulation

The design and optimization of THz metamaterial resonators depend critically on numerical electromagnetic simulation. Analytical models such as the coupled oscillator framework used in Chapter 2 capture the resonance physics but do not predict the absolute resonance frequencies, near-field distributions, or coupling coefficients from geometry alone. Full-wave simulation fills this gap by solving Maxwell's equations over the complete three-dimensional unit cell geometry, giving access to transmittance spectra, field maps, and S-parameters that can be directly compared with experiment. All simulations in this thesis are performed using CST Microwave Studio, a commercially available electromagnetic solver.

The core numerical method in CST is the Finite Integration Technique (FIT), which discretizes the integral form of Maxwell's equations directly on a computational mesh. Unlike finite-difference methods that approximate derivatives, FIT evaluates field integrals over each mesh cell and ensures that the discrete analogues of flux conservation laws are satisfied exactly on the grid, regardless of cell size. In the special case of a uniform Cartesian hexahedral mesh, FIT reduces to the standard FDTD method, but the tetrahedral meshing used by the frequency-domain solver allows the geometry to be represented more accurately at curved and slanted boundaries. The integral form of Maxwell's equations that FIT

discretizes is [125]

$$\oint_S \vec{E} \cdot d\vec{S} = \int_V \left(\frac{\rho}{\varepsilon}\right) dV, \tag{4.1}$$

$$\oint_S \vec{B} \cdot d\vec{S} = 0, \tag{4.2}$$

$$\oint_l \vec{E} \cdot d\vec{l} = \int_S \left(-\frac{\partial \vec{B}}{\partial t}\right) \cdot d\vec{S}, \tag{4.3}$$

$$\oint_l \vec{B} \cdot d\vec{l} = \int_S \left(\mu\vec{J} + \mu\varepsilon\frac{\partial \vec{E}}{\partial t}\right) \cdot d\vec{S}, \tag{4.4}$$

where $\vec{E}$ and $\vec{B}$ are the electric field and magnetic flux density, respectively, and ρ and $\vec{J}$ are the free charge and current densities. The symbols $\oint_S$ and $\oint_l$ denote the closed surface and line integrals, respectively.

In the metamaterial simulation, CST offers a Computer Aided Design (CAD) environment to sketch the desired meta-structures. For this simulation, CST provides two types of solvers: the transient solver and the frequency-domain solver. Both use different types of approximations and appropriate boundary conditions to solve the discretized Maxwell equations. The transient solver works best for electrically large structures because it captures the broadband frequency response of a device in a single simulation run. The frequency-domain solver is better suited for electrically small, sub-wavelength structures. Instead of covering the whole spectrum at once, it calculates the response point by point at each frequency and is particularly efficient for simulating narrow resonance features [126]. CST provides an extensive library of materials including metals such as gold, aluminum, chromium, and nickel, dielectrics such as quartz and silicon, and polymers such as polyimide. CST also allows users to define custom materials by assigning frequency-dependent dispersion parameters. Several predefined dispersion models, such as the Drude and Lorentz models, are available to accurately reproduce material response in specific frequency ranges. While real materials exhibit frequency-dependent conductivity, the CST material library generally

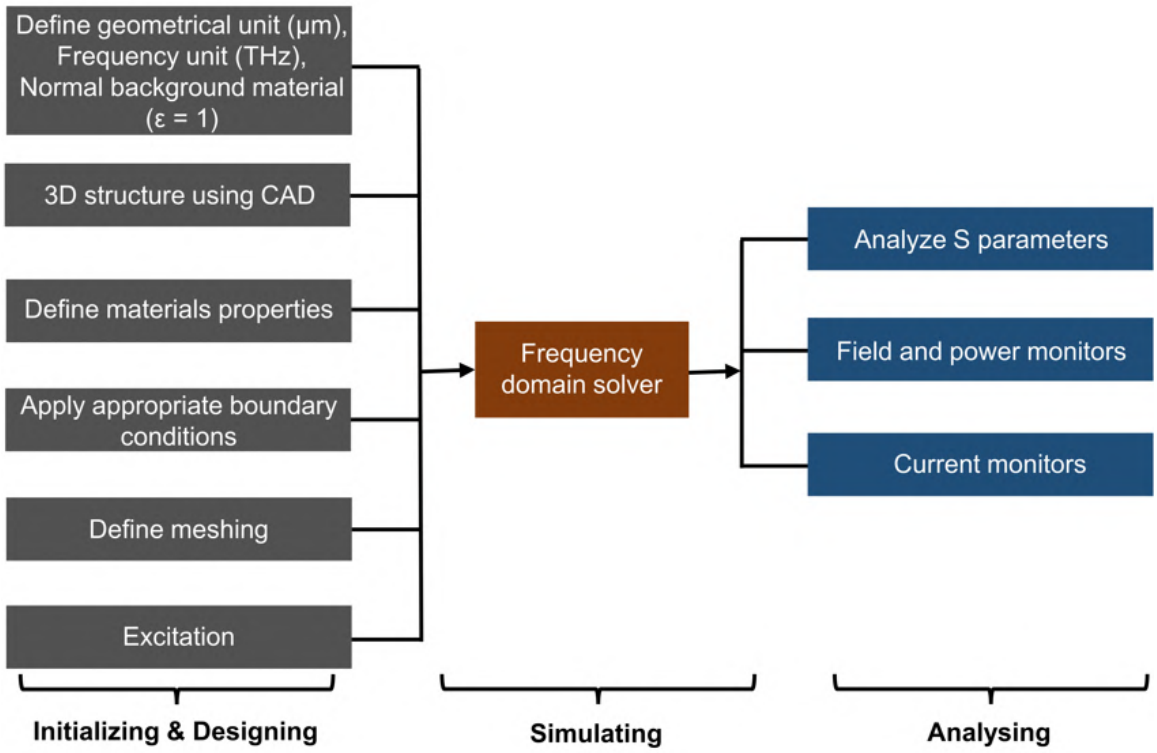

Figure 4.1: Flowchart illustrating the workflow for designing and simulating a THz metasurface in CST Microwave Studio, from geometry definition and material assignment through boundary conditions and meshing to S-parameter extraction and field analysis.

characterizes them using DC conductivity values. This approach provides a reasonable approximation at THz frequencies, particularly for thin metallic films. Figure 4.1 presents a flowchart outlining the steps for initializing, designing, simulating, and analyzing the electromagnetic model of the metasurface.

In this work, we use the frequency-domain solver. After the metamaterial unit cell is designed with the required dimensions and the simulation frequency range is set, the next step is to apply appropriate boundary conditions so that the periodic nature of the structure is accurately captured. In the frequency-domain solver, the *xy*-plane is assigned Unit Cell boundary conditions to model the metamaterial unit cell as an infinite periodic array while accounting for possible edge effects. Along the *z*-direction, an open boundary is used since it corresponds to the propagation axis of light. Specifically, at $z_{\max}$, the open (add space)

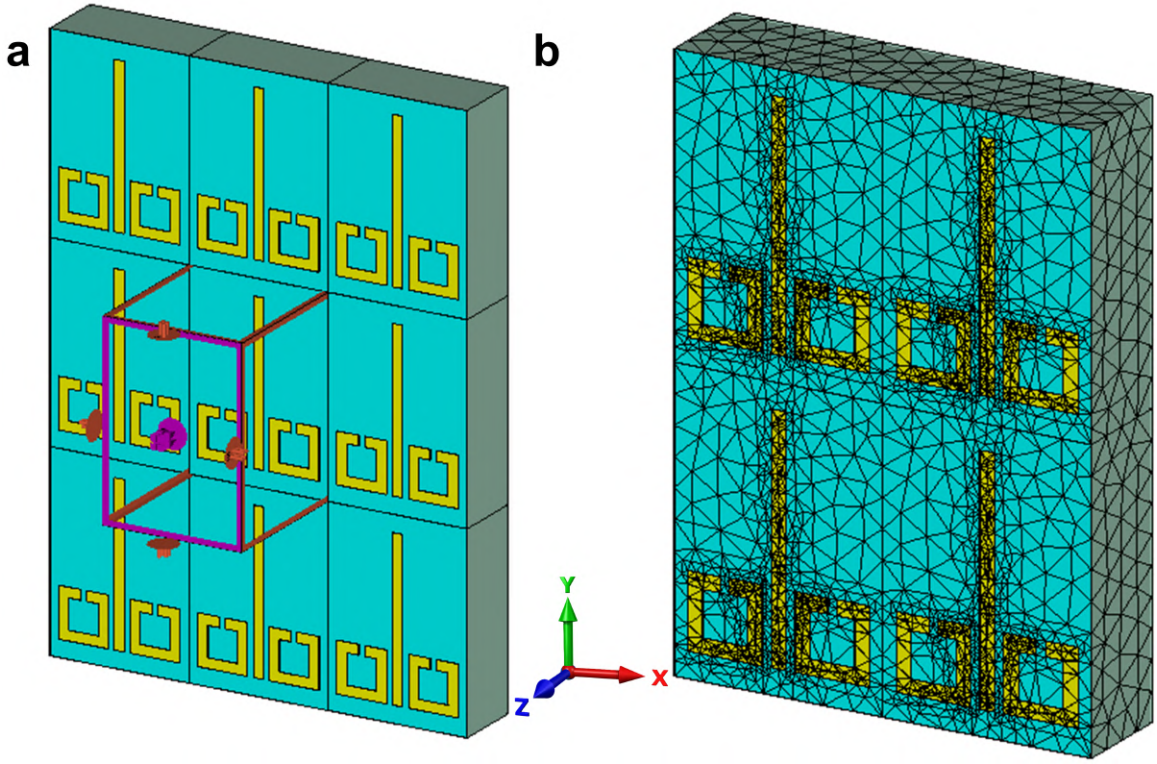

Figure 4.2: Interface parameter windows of the CST-MWS frequency-domain solver illustrating the setup of **(a)** boundary conditions and **(b)** the mesh adaptation process.

boundary condition is applied to ensure that fringing fields generated near the metallic surface at resonance are not artificially reflected back into the simulation domain, as shown in Figure 4.2. To suppress these unwanted fringing field effects, a spacing of about $\lambda/8$ is introduced between the structure and the open boundary. This is also the default setting in CST. After defining the boundary conditions, CST solves the integral form of Maxwell's equations for a single unit cell by discretizing it into smaller tetrahedral elements. This process is called meshing. Figure 4.2 illustrates the meshing of the metamaterial structure. For accurate results, the mesh size must be smaller than the smallest structural feature and also smaller than one-quarter of the characteristic wavelength. A finer mesh improves accuracy but increases computational cost. The choice of mesh size is therefore left to the user, depending on the required balance between resolution and computational efficiency.

In the frequency-domain simulation, once the mesh is defined, the integral form of Maxwell's equations is Fourier transformed, and the time derivative operator is replaced by its Fourier equivalent,

$$\frac{\partial}{\partial t} \longrightarrow i\omega. \tag{4.5}$$

The transformed equations are solved mesh by mesh, separately for each frequency, across the entire selected frequency range. The computed output is stored in the scattering matrix, known as the S-matrix or S-parameters, which contains all complex transmission and reflection coefficients for all calculated modes. The S-parameters relate the outgoing wave O and the incoming wave I through the matrix equation

$$\begin{bmatrix} O_1 \\ O_2 \end{bmatrix} = \begin{bmatrix} S_{11} & S_{12} \\ S_{21} & S_{22} \end{bmatrix} \begin{bmatrix} I_1 \\ I_2 \end{bmatrix}, \tag{4.6}$$

where subscripts 1 and 2 correspond to port 1 and port 2, respectively. The coefficient S_{11} is the reflection coefficient at port 1, S_{12} is the transmission coefficient measured at port 1 for excitation from port 2, S_{21} is the transmission coefficient at port 2, and S_{22} is the reflection coefficient at port 2. CST also provides direct visualization of 2D and 3D electromagnetic field distributions within the simulation domain. From these field distributions, one can extract local charge distributions and surface current densities at any chosen frequency. For metamaterial structures, where both electric and magnetic responses can be present, these field maps play a crucial role in analyzing the resonant behavior and the nature of near-field coupling within the system.

4.1.1 Comparison Between Simulation and Experiment

Although the simulated spectra closely follow the experimentally measured results, small differences between the two are unavoidable. Numerical modeling is always based on certain idealizations, whereas experiments inherently include imperfections and uncontrolled factors.

One primary source of deviation arises from the material parameters used in CST. The permittivity, conductivity, and loss parameters defined in the simulation are typically taken from literature values or fitted data. These may not exactly match the properties of the fabricated samples, especially in the THz regime where dispersion and loss are highly sensitive to processing conditions. Another factor is the difference between the simulated environment and the actual experimental setup. Simulations assume ideal boundary conditions, perfectly homogeneous substrates, and well-defined excitation fields. Real measurements may be influenced by substrate inhomogeneity, surface roughness, finite sample size, alignment errors, or background noise. Each of these can slightly modify the observed spectral response. Fabrication-related variations also contribute to discrepancies. During lithography and metal deposition, small deviations in feature size, thickness, and edge definition are inevitable. Even a minor change in resonator dimensions can lead to a noticeable shift in resonance frequency or a change in linewidth. Additionally, numerical errors associated with mesh discretization introduce slight differences, since the accuracy of the frequency-domain solver depends on the mesh density and convergence criteria used.

Despite these limitations, CST Microwave Studio remains a reliable and powerful tool for modeling metamaterial resonators. When appropriate material models, boundary conditions, and mesh settings are carefully chosen, the frequency-domain solver provides excellent agreement with experiments. Its ability to resolve fine structural features and accurately capture electromagnetic interactions at sub-wavelength scales makes it indispensable for the design and analysis of THz metamaterials.

4.1.2 Modelling the $MAPbI_3$ Phonon Mode

The simulations described so far treat the substrate and the metallic resonators as the only constituents of the unit cell. For the phonon-polariton coupling study in Chapter 5, an additional step is required: the dielectric response of the $MAPbI_3$ film must be introduced

into the simulation in a way that accurately captures the phonon resonance near 0.97 THz.

The standard approach is to assign a frequency-dependent permittivity to the $MAPbI_3$ layer using the Lorentz oscillator model. In CST, this is implemented by defining a dispersive material with a Lorentz pole centered at the transverse optical (TO) phonon frequency. The complex permittivity of the model takes the form [127]

$$\varepsilon(\omega) = \varepsilon_\infty \left(1 + \frac{\omega_{\mathrm{LO}}^2 - \omega_{\mathrm{TO}}^2}{\omega_{\mathrm{TO}}^2 - \omega^2 - i\Gamma\omega}\right), \tag{4.7}$$

where ε_∞ is the high-frequency permittivity, ω_{TO} and ω_{LO} are the transverse and longitudinal optical phonon frequencies, and Γ is the phonon damping rate. The Lorentz model is well established for polar crystals and accurately reproduces the Reststrahlen band between ω_{TO} and ω_{LO}, where the real part of $\varepsilon(\omega)$ becomes negative and the material is strongly reflective.

In this work, the dielectric constants of quartz and $MAPbI_3$ are set to 4.41 [128,129] and $6.5 + i0.05$ [130, 131], respectively, near 1 THz. The phonon parameters for $MAPbI_3$ are extracted from a separate THz-TDS measurement of the bare perovskite film on quartz. The simulated transmittance of the film reproduces the absorption feature at 0.97 THz, confirming that the Lorentz parameters are correctly assigned. Two simulations are then performed for each resonator geometry: one with the phonon mode deactivated, by setting $\omega_{\mathrm{LO}} = \omega_{\mathrm{TO}}$ so that the Lorentz pole vanishes, and one with the phonon mode active. Comparing the two spectra isolates the contribution of the phonon coupling and allows the Rabi splitting to be identified directly from the simulation output.

An important consequence of the $MAPbI_3$ film is a redshift of the metamaterial resonance even when the phonon mode is deactivated. This shift arises from the increase in the effective dielectric constant of the medium surrounding the resonators. Simulations show a typical redshift of approximately 200 GHz relative to the bare structure, as shown in Figure A.1. For this reason, the EIT peak of the bare metamaterial is pre-designed at

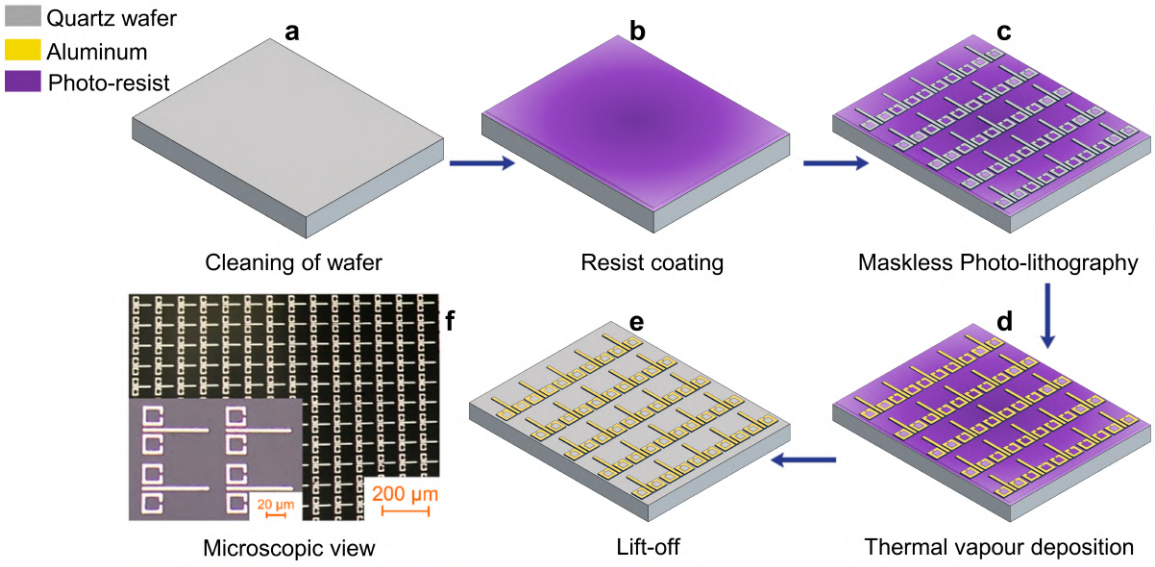

Figure 4.3: **(a–e)** Fabrication process based on maskless photo-lithography and thermal vapour deposition. **(f)** Optical microscope image of the fabricated EIT structure with 3 μm gap size.

1.3 THz, so that after integration with $MAPbI_3$ it aligns closely with the phonon frequency near 1.0 THz and ensures optimal hybridization.

4.2 Design and Fabrication

We fabricated the metamaterial design on a *z*-cut quartz substrate with dimensions of 8 mm $\times$ 8 mm $\times$ 0.5 mm using maskless lithography. The *z*-cut quartz substrate ensures a low-loss and stable platform for clean resonance features and minimizes background absorption. To fabricate the metamaterial structure, we used a positive photo-resist and NaOH developer. Initially, the photo-resist is spin-coated on the quartz substrate at 3000 rpm for 40 s. After that, the substrate is baked at 80 °C for 1 minute. The structure is then exposed using a 360 nm maskless lithography laser. Following the exposure, the sample is immediately placed in the NaOH developer solution for approximately 7 s. Afterward, to remove photo-resist residue, the samples are treated in a plasma chamber. In the thermal vapour deposition

chamber, clean samples are coated with an aluminum (Al) layer of 120 nm thickness, followed by lift-off in N-Methyl-2-Pyrrolidone (NMP). The Al-layer thickness is larger than its skin depth across the spectral range of 0.5–1.6 THz [132]. As shown in Figure 4.3, the unit cell geometry and the uniformity of the fabricated metamaterial structure are confirmed over an area larger than the THz spot size, ensuring homogeneous excitation across the array. Note that other substrate materials with different refractive indices can also be used. However, this would shift the resonance positions and affect the results qualitatively. Proper re-optimization of the resonator dimensions would be required in that case. The fabricated geometric parameters of the unit cell are summarized in Table 4.1.

Table 4.1: Geometric parameters of the rod-SRR EIT metamaterial unit cell.

Parameter	Symbol	Value
Rod length	L	75 µm
SRR arm length	l	23.5 µm
Linewidth	w	5 µm
SRR gap	g	3 µm
Rod–SRR separation	s	3 µm
Periodicity (x)	p_x	67 µm
Periodicity (y)	p_y	93 µm
Al film thickness	t	120 nm

4.2.1 Deposition of the $MAPbI_3$ Perovskite Layer

The $MAPbI_3$ film is deposited directly onto the fabricated metamaterial surface by a single-step antisolvent spin-coating procedure. A precursor solution of methylammonium iodide (MAI, 0.75 M) and lead iodide (PbI_2, 0.75 M) in equimolar ratio is prepared in a 3:1 (v/v) mixture of dimethylformamide (DMF) and dimethyl sulfoxide (DMSO). The DMSO is included to slow crystallization and improve film uniformity. The solution is stirred at 60 °C until fully dissolved and filtered through a 0.45 µm PTFE membrane filter to remove particulates before use.

All deposition steps are carried out inside a nitrogen-filled glove box ($O_2 < 0.1$ ppm, $H_2O < 0.1$ ppm) to prevent moisture exposure, which degrades $MAPbI_3$ rapidly and irreversibly. The precursor solution is dispensed onto the substrate and the substrate is spun at 2000 rpm for 10 s followed by 6000 rpm for 50 s. At 40 s after the start of spinning, 200 µL of chlorobenzene is dripped onto the spinning substrate as an antisolvent. The antisolvent extraction step rapidly removes the DMF/DMSO solvent by miscibility, inducing fast supersaturation of the perovskite precursors and nucleating a dense layer of small crystallites. The timing of the antisolvent drop at 40 s is critical: earlier addition does not allow sufficient solvent evaporation and leads to dewetting, while later addition results in incomplete solvent extraction and rough films. The coated substrate is immediately transferred to a hotplate and annealed at 100 °C for 15 min to complete crystallization and remove residual solvent. The resulting film thickness is approximately 200 nm, measured by profilometry across a scratch-edge reference on a companion substrate prepared identically.

The 200 nm thickness is chosen to balance two competing requirements. A thicker film increases the spatial overlap between the phonon-active material and the near-field region of the resonators, strengthening the coupling. However, a thicker film also introduces additional THz absorption losses and reduces the overall transmittance baseline, making it harder to resolve the transparency windows. No encapsulation layer is applied, to avoid introducing parasitic THz absorption. All THz measurements are carried out under nitrogen flow, and the samples are stored in the glove box between measurement sessions.

The fabrication and simulation methods described in this chapter provide the physical platform and the computational tools for the two experimental studies that follow. Chapter 5 uses THz-TDS and CST simulation to characterize the phonon-polariton hybridization and dual EIT response of the complete hybrid structure. Chapter 6 uses the bare metamaterial, fabricated without the perovskite layer, as the platform for 2D-THz spectroscopy.

Chapter 5

Phonon-Polariton Mediated Dual Electromagnetically Induced Transparency in a THz Metamaterial

5.1 Introduction

The scientific background in Chapter 2 established two key ideas. First, when a metamaterial resonator is brought into strong coupling with a phonon-active material, the original resonances hybridize into upper and lower polariton branches separated by a Rabi splitting. Second, when a bright radiative mode and a sub-radiant dark mode are placed in near-field proximity, their destructive interference opens an EIT-*like* transparency window in the THz transmittance spectrum. Each of these phenomena has been studied extensively in isolation. The phonon-polariton coupling has been demonstrated in individual THz resonators coupled to polar crystals and perovskite films [19, 22, 23], and EIT-*like* transparency has been engineered in a wide variety of rod-SRR metamaterial geometries [15, 76, 78–80]. Yet the physics that emerges when both mechanisms operate simultaneously within a single device has not been addressed, and it is this open question that motivates the present work.

The outcome is non-trivial and cannot be predicted from either mechanism alone. In a conventional EIT metamaterial, the transparency window arises from a single interference pathway between two resonators. When a phonon mode is introduced and the system enters the strong coupling regime, both resonators independently hybridize with the phonon. This creates four polaritonic states rather than two. Whether these states organize themselves

into new interference pathways, and whether those pathways produce distinct transparency windows, is an open question. The answer depends on the spectral overlap of the polaritonic branches, the relative strength of the bright-dark coupling compared to the phonon coupling, and the geometry of the unit cell. None of these factors can be predicted from the single-mechanism results alone.

A further motivation is tunability. Most demonstrations of EIT-*like* transparency in metamaterials operate within a fixed spectral framework. The transparency window can be shifted or suppressed, but the qualitative character of the response remains unchanged. A mechanism that genuinely transforms the response, replacing a single window with two, without any modification to the device structure, would represent a fundamentally different level of control.

This chapter addresses both aspects through a combined experimental and numerical study of a rod-SRR EIT metamaterial integrated with a thin $MAPbI_3$ perovskite film. Section 5.2 establishes the bare EIT metamaterial response and quantifies the near-field coupling between the bright and dark resonators. Section 5.3 examines the strong phonon-polariton coupling in each individual resonator. Section 5.4 presents the complete hybrid system, covering the emergence of dual transparency, field distribution analysis, group delay, energy-level interpretation, theoretical modeling, and rotational and translational tunability.

5.2 Phonon-Polariton Coupling in the EIT Metamaterial

The EIT metamaterial used in this study consists of a central rod resonator symmetrically positioned between a pair of SRRs, fabricated on a *z*-cut quartz substrate. The design and fabrication procedure are described in Chapter 4. The unit cell geometry is shown in Figure 5.1a. Under *y*-polarized THz illumination, the rod supports a dipole resonance at $f_{\mathrm{rod}} \approx 1.2$ THz

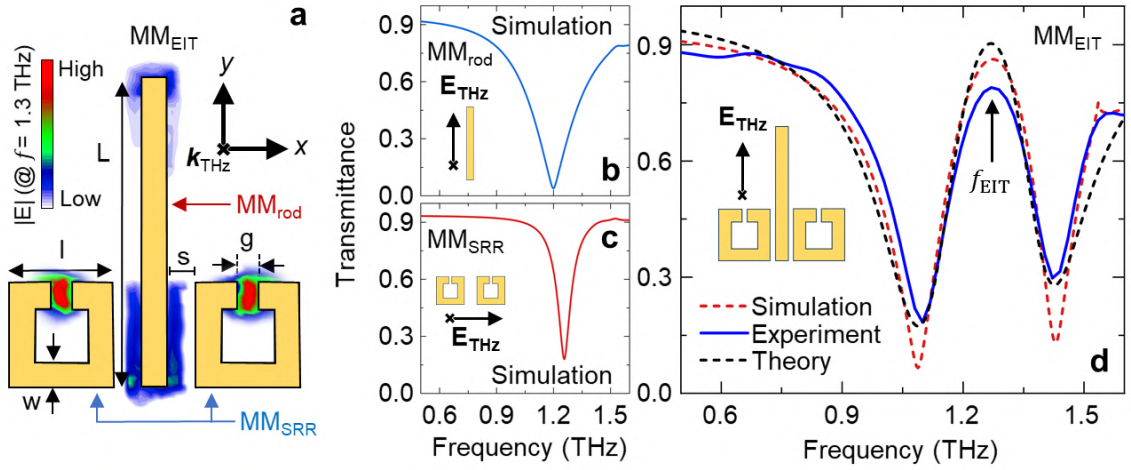

Figure 5.1: **(a)** Schematic representation of the EIT-like metamaterial unit cell consisting of a rod resonator with a pair of split-ring resonators (SRRs) on either side. Geometric parameters: $L = 75\,\mu$m, $l = 23.5\,\mu$m, $w = 5\,\mu$m, $g = 3\,\mu$m, $s = 3\,\mu$m, with periodicities of 67 μm and 93 μm along x and y, respectively. The in-plane field distribution $|\mathbf{E}| = \sqrt{|E_x|^2 + |E_y|^2}$ is shown at the EIT peak frequency of 1.3 THz. **(b)** Simulated transmittance of the rod showing its dipole resonance at 1.2 THz. **(c)** Simulated transmittance of the SRR showing its LC resonance at 1.25 THz. **(d)** Simulated (red-dashed curve), measured (blue-solid curve) and theoretically obtained (black-dashed curve) transmittance spectra of the EIT-like metamaterial that shows the EIT peak frequency at $f_{\mathrm{EIT}} = 1.3$ THz, in an excellent agreement with each other. The insets in (b-d) show the incident electric-field polarization corresponding to the metamaterial structure. Taken from Ref. [15]

and acts as the bright mode (Figure 5.1b). The structural symmetry of the SRR pair prevents its direct excitation by the same polarization. Instead, the x-component of the near-field induced by the rod drives the LC resonance of the SRR pair at $f_{\mathrm{SRR}} \approx 1.25$ THz, making it the dark mode (Figure 5.1c). The destructive interference between the two excitation pathways opens the EIT transparency window at $f_{\mathrm{EIT}} = 1.3$ THz, as shown in Figure 5.1d. The simulated, measured, and analytically modeled transmittance spectra are in excellent agreement, confirming that the observed transparency arises from coherent bright-dark mode coupling.

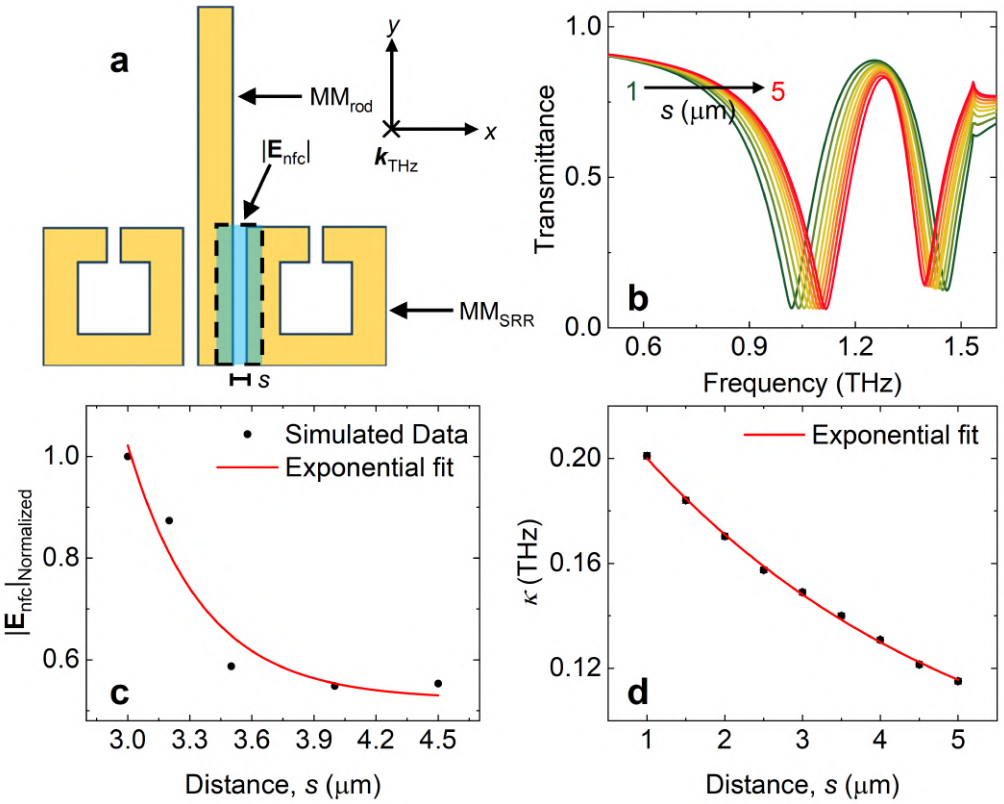

Figure 5.2: **(a)** Schematic of the EIT unit cell with the sky-blue region showing the in-plane near-field coupling zone at 1.3 THz. **(b)** Simulated transmittance as a function of inter-resonator separation s varied from 1 to 5 μm in steps of 0.5 μm. **(c)** Normalized in-plane near-field amplitude $|\mathbf{E}_{\mathrm{nfc}}|$ as a function of s. Red curve is an exponential fit. **(d)** Coupling coefficient κ as a function of s extracted by fitting Eq. (5.6) to the simulated spectra. The red curve is an exponential fit. Taken from Ref. [15].

5.2.1 Near-Field Coupling in the EIT Metamaterial

The emergence of the transparency window is governed by near-field coupling between the bright and dark resonators. Unlike far-field radiative interactions, near-field coupling is mediated by evanescent fields localized in the immediate vicinity of the resonant elements. These fields decay rapidly with distance and become significant only when the two resonators are separated by distances much smaller than the resonant wavelength.

When the rod is excited by the incident THz field, strong electric field localization develops at its ends. When the SRRs are positioned nearby, they interact with this localized field

Table 5.1: Bright and dark mode parameters (γ_b, γ_d) and near-field coupling coefficient κ extracted by fitting Eq. (5.6) to simulated EIT transmittance spectra as a function of rod-SRR separation s. The condition $\kappa^2 > \gamma_b\gamma_d$ is satisfied for all s values, confirming that the near-field coupling is strong enough to sustain a well-resolved EIT transparency window [65, 67].

Distance s (μm)	γ_b (THz)	γ_d (THz)	κ (THz)	$\gamma_b\gamma_d$ (THz^2)	κ^2 (THz^2)
1.0	0.119	0.087	0.201	0.010	0.040
1.5	0.126	0.077	0.184	0.010	0.034
2.0	0.134	0.070	0.170	0.009	0.029
2.5	0.137	0.063	0.157	0.009	0.025
3.0	0.142	0.059	0.149	0.008	0.022
3.5	0.147	0.054	0.140	0.008	0.020
4.0	0.150	0.050	0.131	0.008	0.017
4.5	0.153	0.046	0.121	0.007	0.015
5.0	0.157	0.042	0.115	0.007	0.013

through evanescent coupling. The sky-blue region in Figure 5.2a marks the zone where this energy exchange is most prominent. Energy transferred from the rod dipole to the SRR LC mode creates the conditions for destructive interference in the radiative channel, which opens the transparency window. The coupling strength depends critically on the separation s between the resonators. Moreover, Figure 5.2b shows how the transmittance changes as s is varied from 1 μm to 5 μm. As the separation increases, the transparency window progressively narrows and weakens. Both the normalized near-field amplitude (Figure 5.2c) and the extracted coupling coefficient κ (Figure 5.2d) decay exponentially with increasing s, confirming the evanescent character of the interaction. The coupling coefficient κ is extracted by fitting the analytical transmittance expression Eq. (5.6) to the simulated spectra. The fitting also yields the bright and dark mode damping rates γ_b and γ_d, the resonance frequencies, and the driving coefficient g_{dr}. Selected parameters are summarized in Table 5.1, and the remaining fitted values are presented in Figures 5.9a and 5.9b.

The data confirm that $\kappa^2 > \gamma_b\gamma_d$ not only at s $= 3$ μm but for all smaller separations as

well. This shows that the system operates in the strongly near-field coupled regime across a range of gap values, with even stronger interaction at shorter distances. In the present study, s $= 3\,\mu$m is selected due to fabrication constraints associated with the maskless photolithography process used here (described in Chapter 4). This gap still maintains sufficiently strong near-field coupling to sustain the destructive interference responsible for the EIT transparency window.

5.3 Strong Coupling and Polariton Formation

With the bare EIT response established, we now introduce the phonon mode by depositing a thin film of $MAPbI_3$ perovskite onto the fabricated metamaterial surface. The schematic structure of $MAPbI_3$ as shown in Figure 5.3a. The film deposition procedure of the TO phonon mode at 0.97 THz are described in Chapter 4. The dielectric response of $MAPbI_3$ near its phonon frequency is modeled using the Lorentz oscillator formalism introduced in Chapter 4, and the fitted parameters are used directly in the CST simulations. THz-TDS measurements of the bare $MAPbI_3$ film on quartz confirm a phonon resonance at 0.97 THz, as shown in Figure 5.3b. This is in good agreement with the simulated response, confirming that the Lorentz parameters accurately capture the phonon dielectric function.

Before examining the full hybrid system, we first analyze the coupling between the phonon and each individual metamaterial element. When the phonon mode is activated in the simulation, the rod transmittance (Figure 5.3c) and the SRR transmittance (Figure 5.3d) both show clear spectral anticrossing, signaling the formation of hybrid phonon-polaritonic states. The resulting upper and lower polariton branches are separated by a characteristic Rabi splitting. For the rod, the upper and lower polaritons appear at approximately 1.2 THz and 0.9 THz, corresponding to a Rabi splitting of about 0.31 THz. The SRR exhibits a larger splitting of about 0.37 THz, with polaritonic branches near 1.3 THz and 0.9 THz. The en-

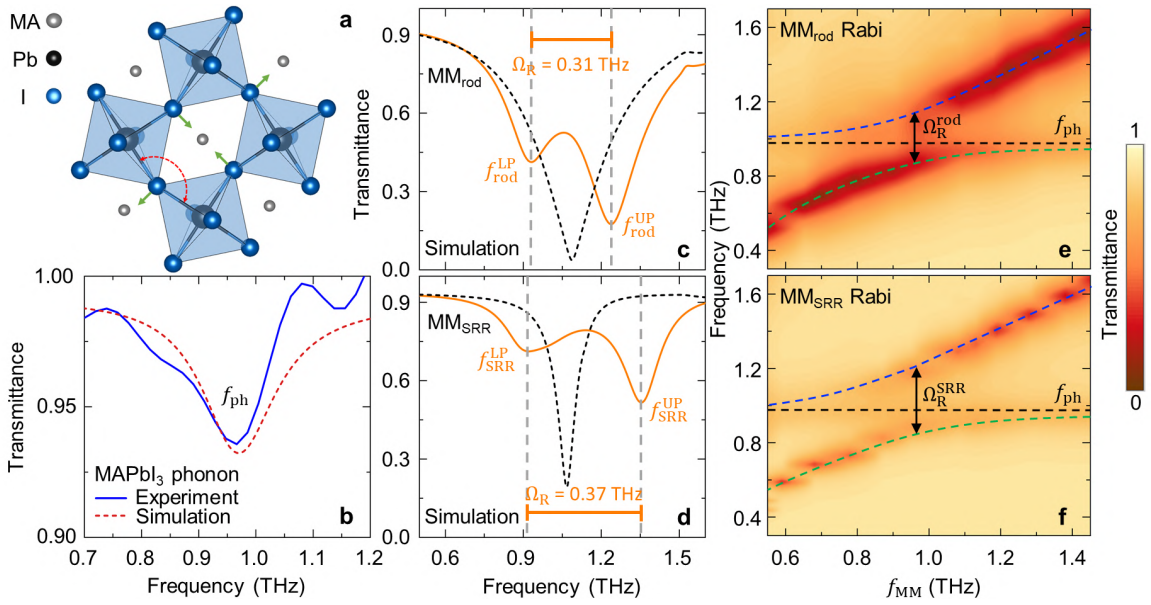

Figure 5.3: **(a)** Schematic of the $MAPbI_3$ perovskite structure showing the Pb-I-Pb bond angle distortion associated with the TO phonon mode. **(b)** Simulated (red-dashed) and measured (blue-solid) transmittance of the $MAPbI_3$ film on quartz showing the phonon at $f_{ph} = 0.97$ THz. Simulated transmittance of **(c)** the rod and **(d)** the SRR in the presence of $MAPbI_3$, showing the formation of upper (f_{MM}^{UP}) and lower (f_{MM}^{LP}) polaritons. Black-dashed curves show the resonator response without the phonon mode. Simulated 2D transmittance maps obtained by varying the resonance frequency of **(e)** the rod and **(f)** the SRR, showing the avoided crossing. Black-dashed lines mark the $MAPbI_3$ phonon at 0.97 THz. Blue and green dashed curves are guides for the upper and lower polaritonic branches, respectively. Taken from Ref. [15].

hanced splitting in the SRR case is directly attributed to the stronger electric field localization within its capacitive gap, which increases the overlap between the confined electromagnetic field and the phonon-active medium.

The dispersion behavior further substantiates the coherent character of this interaction. The two-dimensional transmittance maps in Figures 5.3e and 5.3f show clear avoided crossings as the metamaterial resonance frequency is tuned across the phonon mode. The emergence of two branches separated by a finite energy gap at resonance is the hallmark of coherent hybridization. It demonstrates that the cavity mode and the lattice vibration are no longer independent excitations but form new eigenstates of the coupled system.

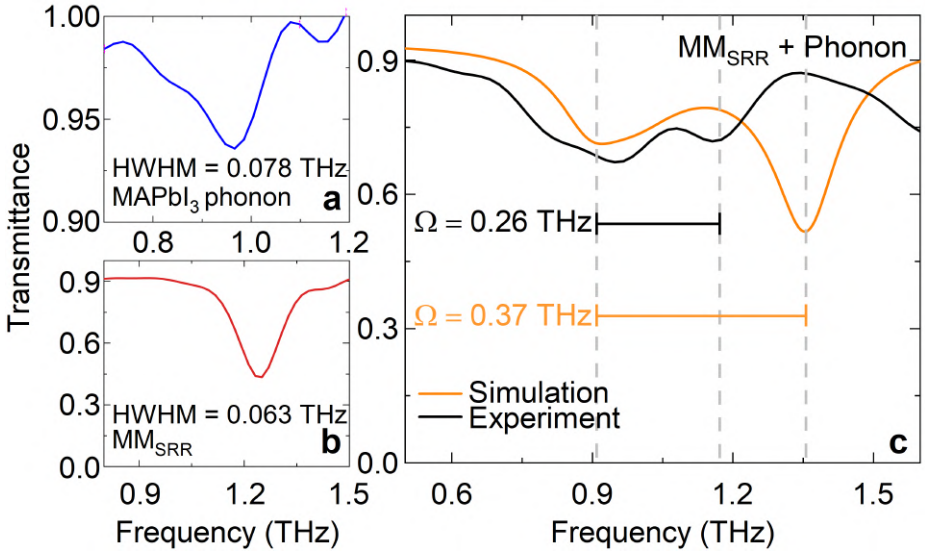

Figure 5.4: Experimentally measured transmittance spectra for **(a)** the $MAPbI_3$ phonon and **(b)** the SRR, with corresponding HWHM of 0.078 and 0.063 THz, respectively. **(c)** Simulated and experimental transmittance of the SRR in the presence of the active phonon mode, showing Rabi splittings of $\Omega_R = 0.37$ THz (simulation) and 0.26 THz (experiment). Taken from Ref. [15].

To confirm that the system operates in the strong coupling regime, we apply the coupled harmonic oscillator model. The two subsystems are represented by an effective interaction Hamiltonian of the form

$$\begin{bmatrix} E_{\mathrm{MM}} + i\hbar\Gamma_{\mathrm{MM}} & V \\ V & E_{\mathrm{ph}} + i\hbar\Gamma_{\mathrm{ph}} \end{bmatrix}, \tag{5.1}$$

where $E_{\mathrm{MM}} = 2\pi\hbar f_{\mathrm{MM}}$ is the metamaterial resonance energy, $E_{\mathrm{ph}} = 2\pi\hbar f_{\mathrm{ph}}$ is the phonon energy, $\hbar\Gamma_{\mathrm{MM}}$ and $\hbar\Gamma_{\mathrm{ph}}$ are the half-width at half-maximum (HWHM) linewidths, and V is the interaction potential responsible for coherent energy exchange. At spectral degeneracy ($E_{\mathrm{MM}} = E_{\mathrm{ph}}$), diagonalization of Eq. (5.1) yields two hybrid eigenstates separated by the Rabi splitting $\hbar\Omega_R$. The interaction potential is then

$$V = \frac{1}{2}\sqrt{(\hbar\Omega_R)^2 + (\hbar\Gamma_{\mathrm{ph}} - \hbar\Gamma_{\mathrm{MM}})^2}. \tag{5.2}$$

The strong coupling condition is $V > V_{\mathrm{st}}$, where $V_{\mathrm{st}} = \sqrt{((\hbar\Gamma_{\mathrm{ph}})^2 + (\hbar\Gamma_{\mathrm{MM}})^2)/2}$.

From the experimentally measured linewidths, we obtain $\hbar\Gamma_{\mathrm{ph}} = 0.323\,\mathrm{meV}$ and $\hbar\Gamma_{\mathrm{SRR}} = 0.261\,\mathrm{meV}$, as shown in Figures 5.4a and 5.4b, respectively. The threshold interaction strength is $V_{\mathrm{st}} = 0.294\,\mathrm{meV}$. The measured Rabi splitting of $\hbar\Omega_{\mathrm{R}} = 1.075\,\mathrm{meV}$ gives an interaction potential of $V = 0.538\,\mathrm{meV}$, which clearly satisfies $V > V_{\mathrm{st}}$. This confirms that the SRR-phonon hybrid operates in the strong coupling regime. A similar analysis for the rod-phonon system leads to the same conclusion. The rod Rabi splitting is somewhat smaller, consistent with the weaker field confinement compared to the SRR, but the interaction potential still exceeds the loss-determined threshold.

These calculations establish that both resonant elements independently form coherent phonon-polaritonic states with the $MAPbI_3$ layer. This confirmation is essential before proceeding to the full hybrid system. It ensures that the spectral modifications observed in the subsequent sections originate from genuine strong light-matter coupling rather than from a weak perturbative effect.

5.4 Hybrid Phonon-EIT System

5.4.1 Emergence of Dual Transparency

Having confirmed strong coupling in the individual subsystems, we now examine the complete hybrid configuration in which the $MAPbI_3$ phonon mode is integrated with the full EIT metamaterial cavity.

The bare EIT metamaterial is designed to produce a transparency peak at 1.3 THz. Upon deposition of $MAPbI_3$, the increased dielectric loading shifts the cavity resonance to approximately 1.08 THz, as shown in the appendix Figure A.1. This brings the EIT mode into close spectral proximity with the TO phonon at 0.97 THz, enabling strong interaction between them. The experimentally measured transmittance shows excellent agreement with simulation and theory, as shown in Figures 5.5b and 5.5c, respectively. The single trans-

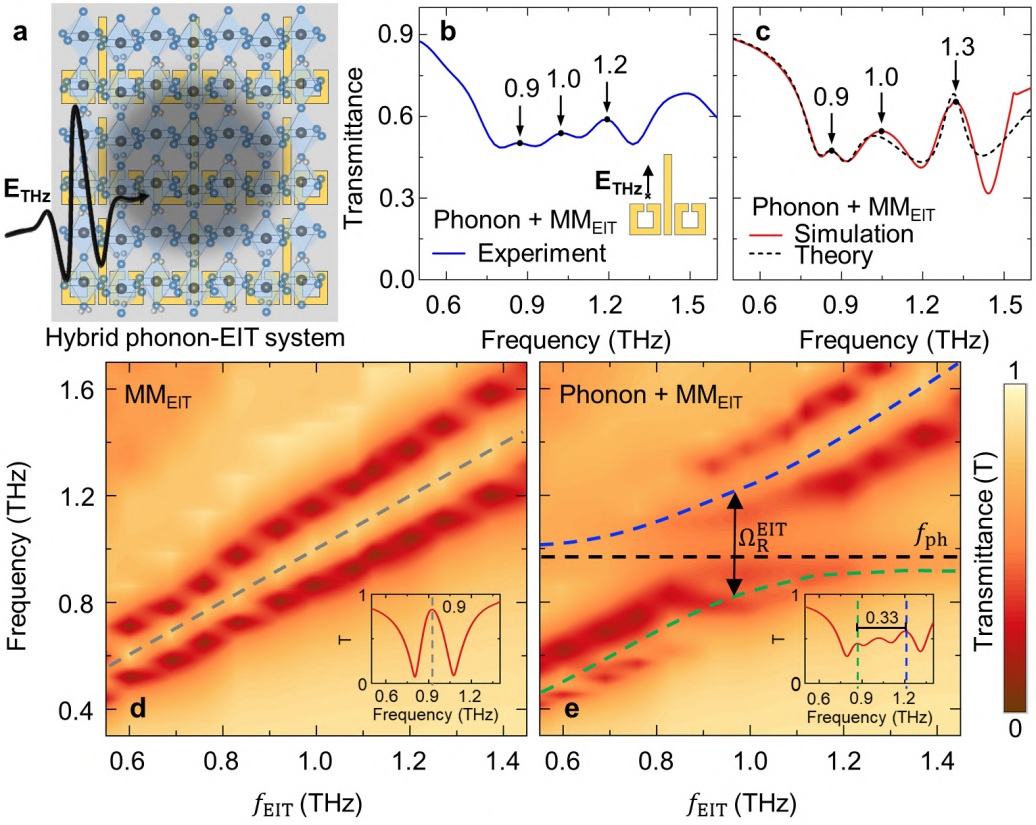

Figure 5.5: **(a)** Schematic of the hybrid phonon-EIT metamaterial. **(b)** Measured and **(c)** simulated (red) and theoretical (black-dashed) transmittance of the hybrid structure. Peaks at 0.9 THz, 1.0 THz, and 1.2 THz arise from phonon-induced splitting of the EIT response. 2D transmittance contour plots with the phonon **(d)** deactivated and **(e)** activated. The gray-dashed line in (d) marks the bare EIT peak. The black-dashed line in (e) marks the phonon mode. Blue and green dashed curves guide the upper and lower polaritonic-EIT branches. Insets in (d,e) show transmittance slices at $f_{\mathrm{EIT}} = 0.9$ THz. Taken from Ref. [15].

parency window of the bare structure splits into two distinct transparency peaks, centered near 0.9 THz and 1.2 THz. A feature near 1.0 THz is also visible, but it does not correspond to an EIT-*like* state. It arises from the superposition of the Rabi-split modes rather than from destructive interference. The mechanism behind the dual transparency follows directly from the excitation sequence. Under *y*-polarized illumination, the rod is excited first, forming upper and lower rod-phonon polaritonic branches. These hybridized states then excite the SRR via near-field interaction. The strong field confinement in the SRR

gap drives additional coupling to the phonon, producing further hybridization. The overlapping polaritonic states from the two resonators organize as follows: the upper polariton of the rod overlaps with the upper polariton of the SRR to form the higher-frequency transparency window at 1.2 THz, while the lower branches combine to produce the lower-frequency window at 0.9 THz. In both cases, destructive interference suppresses the radiative losses and restores transmission, preserving the EIT-*like* character of each window. The two-dimensional transmittance contour plots confirm this picture. Without the phonon, tuning the structural parameters yields a single EIT branch, as shown in Figure 5.5d. With the phonon activated (Figure 5.5e), a clear avoided crossing appears and the original transparency peak splits into upper and lower polaritonic-EIT branches. The anticrossing gap confirms coherent hybridization between the EIT mode and the phonon excitation. Near $f_{\mathrm{EIT}} \approx 0.9$ THz, the effective splitting (0.33 THz) is slightly larger than that of the isolated subsystems, reflecting the enhanced interaction within the combined cavity environment.

5.4.2 Field Distribution Analysis

To verify that the dual transparency peaks in the hybrid regime retain the interference signature of EIT, we examine the normalized in-plane electric field distributions at each transmission peak and dip frequency. Figure 5.6a shows that for the bare EIT structure at 1.3 THz, the field is predominantly localized within the SRR gaps, and the rod dipole oscillation is deactivated. This is the expected signature of destructive bright-dark interference.

In the hybrid structure, the same field signature is recovered at both 0.9 THz and 1.3 THz, as shown in Figures 5.6b and 5.6d, respectively. In both cases, the electric field concentrates in the SRR gaps and the rod dipole is suppressed, confirming that these two transmission peaks arise from destructive interference and therefore carry genuine EIT-*like* character. Figure 5.6c shows that at 1.1 THz, the field distribution is different. There are no opposing fields in the SRR gaps. This confirms that the 1.1 THz feature does not arise from inter-

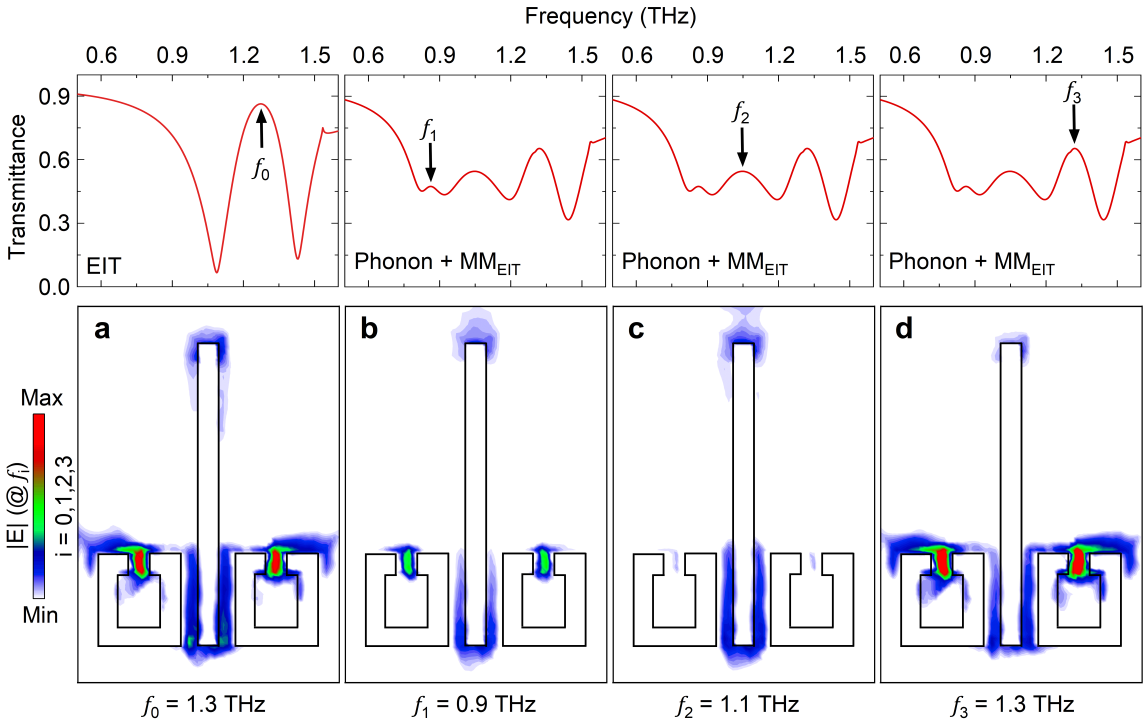

Figure 5.6: Normalized in-plane electric field distribution $|\mathbf{E}| = \sqrt{|E_x|^2 + |E_y|^2}$ for **(a)** the bare EIT structure at $f_0 = 1.3\,\text{THz}$, and the hybrid system at **(b)** $f_1 = 0.9\,\text{THz}$, **(c)** $f_2 = 1.1\,\text{THz}$, and **(d)** $f_3 = 1.3\,\text{THz}$. Normalization is with respect to the maximum field amplitude of the bare EIT structure at 1.3 THz. Taken from Ref. [15].

ference but from the overlap of polaritonic branches. The field analysis therefore provides direct spatial evidence distinguishing the two EIT-*like* windows from the intermediate polaritonic feature.

5.4.3 Group Delay and Slow-Light Analysis

A defining characteristic of EIT-*like* responses is the steep normal dispersion near the transparency window, which produces slow-light behavior. The group delay is extracted from the phase of the complex transmittance as

$$\tau_g = -\frac{1}{2\pi}\frac{d\varphi}{df}, \tag{5.3}$$

where φ is the transmission phase.

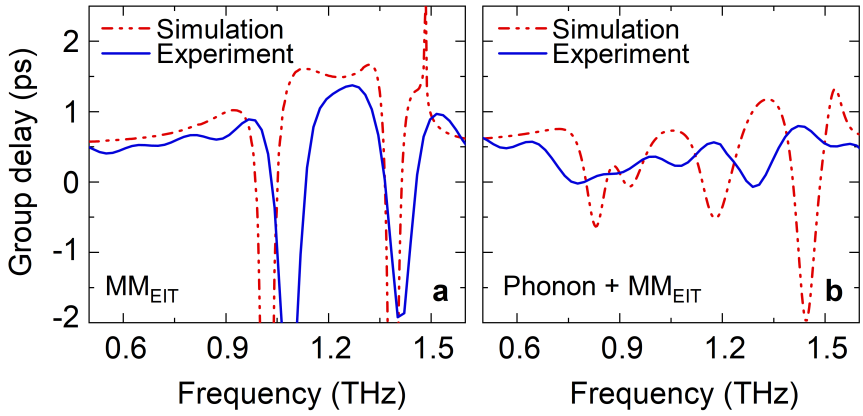

Figure 5.7: Simulated (red-dashed) and experimental (blue-solid) group delay for **(a)** the bare EIT structure and **(b)** the hybrid phonon-EIT system. A delay of approximately 1.5 ps is observed at the bare EIT peak. Introduction of the phonon mode produces additional delay features at 0.9 THz and 1.3 THz. Taken from Ref. [15].

For the bare EIT metamaterial, as shown in Figure 5.7a, a group delay of approximately 1.5 ps is observed near 1.3 THz, consistent with interference-induced dispersion. When the phonon mode is activated (Figure 5.7b), this single delay peak splits into multiple delay features at 0.9 THz and 1.3 THz, corresponding to the two transparency windows. Additional delay features appear at frequencies where none were present in the absence of the phonon. Negative group delay regions near the transmission dips signal anomalous dispersion, as expected at the edges of EIT-like windows. The slow-light behavior at the dual transparency peaks confirms that both windows carry the dispersive character associated with EIT. The reduced group velocity also increases the effective interaction time between the confined field and the phonon excitation, contributing to the slightly enhanced splitting observed in the hybrid system relative to the isolated subsystems.

5.4.4 Energy-Level Representation of the Hybrid Phonon-EIT System

To build physical intuition about the dual-transparency behavior, we interpret the hybrid system through an energy-level picture. Although EIT in metamaterials is a classical interference phenomenon, the three-level Λ analogy introduced in Chapter 2 provides a useful

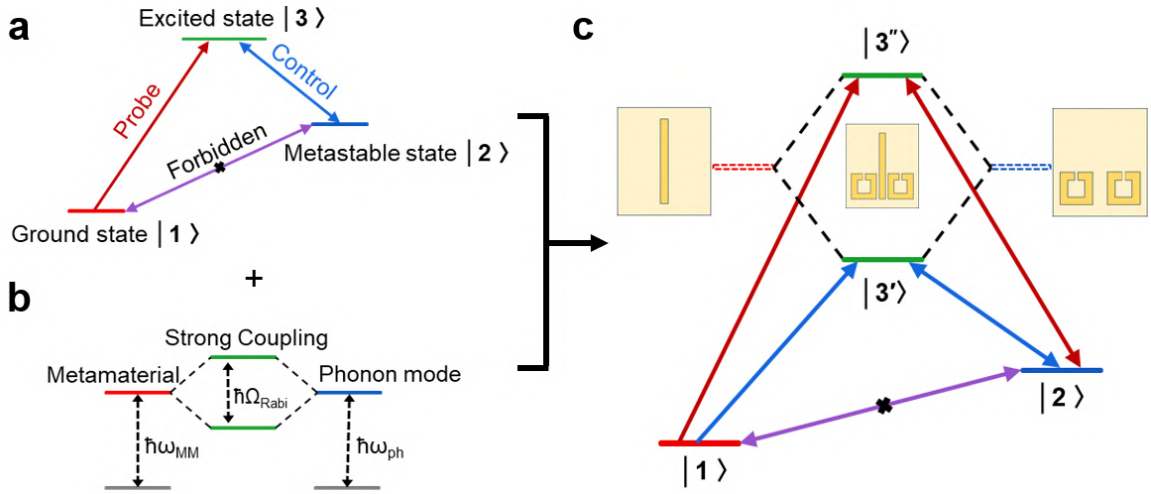

Figure 5.8: **(a)** Energy-level diagram for the three-level EIT system. The $|1\rangle \leftrightarrow |2\rangle$ transition is dipole forbidden. Transparency arises from destructive interference of excitation pathways for the $|1\rangle \rightarrow |3\rangle$ transition. **(b)** Energy-level diagram for Rabi splitting in a phonon-polariton system. **(c)** Combined energy-level diagram for the hybrid phonon-EIT system. Rod and SRR states are shown in red and blue. Rabi splitting creates polaritonic states $|3'\rangle$ (lower) and $|3''\rangle$ (upper), shown in green. The two distinct excitation pathways indicated by the red and blue arrows correspond to the two EIT-like transparency windows. Taken from Ref. [15].

conceptual framework.

In the atomic Λ system, a transparency window opens when the probe and control fields drive two excitation pathways that interfere destructively, suppressing the excited-state population, as shown in Figure 5.8a. In the metamaterial, the bright mode plays the role of the directly driven excited state, and the dark mode plays the role of the metastable state. When strong coupling to a phonon mode is introduced, the resonance undergoes Rabi splitting, yielding distinct upper and lower polariton branches, as depicted in Figure 5.8b. In the present hybrid system, both mechanisms must be incorporated simultaneously. The rod and SRR each independently undergo Rabi splitting with the phonon, producing four polaritonic states. Because the rod-phonon and SRR-phonon polaritonic branches overlap substantially in frequency, they can be condensed into two dominant levels: a lower polaritonic state $|3'\rangle$ and an upper polaritonic state $|3''\rangle$, as shown in Figure 5.8c. Each of these states now me-

diates a distinct bright-dark interference pathway. The lower polaritonic state $|3'\rangle$ enables destructive interference at the lower transparency frequency near 0.9 THz, while the upper polaritonic state $|3''\rangle$ enables interference at the higher transparency frequency near 1.2 THz. The two pathways are represented by the red and blue arrows in Figure 5.8c. The result is dual EIT-like transparency, with each window tied to one of the polaritonic branches. The separation between the two windows is governed by the Rabi splitting, which is determined by the oscillator strength of the phonon and the local field confinement of the resonators. Changing the coupling strength through geometric or material design therefore provides direct control over the spectral spacing of the two transparency windows.

5.4.5 Theoretical Modeling of the Hybrid Phonon-EIT System

The energy-level picture in the previous section motivates a quantitative framework. The system contains three interacting oscillators: the bright mode (rod), the dark mode (SRR), and the phonon. When the phonon is absent, the bright and dark modes interact through near-field coupling κ. When the phonon is present and the system enters the strong coupling regime, both the bright and dark modes hybridize with the phonon. Each mode splits into a lower and upper polariton branch. The original single bright-dark interference channel therefore bifurcates into two independent channels, one for each pair of polaritonic branches. The full transmittance of the hybrid system is then the superposition of two EIT-like contributions, one from the lower-polariton pair and one from the upper-polariton pair.

We begin with the single EIT system. The coupled oscillator equations for the bright mode amplitude x_b and dark mode amplitude x_d are

$$\ddot{x}_\mathrm{b} + \gamma_\mathrm{b}\dot{x}_\mathrm{b} + \omega_\mathrm{b}^2 x_\mathrm{b} + \kappa^2 x_\mathrm{d} = g_\mathrm{dr} E_0, \tag{5.4}$$

$$\ddot{x}_\mathrm{d} + \gamma_\mathrm{d}\dot{x}_\mathrm{d} + \omega_\mathrm{d}^2 x_\mathrm{d} + \kappa^2 x_\mathrm{b} = 0. \tag{5.5}$$

Here ω_b and ω_d are the resonance frequencies of the bright and dark modes, γ_b and γ_d are

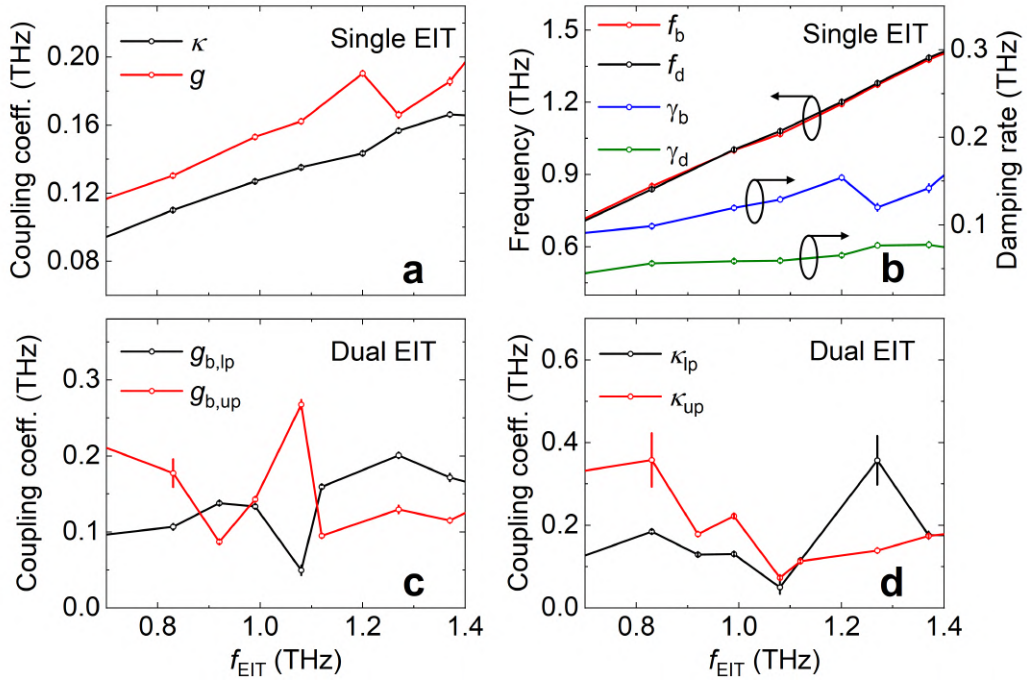

Figure 5.9: Extracted coupling parameters as a function of f_{EIT} for the **(a,b)** single EIT and **(c,d)** dual EIT systems. **(a)** κ (bright-dark coupling) and g_{dr} (bright-mode driving). **(b)** Resonance frequencies f_b, f_d and damping rates γ_b, γ_d. **(c)** Driving coefficients $g_{\mathrm{b,lp}}$ and $g_{\mathrm{b,up}}$ for the lower and upper polaritonic branches. **(d)** Coupling coefficients κ_{lp} and κ_{up} between the bright and dark polaritonic modes. Taken from Ref. [15].

their damping rates, g_{dr} is the driving efficiency of the bright mode (the coupling of the rod to the incident field, distinct from the strong coupling constant g in Chapter 2), and κ is the near-field coupling between the two resonators. The dark mode has no direct driving term because it cannot be excited by the incident field under the given polarization. Solving Eqs. (5.4) and (5.5) in the frequency domain gives the transmittance

$$T = 1 - \left| \frac{g_{\mathrm{dr}}(\omega - \omega_{\mathrm{d}} + i\gamma_{\mathrm{d}})}{(\omega - \omega_{\mathrm{b}} + i\gamma_{\mathrm{b}})(\omega - \omega_{\mathrm{d}} + i\gamma_{\mathrm{d}}) + \kappa^2} \right|^2 . \tag{5.6}$$

Fitting Eq. (5.6) to the simulated EIT spectra yields the parameters shown in Figures 5.9a and 5.9b. The extracted coupling satisfies $\kappa^2 > \gamma_{\mathrm{b}}\gamma_{\mathrm{d}}$, confirming robust bright-dark interaction.

When the phonon mode is activated, the eigenfrequencies of the lower and upper polari-

tonic branches are

$$\omega_{\mathrm{lp,up}} = \omega_0 \pm g_{\mathrm{rabi}}, \tag{5.7}$$

where ω_0 is the TO phonon frequency and $\Omega_{\mathrm{R}} = 2g_{\mathrm{rabi}}$ is the Rabi splitting. Both the bright and dark resonators undergo this splitting, replacing ω_{b} and ω_{d} by four hybridized frequencies $\omega_{\mathrm{b,lp}}$, $\omega_{\mathrm{b,up}}$, $\omega_{\mathrm{d,lp}}$, and $\omega_{\mathrm{d,up}}$, with corresponding damping rates and coupling coefficients $g_{\mathrm{b,lp}}$, $g_{\mathrm{b,up}}$, κ_{lp}, and κ_{up}. Each polaritonic branch forms its own bright-dark interference channel, and the total transmittance of the hybrid system is the superposition of the two EIT contributions,

$$\begin{aligned} T_{\mathrm{dEIT}} = 1 &- \left| \frac{g_{\mathrm{b,lp}}(\omega - \omega_{\mathrm{d,lp}} + i\gamma_{\mathrm{d,lp}})}{(\omega - \omega_{\mathrm{b,lp}} + i\gamma_{\mathrm{b,lp}})(\omega - \omega_{\mathrm{d,lp}} + i\gamma_{\mathrm{d,lp}}) + \kappa_{\mathrm{lp}}^2} \right|^2 \\ &- \left| \frac{g_{\mathrm{b,up}}(\omega - \omega_{\mathrm{d,up}} + i\gamma_{\mathrm{d,up}})}{(\omega - \omega_{\mathrm{b,up}} + i\gamma_{\mathrm{b,up}})(\omega - \omega_{\mathrm{d,up}} + i\gamma_{\mathrm{d,up}}) + \kappa_{\mathrm{up}}^2} \right|^2 . \end{aligned} \tag{5.8}$$

Eq. (5.8) provides an excellent fit to the simulated dual-transparency spectra, as shown in Figure 5.5c. The extracted parameters (Figures 5.9c,d) confirm that the hybrid system is governed by two distinct bright-dark coupling channels, each associated with one polaritonic branch.

5.4.6 Tunability of the EIT Response

The rod-SRR geometry is chosen in part because of the rotational and translational tunability it offers. These degrees of freedom allow controlled modulation of the interference mechanism and access to distinct resonant regimes without any change to the material or the device structure. When the incident field is polarized along the rod ($\theta = 0°$), the rod acts as the bright mode and the EIT transparency window is fully developed. As the structure is rotated, the projection of the incident field on the rod decreases while that on the SRR increases. At $\theta = 90°$, the rod is effectively decoupled from the incident field and the SRR LC resonance dominates the spectrum. The bright-dark hybridization that sustains EIT is

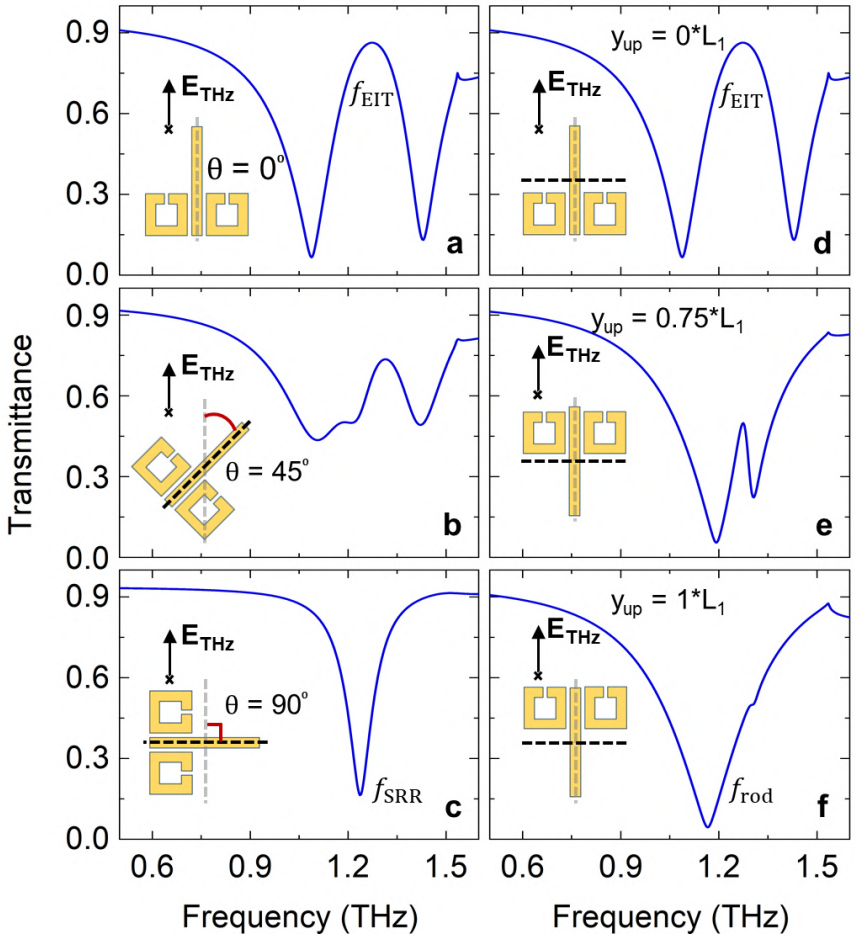

Figure 5.10: Simulated transmittance of the bare EIT metamaterial with **(a–c)** rotational tunability (angle θ) and **(d–f)** translational tunability (upward SRR displacement y_{up}). $L_1 = L - l$. Taken from Ref. [15].

lost, and the response transitions to a single LC-type resonance. This evolution is clearly visible in Figures 5.10a-c.

A complementary control is achieved by translating the SRR along the length of the rod. At the reference position $y_{\mathrm{up}} = 0$, the electric and magnetic excitation pathways for the SRR are in phase, so their contributions add constructively and the EIT condition is maintained. As the SRR is displaced upward, the electric pathway reverses its phase contribution. The two pathways now partially cancel each other, weakening the LC resonance and progressively collapsing the EIT window. At $y_{\mathrm{up}} = L_1$, the SRR resonance is effec-

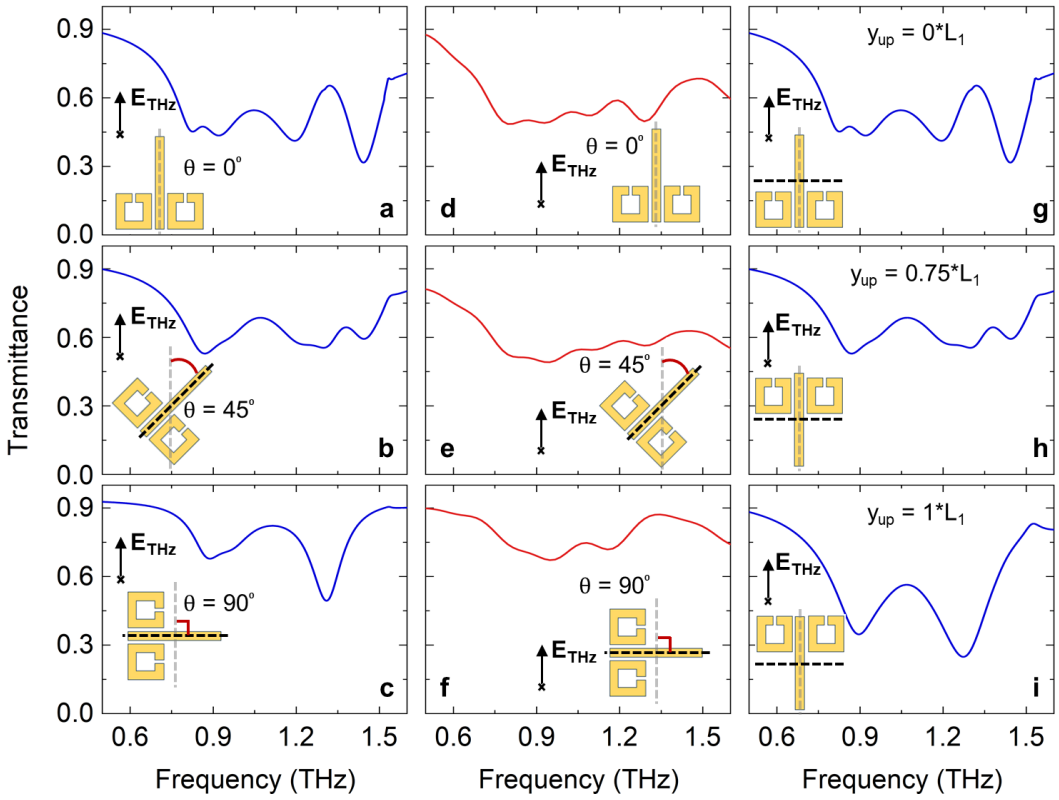

Figure 5.11: Simulated **(a–c)** and experimental **(d–f)** transmittance of the hybrid phonon-EIT structure with rotational tunability ($\theta = 0°, 45°, 90°$). Simulated spectra with translational tunability **(g–i)** for SRR displacement y_{up}. $L_1 = L - l$. Taken from Ref. [15].

tively deactivated and the spectrum reduces to the dipolar response of the rod alone. This is shown in Figures 5.10d-f. Both tuning mechanisms demonstrate that the EIT response is governed by controllable interference pathways. This structural control is essential in the hybrid system, where precise alignment of the EIT cavity resonance with the phonon mode determines the quality of the strong coupling and the dual-transparency response.

5.4.7 Tunability of the Hybrid Phonon-EIT Response

Building on the tunability of the bare EIT system, we now examine how rotation and translation modify the hybrid phonon-EIT response. These control parameters allow reversible switching between the dual-EIT regime and conventional phonon-polariton Rabi splitting.

At $\theta = 0°$, the rod bright mode is strongly driven and the full hybrid dual-transparency response is observed, as shown in Figures 5.11a and 5.11d. As the rotation angle increases to $\theta = 45°$, the bright-dark coupling weakens and the dual-EIT character diminishes (Figures 5.11b and 5.11e). At $\theta = 90°$, the rod is deactivated and the SRR becomes the dominant resonator. The dual-EIT response disappears, replaced by a conventional SRR-phonon Rabi splitting (Figures 5.11c and 5.11f). Rotational tuning therefore provides a continuous, reversible pathway from the three-oscillator hybrid system (rod-SRR phonon) to a two-oscillator strong-coupling system (SRR-phonon), with no structural modification.

Translational tuning achieves a complementary transition. At small values of y_{up}, the dual-EIT behavior is preserved. As y_{up} increases, the dark-mode participation diminishes and the dual-transparency response collapses. At $y_{\mathrm{up}} = L_1$, the SRR is effectively deactivated and the system reduces to the strongly coupled rod-phonon configuration, exhibiting conventional Rabi splitting of the rod alone (Figure 5.11i). Rotation and translation are therefore complementary: rotation accesses the SRR-phonon limit, while translation accesses the rod-phonon limit. Together they demonstrate the full range of spectral behaviors accessible within this single device platform.

5.4.8 Effect of Substrate and Phonon Linewidth

The choice of substrate plays a critical role in determining the electromagnetic response of the metamaterial, as it directly influences both the structural configuration and the resonance characteristics. Since different substrates possess distinct refractive indices, the metamaterial design must be optimized accordingly from the outset. While similar resonance features can be recovered through careful design adjustments, the coupling behavior remains sensitive to the dielectric environment.

To examine this dependence, we performed simulations using silicon and polyimide substrates, with appropriate modifications to the metamaterial geometry, while quartz was

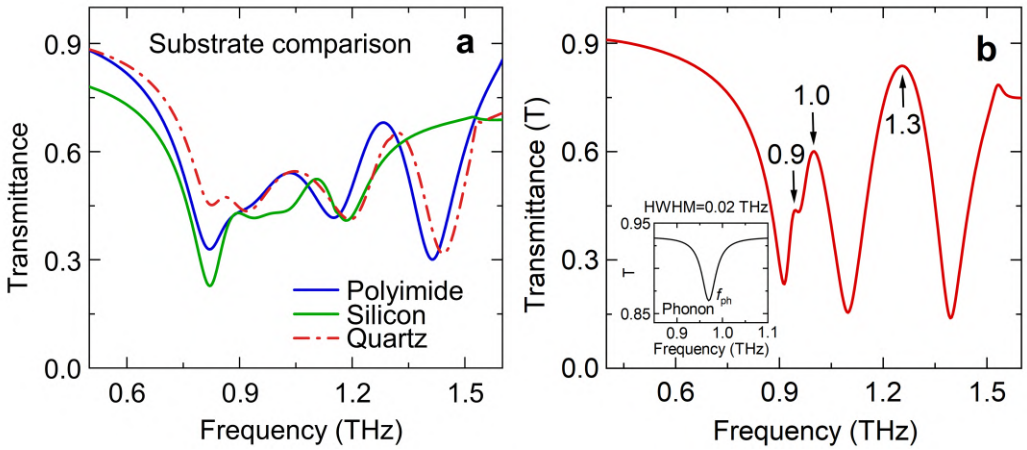

Figure 5.12: **(a)** Simulated transmittance of the hybrid structure on quartz (red dash-dot), polyimide (blue solid), and silicon (green solid) substrates. **(b)** Simulated transmittance of the phonon-EIT hybrid with a sharper phonon mode. The inset shows the phonon feature at 0.97 THz. The higher-frequency transparency peak shows substantially enhanced transmittance. Taken from Ref. [15].

used as the reference substrate for comparison. The simulated transmission spectra, shown in Figure 5.12a, indicate that the dual EIT-*like* peaks are preserved across all substrates. However, in the case of silicon, the reduced Rabi splitting leads to a smaller frequency separation between the two peaks, along with a decrease in transmission amplitude and a narrowing of the transparency window. In contrast, polyimide exhibits comparatively improved transmission characteristics, highlighting the role of substrate permittivity in modulating the coupling strength.

Another limitation of the demonstrated hybrid structure is the relatively low amplitude of the transmission maxima. This can be addressed by employing a material with a sharper phonon resonance. A reduced phonon linewidth enhances the individual transmission dips associated with Rabi splitting, which in turn leads to an increase in the amplitude of the EIT-*like* peaks. To illustrate this effect, we simulated a hypothetical phonon mode with a significantly smaller half-width at half maximum (HWHM = 0.02 THz), as shown in the inset of Figure 5.12b. The resulting transmission spectrum exhibits a pronounced enhancement,

with the higher-frequency EIT-*like* peak around 1.3 THz reaching amplitudes comparable to the original resonance. Furthermore, lowering the temperature is expected to further reduce phonon damping, thereby sharpening the resonance and improving the overall spectral response. Materials with intrinsically strong and sharp phonon modes, such as PbTe [133], provide promising platforms for accessing stronger light-matter interaction regimes, including ultra-strong and deep-strong coupling, which may lead to additional spectral splitting in the hybrid system.

5.5 Conclusion

In this chapter, we demonstrated a hybrid THz metamaterial platform in which the TO phonon of $MAPbI_3$ strongly couples to an EIT-*like* cavity, resulting in phonon-polariton mediated dual transparency. The original single EIT window splits into two distinct transparency peaks associated with the lower and upper polaritonic-EIT branches. This confirms coherent interplay between bright-dark interference and strong light-matter coupling. The strong coupling regime was validated through coupled oscillator modeling, spectral fitting, and comparison with the dissipative threshold. Field distribution analysis confirmed that both transparency peaks retain the interference signature of EIT. Phase-resolved THz-TDS measurements revealed enhanced dispersion and slow-light behavior at both windows. Rotational and translational tuning enables reversible switching between the dual-EIT response and conventional rod-phonon or SRR-phonon Rabi splitting, highlighting the multifunctional and reconfigurable nature of the hybrid platform.

While the spectral signatures of strong coupling and dual transparency are well established by the results in this chapter, several important dynamical aspects of the EIT response remain unaddressed. The frequency-domain analysis does not provide direct information about how long the induced current in the bright mode persists after excitation in the bare

EIT metamaterial. It also cannot resolve the coherence lifetime between the bright and dark modes, or identify the dephasing mechanisms that limit it. These timescales govern the depth and width of the EIT window and are central to any device application based on slow light or coherent switching. Measuring them requires a different approach entirely, one that drives the metamaterial into the nonlinear regime and reads the dynamics from the resulting time-resolved nonlinear signals. This is the subject of the following chapter.

Chapter 6

Unveiling Nonlinearities of Electromagnetically Induced Transparency in a THz Metamaterial

6.1 Introduction

The preceding chapter established that the EIT metamaterial can be driven into a dual-transparency regime through phonon-polariton hybridization. The spectral evidence for this is compelling: the single transparency window splits into two, the field distributions confirm EIT-*like* interference at both windows, and the coupled oscillator model reproduces the transmittance quantitatively. However, that chapter does not capture the ultrafast dynamics that evolve within the bare EIT transparency window, particularly on picosecond timescales, which are investigated in this work using 2D-THz spectroscopy.

Frequency-domain measurements are time-averaged. They reveal the spectral position and width of the EIT window but carry no information about how long the coherence between the bright and dark modes actually persists [65–67]. They cannot distinguish whether the energy stored in the bright mode decays before or after that coherence is lost. They cannot separate the contribution of structural inhomogeneity from that of intrinsic lifetime broadening to the observed linewidth of the EIT peak. Each of these questions has direct consequences for device performance. The group delay, the modulation depth, and the switching speed of any EIT-based device are all bounded by the answers. The standard approach for accessing dynamics in THz metamaterial systems is OPTP spectroscopy. This

technique cannot isolate the metamaterial contribution cleanly. The optical pump predominantly excites free carriers within the substrate or any integrated photoactive layer [24–26]. The resulting transient THz signal is therefore a convolution of substrate dynamics and resonator dynamics rather than a pure measurement of the coupled resonator system. A technique that drives the metamaterial with THz fields alone, below the substrate bandgap, is needed.

2D-THz spectroscopy was developed precisely to address this class of problems. The technique correlates two independent time axes, one corresponding to the real time and the other to the delay between two phase-locked excitation pulses. This correlation maps the nonlinear response of the system onto a two-dimensional frequency plane where different interaction signals appear at well-separated coordinates [95, 115]. First demonstrated in the context of semiconductor quantum wells [116, 117], 2D-THz spectroscopy has since been extended to quantum cascade structures [118], magnons [119, 120], superconductors [121, 122], and a variety of quantum materials [95, 123, 124]. It is today recognized as the THz analogue of two-dimensional infrared and optical coherent spectroscopies. Its defining capability is the simultaneous extraction of population relaxation times from pump-probe signals and coherence lifetimes from photon-echo signals, all from the same sample under the same excitation conditions. Critically, because THz photon energies lie far below the bandgap of common substrates such as quartz and silicon, the THz pulses drive the metallic resonators without generating any free carriers in the substrate. The measured nonlinear signals therefore originate entirely from the metamaterial resonators, free from any substrate contribution.

In this chapter, 2D-THz spectroscopy is applied to the bare EIT metamaterial for the first time. The bright-mode relaxation time, the coherence lifetime, and the pure dephasing contribution are extracted from the pump-probe and photon-echo signals. A density matrix model based on the three-level Λ-type system and Lindblad dissipation reproduces

all observed features. The dressed-state structure responsible for the EIT window is visualized directly through the multi-peak structure of the ABB photon-echo signal in the 2D frequency domain.

6.2 Linear THz Characterization

The metamaterial used in this study is the same rod-SRR structure described in Chapter 5. Its simulated electric field distribution and linear THz-TDS characterization are shown in Appendix Figures A.2 and A.3, respectively. The fabrication procedure, geometric parameters, and the coupled oscillator model for the linear EIT response are all discussed there and are not repeated here. The EIT peak frequency for the sample used in this experiment is $f_{\mathrm{EIT}} = 1.27\,\mathrm{THz}$, and the linear transmittance spectrum measured by THz-TDS is shown in Figure 6.1b.

Figure 6.1a summarizes the experimental geometry and the theoretical framework used throughout this chapter. The left panel shows the 2D-THz configuration. Two co-propagating, phase-locked THz pulses $\mathbf{E}_{\mathrm{A}}^{\mathrm{in}}(t,\tau)$ and $\mathbf{E}_{\mathrm{B}}^{\mathrm{in}}(t)$ illuminate the EIT metamaterial. The variable t is the real time, and τ is the delay between the arrival of the two pulses at the sample. When both pulses interact with the metamaterial near $\tau = 0$, a nonlinear signal $\mathbf{E}_{\mathrm{NL}}(t,\tau)$ is emitted and recorded. A detailed description and schematic of the 2D-THz spectroscopy experimental setup are presented in Chapter 3. In Figure 6.1a, the right panel shows the three-level Λ-type analogy adopted to model the EIT response. The ground state $|0\rangle$ represents the unexcited metamaterial. The state $|1\rangle$ is the bright dipole mode of the rod, which couples directly to the incident THz field. The state $|2\rangle$ is the dark LC mode of the SRR pair, which is shielded from direct excitation by structural symmetry but is driven indirectly through the near-field of the rod. The two allowed transitions, $|0\rangle$-$|1\rangle$ and $|1\rangle$-$|2\rangle$, create two distinct excitation pathways that accumulate a relative phase difference

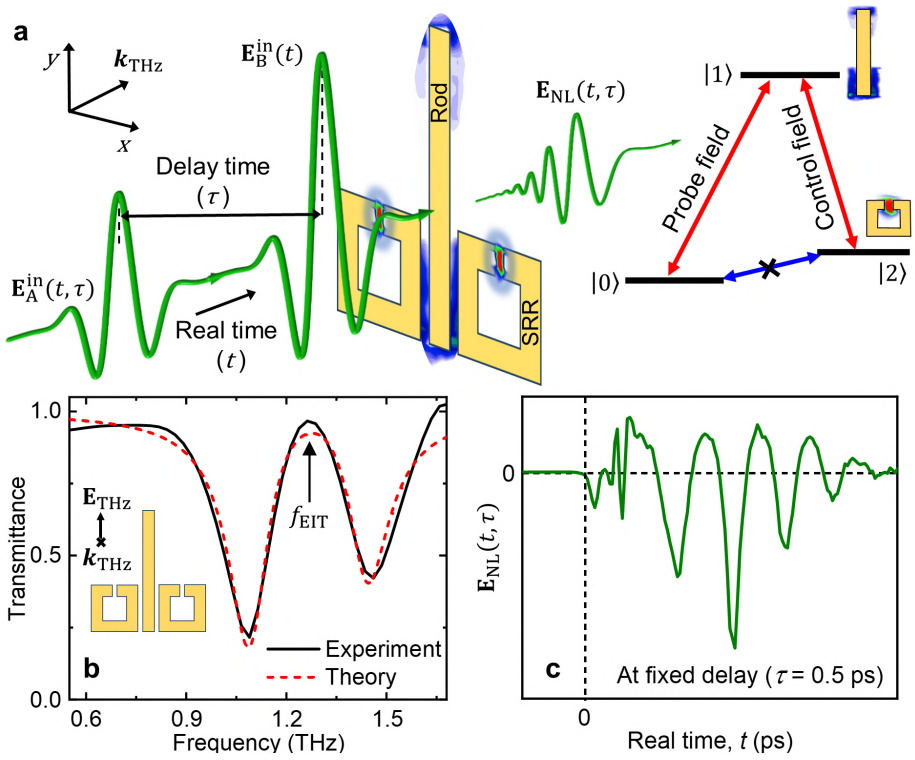

Figure 6.1: **(a) Left:** Schematic of the experimental geometry showing the two THz pulses $\mathbf{E}_{\mathrm{A}}^{\mathrm{in}}(t,\tau)$ and $\mathbf{E}_{\mathrm{B}}^{\mathrm{in}}(t)$ interacting with the EIT metamaterial, and the emitted nonlinear signal $\mathbf{E}_{\mathrm{NL}}(t,\tau)$. **Right:** Three-level Λ-type system used to model the EIT dynamics, with states $|0\rangle$, $|1\rangle$ (bright/rod), and $|2\rangle$ (dark/SRR). **(b)** Measured (black) and modeled (red-dashed) transmittance showing the EIT peak at $f_{\mathrm{EIT}} = 1.27\,\mathrm{THz}$. **(c)** A typical temporal scan of $\mathbf{E}_{\mathrm{NL}}(t,\tau)$ at a delay time of 0.5 ps showing coherent oscillations at the EIT resonance frequency. Taken from Ref. [28].

of π, satisfying the destructive interference condition that opens the EIT window.

Figure 6.1b shows the linear transmittance of this sample. The measured spectrum (black-solid) shows a well-defined transparency peak at 1.27 THz within the broad absorption dip of the rod dipole resonance. The theoretical curve (red-dashed), obtained from the coupled oscillator model, reproduces the measured lineshape with excellent agreement, confirming that the EIT parameters are accurately known before the nonlinear experiment begins. Figure 6.1c provides an exemplary temporal scan of $\mathbf{E}_{\mathrm{NL}}$ at $\tau = 0.5$ ps showing clear coherent oscillations. The oscillation frequency is 1.27 THz, precisely at the EIT peak. This

demonstrates that the nonlinear signal traces the EIT resonance of the metamaterial rather than any other feature of the substrate or the driving pulses.

In the three-level Λ-type analogy used throughout this chapter, the transition $|0\rangle \leftrightarrow |1\rangle$ is driven directly by the THz field. The transition $|1\rangle \leftrightarrow |2\rangle$ is mediated by the structural near-field coupling parameterized by g_s. The two excitation pathways accumulate a relative phase difference of π, satisfying the destructive interference condition that opens the EIT window.

6.3 Coupled Oscillator Model and Control-Field Dependence

The coupled oscillator framework for this system is developed in Chapter 2 and applied to the experimental results in Chapter 5. The key equations are reproduced here because they are referenced directly in the analysis below. The equations of motion for the bright-mode amplitude x_b and dark-mode amplitude x_d are

$$\ddot{x}_\mathrm{b} + \gamma_\mathrm{b}\dot{x}_\mathrm{b} + \omega_\mathrm{b}^2 x_\mathrm{b} + \kappa^2 x_\mathrm{d} = g_\mathrm{dr} E_0, \tag{6.1}$$

$$\ddot{x}_\mathrm{d} + \gamma_\mathrm{d}\dot{x}_\mathrm{d} + \omega_\mathrm{d}^2 x_\mathrm{d} + \kappa^2 x_\mathrm{b} = 0, \tag{6.2}$$

where ω_b and ω_d are the resonance frequencies, γ_b and γ_d are the respective linewidths, g_dr is the driving efficiency of the bright mode (not to be confused with the strong coupling constant g of Chapter 2), and κ is the near-field coupling coefficient between the two resonators. The resulting transmittance is

$$T = 1 - \left| \frac{g_\mathrm{dr}(\omega - \omega_\mathrm{d} + i\gamma_\mathrm{d})}{(\omega - \omega_\mathrm{b} + i\gamma_\mathrm{b})(\omega - \omega_\mathrm{d} + i\gamma_\mathrm{d}) + \kappa^2} \right|^2. \tag{6.3}$$

It is worth noting that the coupled oscillator framework adopted here is phenomenological in nature. The finite conductivity of the metallic resonators and the dielectric response of the quartz substrate are not included as explicit microscopic parameters. Instead, their

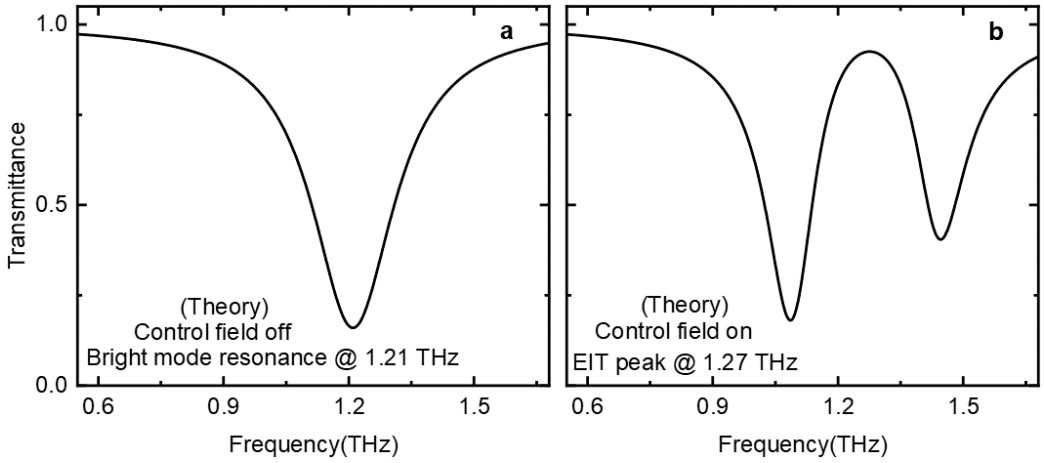

Figure 6.2: Theoretical transmittance of the EIT metamaterial **(a)** without the coupling field ($\kappa = 0$), showing only the rod dipole dip at 1.21 THz, and **(b)** with the coupling field active ($\kappa \neq 0$), showing the EIT transparency peak at 1.27 THz in agreement with experiment. Taken from Ref. [28].

effects are incorporated into the effective resonance frequencies ω_{b}, ω_{d} and the damping constants $\gamma_{\mathrm{b}}, \gamma_{\mathrm{d}}$. The resonance frequencies capture the combined influence of the resonator geometry and the surrounding dielectric environment, while the damping constants account for ohmic losses, radiative re-emission, and substrate absorption. These parameters are extracted by fitting Eq. (6.3) to both the CST-simulated and the experimentally measured transmittance spectra. The parameter set obtained from this procedure is subsequently used as the starting point for the QME (Quantum Master Equation) simulation of the nonlinear response discussed in Section 6.5.

Figure 6.2 demonstrates the role of the coupling field in generating the EIT window. In Figure 6.2a, the SRR is decoupled from the rod by setting $\kappa = 0$. Without any back-action from the dark mode, the transmittance is a single Lorentzian dip at 1.21 THz, the bare absorption of the rod dipole. The medium is fully opaque at this frequency. In Figure 6.2b, the coupling is restored ($\kappa \neq 0$). The near-field of the rod now drives the SRR indirectly, and the SRR back-action on the rod introduces the second excitation pathway. Destructive interference between the two pathways opens the EIT transparency window at 1.27 THz.

The agreement between Figure 6.2b and the measured spectrum of Figure 6.1b confirms that the coupled oscillator model accurately captures the linear response of the system. The EIT window owes its existence entirely to κ, and the transparency immediately vanishes when the coupling is removed. With this linear picture established and validated, the chapter now turns to what the nonlinear response reveals about the dynamics operating within that window.

Before proceeding to the nonlinear measurement, it is useful to establish the correspondence between the Conventional Coupled Oscillator (CCO) and QME parameters. The structural coupling coefficient κ in the CCO model and the hybridization parameter g_s in the QME both describe the coherent energy exchange between the bright and dark modes, governing the hybridized mode splitting and the formation of the EIT window. The damping constants γ_b and γ_d in the CCO model map onto the population decay rates γ_1 and γ_2 in the QME, which enter the Lindblad superoperator as relaxation channels for the bright and dark states respectively. One distinction is that the QME additionally includes a pure dephasing rate γ_φ, which decays the off-diagonal coherences without any population transfer and has no direct counterpart in the classical picture. Its origin here is the distribution of resonance frequencies across the array introduced by lithographic imperfections. Despite this difference, both frameworks reproduce the same EIT resonance positions and linewidths in the linear regime, confirming their mutual consistency. The parameter values extracted from the CCO fit to the measured transmittance therefore serve as reliable starting points for the QME simulation of the nonlinear response in Section 6.5.

6.4 2D-THz Spectroscopy: Nonlinear Signals and Frequency Analysis

6.4.1 The Nonlinear Signal and the Subtraction Scheme

The 2D-THz experiment generates two co-propagating, phase-locked THz pulses, denoted $\mathbf{E}_{\mathrm{A}}(t,\tau)$ and $\mathbf{E}_{\mathrm{B}}(t)$, separated by a controllable delay τ. For delay times $\tau < 0$, when pulse A arrives well before pulse B, each pulse independently excites the EIT metamaterial and the system responds linearly to each. When both pulses are present simultaneously near $\tau = 0$, the total field drives the system into the nonlinear regime. Nonlinear currents are induced that depend on both fields at once. Moreover, the nonlinear signal $\mathbf{E}_{\mathrm{NL}}(t,\tau)$ is isolated by the three-measurement subtraction scheme. At each delay value τ, three waveforms are recorded: $\mathbf{E}_{\mathrm{A}}(t,\tau)$ with pulse A alone, $\mathbf{E}_{\mathrm{B}}(t)$ with pulse B alone, and $\mathbf{E}_{\mathrm{AB}}(t,\tau)$ with both pulses simultaneously. The nonlinear signal is constructed as

$$\mathbf{E}_{\mathrm{NL}}(t,\tau) = \mathbf{E}_{\mathrm{AB}}(t,\tau) - \mathbf{E}_{\mathrm{A}}(t,\tau) - \mathbf{E}_{\mathrm{B}}(t). \tag{6.4}$$

This subtraction removes all linear contributions and retains only the $\chi^{(3)}$ terms that require the simultaneous presence of both pulses. The three individual field measurements that enter Eq. (6.4) are shown in Figure 6.3.

Figure 6.3a shows $\mathbf{E}_{\mathrm{A}}(t,\tau)$, the field transmitted through the sample with only pulse A present. The dominant feature is the transmitted pulse waveform itself, whose wavefront is marked by the green-dashed line. Following this wavefront along the real-time axis, a decaying oscillatory tail is visible. This tail is the free-induction decay (FID) of the EIT metamaterial: after the driving pulse has passed, the resonator system continues to ring at 1.27 THz and the FID amplitude decays as energy is lost through ohmic and radiative channels. As τ changes, this entire pattern shifts because pulse A arrives at a different absolute time relative to the detection window. The waveform is a purely linear response of

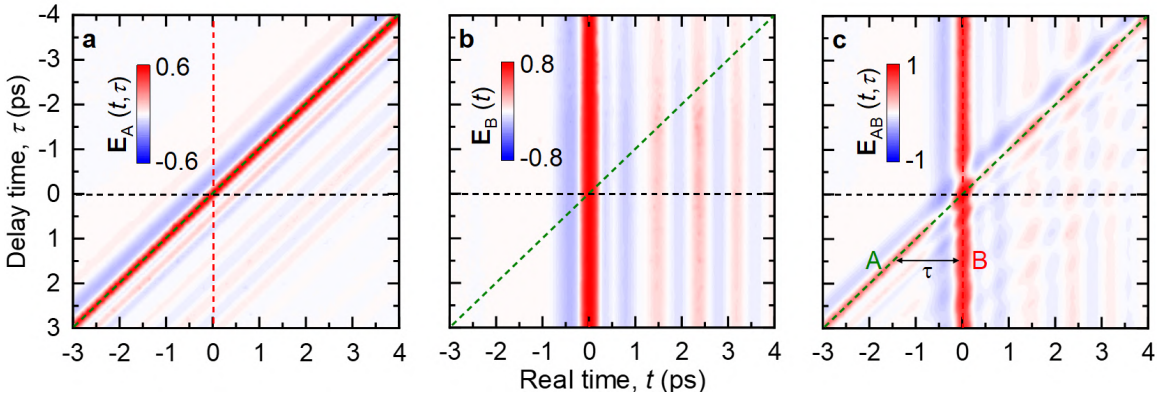

Figure 6.3: 2D contour plots of **(a)** $\mathbf{E}_{\mathrm{A}}(t,\tau)$ and **(b)** $\mathbf{E}_{\mathrm{B}}(t)$ transmitted individually. **(c)** $\mathbf{E}_{\mathrm{AB}}(t,\tau)$ with both pulses present. Fields normalized to $\mathbf{E}_{\mathrm{AB}}(0,0)$. Green and red dashed lines mark the propagation wavefronts of pulses A and B. Black dashed line indicates $\tau = 0$. Taken from Ref. [28].

the metamaterial to a single pulse. Figure 6.3b shows $\mathbf{E}_{\mathrm{B}}(t)$, the transmitted field with only pulse B present. Since pulse B always arrives at the same absolute time, this waveform is entirely independent of τ and appears as a horizontal band. It shows the same FID structure as Figure 6.3a but shifted to the pulse B wavefront position (red-dashed line).

Figure 6.3c shows $\mathbf{E}_{\mathrm{AB}}(t,\tau)$, the total transmitted field with both pulses present simultaneously. For large negative delays, where the two pulses are well separated in time, this waveform is simply the linear sum of Figures 6.3a and 6.3b. Near $\tau = 0$, however, additional features appear that are not present in either individual response. These features arise because the two pulses overlap on the sample and their combined field drives the coupled resonator system into the nonlinear regime. The subtraction of Eq. (6.4) removes the individual linear contributions and isolates these features as $\mathbf{E}_{\mathrm{NL}}$.

6.4.2 Identification of the Four $\chi^{(3)}$ Nonlinear Channels

The origin of each nonlinear signals can be understood from perturbation theory. In a third-order nonlinear interaction, the polarization involves three field interactions. When two pulses A and B are applied, the nonlinear polarization contains terms of the form $\mathbf{E}_{\mathrm{A}}\mathbf{E}_{\mathrm{A}}^{*}\mathbf{E}_{\mathrm{B}}$,

$\mathbf{E}_\mathrm{B}\mathbf{E}_\mathrm{B}^*\mathbf{E}_\mathrm{A}$, $\mathbf{E}_\mathrm{B}^2\mathbf{E}_\mathrm{A}^*$, and $\mathbf{E}_\mathrm{A}^2\mathbf{E}_\mathrm{B}^*$, where the asterisk denotes complex conjugation. Each combination produces a specific frequency along t and a specific frequency along τ, placing it at a unique position in the 2D spectrum.

The $\mathrm{A_{pu}}-\mathrm{B_{pr}}$ pump-probe signal arises from $\mathbf{E}_\mathrm{A}\mathbf{E}_\mathrm{A}^*\mathbf{E}_\mathrm{B}$, with frequency combination $\nu_\mathrm{AB} = \nu_\mathrm{A} - \nu_\mathrm{A} + \nu_\mathrm{B} \approx \nu_0$. The two interactions of pulse A cancel each other's phase. The signal carries no oscillation in τ and appears at $(\nu_0, 0)$. Its amplitude decays monotonically along τ, encoding T_1. The $\mathrm{B_{pu}}-\mathrm{A_{pr}}$ pump-probe signal arises from $\mathbf{E}_\mathrm{B}\mathbf{E}_\mathrm{B}^*\mathbf{E}_\mathrm{A}$, with frequency combination $\nu_\mathrm{BA} = \nu_\mathrm{B} - \nu_\mathrm{B} + \nu_\mathrm{A} \approx \nu_0$. The pump phase cancels, but the probe is pulse A, which oscillates at $\nu_\mathrm{A} \approx \nu_0$ along τ. This signal appears at $(\nu_0, -\nu_0)$ and its envelope also encodes T_1. The ABB photon echo arises from $\mathbf{E}_\mathrm{B}^2\mathbf{E}_\mathrm{A}^*$, with $\nu_\mathrm{ABB} = 2\nu_\mathrm{B} - \nu_\mathrm{A} \approx \nu_0$. The conjugation reverses the phase of pulse A rather than cancelling it. The signal retains the phases of both pulses, oscillates along τ at ν_0, and appears at (ν_0, ν_0). Its oscillatory decay encodes T_2. The BAA photon echo arises from $\mathbf{E}_\mathrm{A}^2\mathbf{E}_\mathrm{B}^*$, with $\nu_\mathrm{BAA} = 2\nu_\mathrm{A} - \nu_\mathrm{B} \approx \nu_0$. The phase of pulse B is reversed by conjugation. This signal appears at $(\nu_0, -2\nu_0)$ and also encodes T_2 independently. All four signals appear at the same detection frequency $\nu_t = \nu_0 = 1.27\,\mathrm{THz}$. They are separated entirely by their positions along the ν_τ axis.

6.5 Theoretical Model: Density Matrix Formalism

6.5.1 Three-Level Λ-Type Hamiltonian

The general density matrix framework and the three-level Λ-type Hamiltonian are introduced in Chapter 2. Here we specify the Hamiltonian for this system. The total Hamiltonian

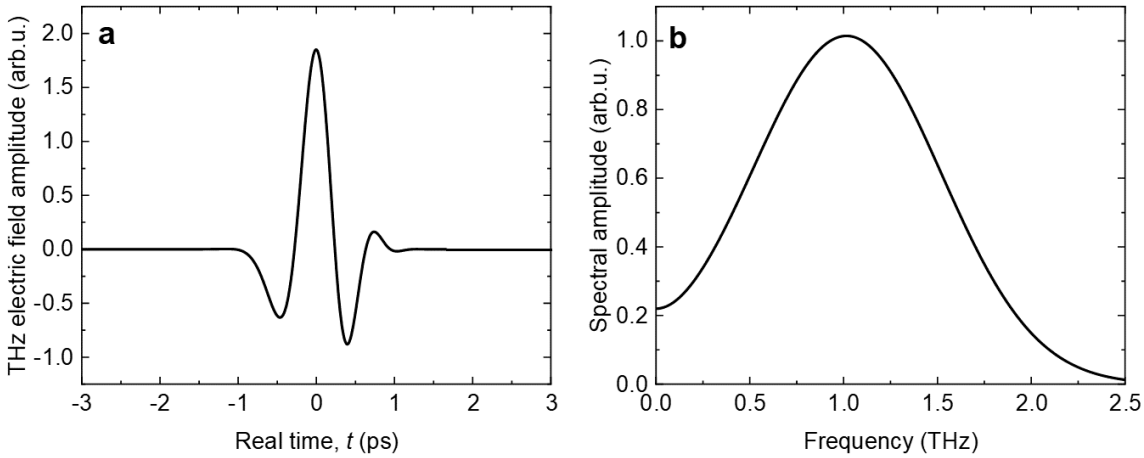

Figure 6.4: **(a)** Modelled time transient and **(b)** frequency spectrum of the input THz pulse used in the density matrix simulation. The spectrum peaks near 1.0 THz and covers the EIT resonance at 1.27 THz with adequate spectral weight. Taken from Ref. [28].

is $\hat{H}(t) = \hat{H}_0 + \hat{H}_c + \hat{H}_{int}(t)$, where

$$\hat{H}_0 = E_0 \left|0\right\rangle \left\langle 0\right| + E_1 \left|1\right\rangle \left\langle 1\right| + E_2 \left|2\right\rangle \left\langle 2\right|, \tag{6.5}$$

$$\hat{H}_c = g_s\left(\left|1\right\rangle \left\langle 2\right| + \left|2\right\rangle \left\langle 1\right|\right), \tag{6.6}$$

$$\hat{H}_{int}(t) = -\mu_{01} E(t)\left(\left|0\right\rangle \left\langle 1\right| + \left|1\right\rangle \left\langle 0\right|\right). \tag{6.7}$$

Here $\hat{H}_0$ carries the bare energies of the three states, $\hat{H}_c$ describes the structural near-field coupling between the bright and dark modes with coupling constant g_s, and $\hat{H}_{int}(t)$ is the THz field-dipole interaction. The RWA is applied to remove rapidly oscillating off-resonant terms. The THz excitation field is modelled as a chirped Gaussian pulse,

$$E(t) = E_0 \cos\left[2\pi f_0 \gamma \left(e^{(t-t_0)/\gamma} - 1\right)\right] \exp\left(-\frac{(t-t_0)^2}{2\sigma^2}\right), \tag{6.8}$$

where $f_0 = 1.0\,\text{THz}$ is the central frequency, $\sigma = 0.35\,\text{ps}$ is the Gaussian envelope width, and $\gamma = 1.6\,\text{ps}$ is the chirp parameter. These values are chosen to match the measured THz pulse waveform. The modelled pulse and its spectrum are shown in Figure 6.4.

Figure 6.4a shows the modelled time-domain waveform. Figure 6.4b shows the corresponding frequency spectrum. The peak near 1.0 THz and the finite spectral weight ex-

tending to 1.27 THz confirm that the modelled pulse has adequate coverage of the EIT resonance frequency. Without spectral weight at 1.27 THz, the model could not drive the EIT resonance and the theoretical 2D spectrum would not reproduce the experiment. The consistency between the modelled pulse spectrum and the experimental THz pulse spectrum is what makes the quantitative agreement in all subsequent figures possible.

6.5.2 Physical Picture of the 2D-THz Measurement

The nonlinear signals observed in 2D-THz spectroscopy originate from the coherent interaction of the sample with two time-delayed THz pulses. While the density matrix formalism provides a rigorous mathematical description of these processes, it is useful to first develop an intuitive understanding of how the different spectral features arise. Such a physical picture helps establish the connection between the measured nonlinear signals and the underlying coherent dynamics of the coupled metamaterial system.

When the first THz pulse interacts with the metamaterial, it excites a coherent superposition of the bright and dark resonator modes. During the time delay τ, this coherent state evolves freely and accumulates a phase determined by the resonance frequency of the coupled system. In an ideal system where every resonator is identical, all unit cells would evolve with the same phase. In practice, however, small variations in fabrication dimensions and local material properties introduce slight differences in the resonance frequencies of individual resonators. As a result, the collective coherence gradually dephases with increasing delay time.

The arrival of the second THz pulse modifies the evolution of the system by interacting with the remaining coherent polarization created by the first pulse. Under suitable conditions, this interaction reverses the accumulated phase differences and produces a rephasing process. The emitted photon echo therefore represents the recovery of the macroscopic coherence of the ensemble rather than the generation of a new excitation. As the delay

between the two excitation pulses increases, the photon echo gradually decreases because irreversible dephasing processes continuously reduce the remaining coherence within the coupled system. Consequently, the decay of the photon echo directly reflects the coherence lifetime T_2.

In contrast, the pump-probe signal originates from the population created after the first THz excitation. Since the population does not retain phase information, its temporal evolution is governed primarily by energy relaxation processes. The decay of this signal, therefore, provides direct access to the population relaxation time T_1. By analysing both the pump-probe and photon-echo signals, it is possible to separate population relaxation from coherence decay, thereby allowing the different contributions to the nonlinear response to be investigated independently.

The two-dimensional frequency spectrum provides additional insight into the physical processes occurring within the coupled metamaterial. The pump-probe peaks primarily reflect the population dynamics of the hybrid resonant states, whereas the rephasing peaks provide information about the system's coherence. Furthermore, the shape of the rephasing peak reflects the degree of structural disorder present in the metamaterial array. A symmetric peak indicates a nearly homogeneous ensemble, whereas an elongation along the diagonal direction is characteristic of inhomogeneous broadening arising from small variations in the resonance frequencies of individual resonators. The width of the peak along the anti-diagonal direction, on the other hand, is determined mainly by the intrinsic homogeneous linewidth of the coupled resonance.

The nonlinear response measured in this work, therefore, provides considerably more information than conventional linear THz spectroscopy. In addition to determining the resonance frequencies of the hybrid states, 2D-THz spectroscopy enables independent measurements of the population relaxation time, the coherence lifetime, and the effects of structural disorder on coherent dynamics. This separation of distinct physical processes forms the

basis of the quantitative analysis presented in the following sections, in which the density matrix formalism is employed to model the measured nonlinear spectra and extract the relevant relaxation parameters.

6.5.3 Lindblad Master Equation and Decoherence

The dissipative dynamics are governed by the Lindblad master equation introduced in Chapter 2. For this system it takes the form

$$\frac{d\hat{\rho}}{dt} = -\frac{i}{\hbar}\left[\hat{H}(t), \hat{\rho}\right] + \mathcal{L}(\hat{\rho}), \tag{6.9}$$

where the Lindblad superoperator is

$$\mathcal{L}(\hat{\rho}) = \sum_{\alpha} \gamma_{\alpha}\left[\hat{L}_{\alpha}\hat{\rho}\hat{L}_{\alpha}^{\dagger} - \tfrac{1}{2}\left\{\hat{L}_{\alpha}^{\dagger}\hat{L}_{\alpha}, \hat{\rho}\right\}\right] + \sum_{k} \gamma_{\varphi}\left[\hat{L}_{k}\hat{\rho}\hat{L}_{k}^{\dagger} - \tfrac{1}{2}\left\{\hat{L}_{k}^{\dagger}\hat{L}_{k}, \hat{\rho}\right\}\right]. \tag{6.10}$$

The first sum runs over population relaxation processes. The transitions $|1\rangle \rightarrow |0\rangle$ and $|1\rangle \rightarrow |2\rangle$ at rates γ_1 and γ_2 are implemented through transition operators $\hat{L}_{\alpha} = |l\rangle\langle k|$. These decays are the excited-state populations and damp coherences at half the population decay rate. The values of γ_1 and γ_2 are taken from the linear transmittance fit, ensuring consistency between the linear and nonlinear descriptions. The second sum accounts for pure dephasing through diagonal operators $\hat{L}_k = |k\rangle\langle k|$ at rate γ_{φ}. Pure dephasing attenuates only the off-diagonal elements of $\hat{\rho}$ without transferring population. In this metamaterial, its physical origin is structural inhomogeneity. The lithographic imperfections produce a distribution of resonant frequencies across the array, randomizing the phase of contributions from different unit cells without dissipating their energy.

The equation of motion is integrated numerically using a fourth-order Runge-Kutta algorithm, starting from $\hat{\rho}(0) = |0\rangle\langle 0|$. The macroscopic current response is computed as

$$j(t) = \frac{iN}{\hbar}\sum_{k,l} \rho_{kl}(t)\,(E_k - E_l)\,d_{kl}, \tag{6.11}$$

where d_{kl} are the dipole matrix elements and N is the number density of resonators. The nonlinear current $j_{\mathrm{NL}}(t,\tau) = j_{\mathrm{AB}}(t,\tau) - j_{\mathrm{A}}(t,\tau) - j_{\mathrm{B}}(t)$ is computed from three separate integrations. Two-dimensional Fourier transformation of $j_{\mathrm{NL}}(t,\tau)$ gives the theoretical 2D spectrum for direct comparison with experiment.

6.5.4 Origin of the Third-Order Nonlinearity

It is worth clarifying that the third-order nonlinearity in this model does not originate from any explicit nonlinear term in the Hamiltonian. Neither $\hat{H}_{\mathrm{c}}$ nor $\hat{H}_{\mathrm{int}}(t)$ carries a field-dependent or intensity-dependent contribution. The structural coupling $\hat{H}_{\mathrm{c}}$ is a field-independent hybridization term, and $\hat{H}_{\mathrm{int}}(t)$ enters the Hamiltonian linearly in the applied THz field. The nonlinear response emerges instead from the repeated action of the commutator $[\hat{H}(t),\hat{\rho}]$ in the Liouville–von Neumann equation across successive field interactions. This is a fundamental consequence of the density matrix formalism for a multilevel system. The trace constraint $\mathrm{Tr}(\hat{\rho}) = 1$ enforces a coupling between the diagonal population elements and the off-diagonal coherence elements of $\hat{\rho}$ that is intrinsically nonlinear in the driving field, physically analogous to population saturation in a two-level atom.

To third order in the applied field, the four-wave mixing signals arise from three successive applications of the commutator $[\hat{H}_{\mathrm{int}},\hat{\rho}]$. The first two field interactions drive the system into one of two intermediate states depending on the pulse ordering: either a population grating, which underlies the pump-probe signals, or a rephasing coherence, which underlies the photon-echo signals. The third field interaction then converts this intermediate state into a radiating off-diagonal coherence that emits the observed nonlinear current. Meanwhile, the structural coupling g_{s} plays an important but passive role in this sequence. During the free-evolution periods between successive field interactions, g_{s} mixes the bright and dark state populations and coherences, imprinting the dark-mode dynamics onto the

evolving density matrix. This mixing is what gives rise to the cross-peak structure and the oscillatory decay of the photon-echo signal in the 2D spectrum. However, g_s does not itself generate the nonlinearity. It governs only how the nonlinear signal evolves in the windows between THz-field interactions, shaping the spectral and temporal structure of the response rather than being its origin.

6.6 Experimental Results and Analysis

6.6.1 The Nonlinear Signal and its Two-Dimensional Spectrum

Figure 6.5a shows the experimentally measured nonlinear signal $\mathbf{E}_{\mathrm{NL}}(t,\tau)$ as a 2D contour plot. For large negative delays, where pulse A arrives at the sample long before pulse B, the nonlinear signal is negligibly small. This directly confirms that the three-measurement subtraction works correctly: when the two pulses do not interact, the subtraction returns zero and no nonlinear contribution remains. As τ approaches zero, a coherent signal emerges. Coherent oscillations at 1.27 THz appear along the real-time axis t, tracing the EIT resonance of the metamaterial. These oscillations confirm that the nonlinear response originates from the coupled resonator system rather than from any substrate contribution. The signal also varies along τ: this modulation reflects the mixing of the two THz field frequency components by the nonlinear interaction and encodes how the phase relationship between the two pulses affects the nonlinear output. The theoretical nonlinear current $j_{\mathrm{NL}}(t,\tau)$ reproduces the overall temporal structure of the experimental contour faithfully, including the onset near $\tau = 0$ and the modulation pattern along both t and τ, as shown in Figure 6.5c.

Figure 6.5b shows the 2D Fourier spectrum. Four distinct nonlinear signals are visible, all located at the detection frequency $\nu_t = \nu_0 = 1.27\,\mathrm{THz}$. Their positions along the excitation frequency axis are $\nu_\tau = 0$, $-\nu_0$, $+\nu_0$, and $-2\nu_0$, corresponding to the four $\chi^{(3)}$ signals. These signals are $\mathrm{A_{pu}}-\mathrm{B_{pr}}$, $\mathrm{B_{pu}}-\mathrm{A_{pr}}$, ABB photon echo, and BAA photon echo

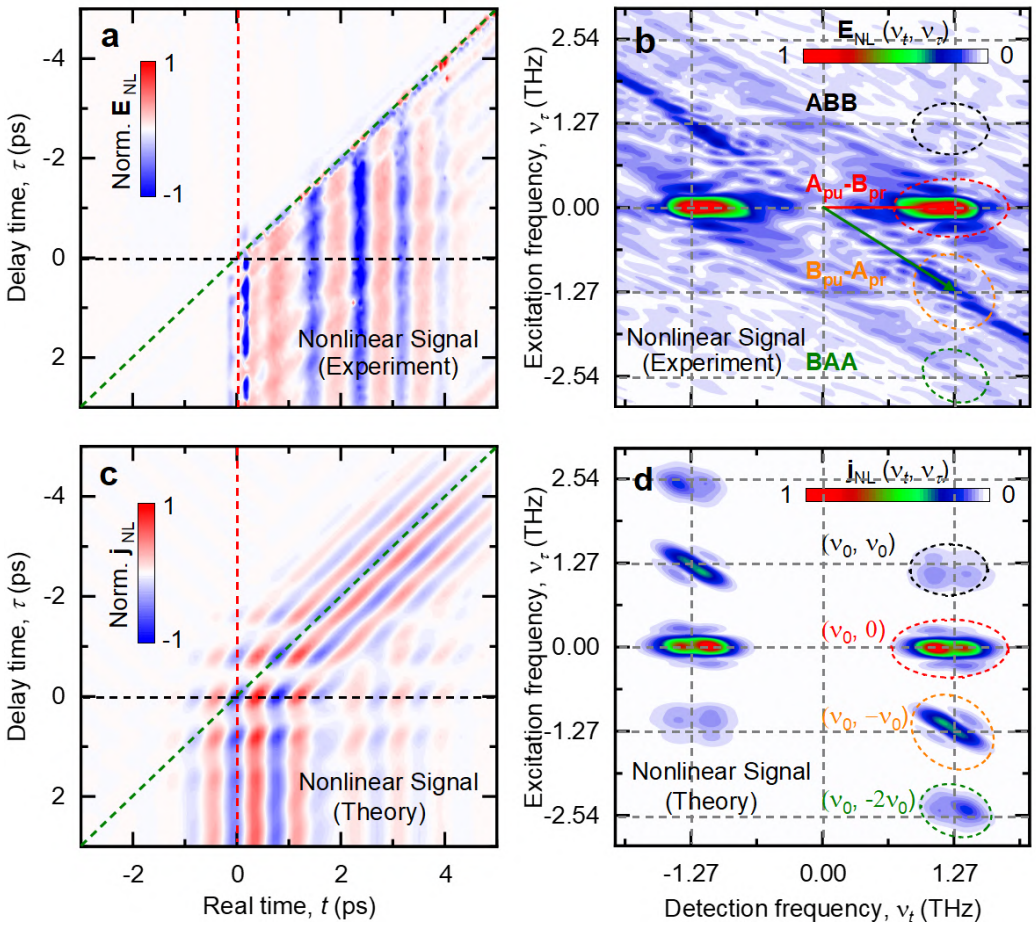

Figure 6.5: **(a)** 2D contour plot of $\mathbf{E}_{\mathrm{NL}}(t,\tau)$. Green and red dashed lines mark the wavefronts of pulses A and B. Black dashed line marks $\tau = 0$. **(b)** Normalized 2D Fourier spectrum $\mathbf{E}_{\mathrm{NL}}(\nu_t,\nu_\tau)$. Dashed ellipses indicate the four $\chi^{(3)}$ signal positions. Green and red arrows are the frequency vectors of pulses A and B. **(c)** Theoretical $j_{\mathrm{NL}}(t,\tau)$ and **(d)** its 2D Fourier spectrum, in excellent agreement with (a,b). Taken from Ref. [28].

respectively. The two pump-probe signals are substantially more intense than the two echo signals. This intensity hierarchy arises from the $\chi^{(3)}$ scaling: pump-probe signals involve two interactions with the pump and one with the probe, while echo signals carry reversed phase information and therefore scale differently with the pulse amplitudes. The green and red arrows in the Figure 6.5b mark the frequency vectors of pulses A and B, showing how each signal is formed by combinations of these vectors. The theoretical 2D spectrum (Figure 6.5d) agrees well with experiment in all four signal positions, their relative amplitudes,

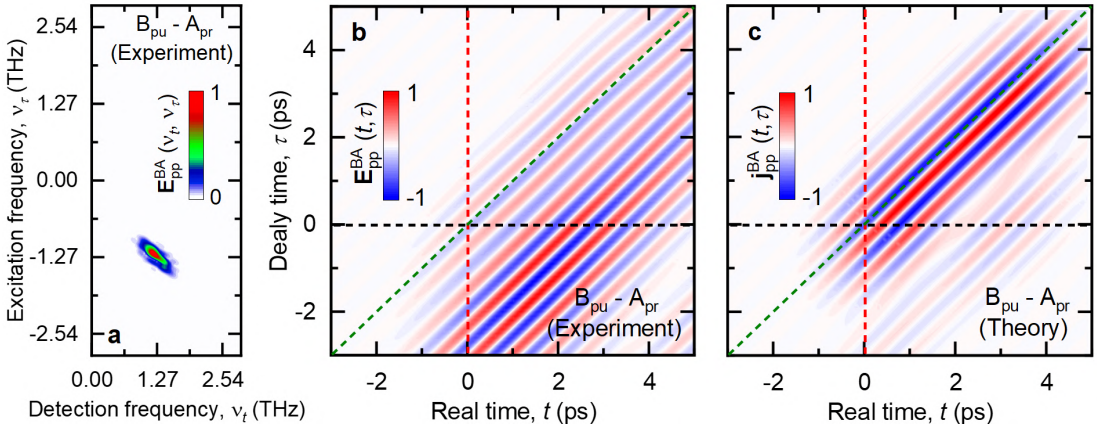

Figure 6.6: **(a)** 2D Gaussian filter region isolating the $\mathrm{B_{pu}}-\mathrm{A_{pr}}$ signal. **(b)** Experimental $\mathbf{E}^{\mathrm{BA}}_{\mathrm{pp}}(t,\tau)$ and **(c)** theoretical $j^{\mathrm{BA}}_{\mathrm{pp}}(t,\tau)$ 2D contour plots. Green and red dashed lines mark pulse A and B wavefronts. Black dashed line marks $\tau = 0$. Taken from Ref. [28].

and their spectral shapes. This agreement confirms that the three-level Λ-type Lindblad model captures the essential physics of the nonlinear response.

6.6.2 Bright-Mode Relaxation from the Pump-Probe Signal

The $\mathrm{A_{pu}}-\mathrm{B_{pr}}$ pump-probe signal at $(\nu_0, 0)$ is extracted by applying a 2D Gaussian filter in the frequency domain and inverse-Fourier transforming. The resulting time-domain contour of $\mathbf{E}^{\mathrm{AB}}_{\mathrm{pp}}(t,\tau)$ is shown in Figure 6.7a, with the theoretical counterpart in Figure 6.7b. Before discussing Figure 6.7 in detail, the complementary $\mathrm{B_{pu}}-\mathrm{A_{pr}}$ signal at $(\nu_0, -\nu_0)$ is shown in Figure 6.6. The filtering step that isolates this signal from the 2D spectrum is illustrated in Figure 6.6a, which shows the 2D Gaussian filter window applied around $(\nu_0, -\nu_0)$. The resulting experimental time-domain contour is shown in Figure 6.6b, and the theoretical counterpart in Figure 6.6c.

Figure 6.6a shows the Gaussian filter ellipse in the (ν_t, ν_τ) plane centred on the $\mathrm{B_{pu}}-\mathrm{A_{pr}}$ signal at $(\nu_0, -\nu_0)$. Only spectral weight within this window is retained before the inverse Fourier transform is applied, ensuring clean separation from the adjacent pump-probe signal at $(\nu_0, 0)$ and the echo signals. Figure 6.6b shows the resulting $\mathbf{E}^{\mathrm{BA}}_{\mathrm{pp}}(t,\tau)$ contour. This

signal oscillates along both t and τ. The oscillations along t reflect emission at 1.27 THz. The oscillations along τ arise because the probe in this channel is pulse A, which carries frequency $\nu_A \approx \nu_0$ in both time dimensions. The envelope of these τ-oscillations decays at a rate consistent with T_1. Figure 6.6c shows the theoretical counterpart, which reproduces both the oscillation pattern and the envelope decay. The fact that this symmetric measurement with reversed pulse ordering yields the same T_1 confirms that the population relaxation rate is an intrinsic property of the bright mode rather than a consequence of the specific pulse sequence used to probe it.

Returning to the $A_{pu}-B_{pr}$ signal in Figure 6.7a: this is the only nonlinear component in the 2D spectrum that decays monotonically along τ without any sinusoidal modulation. The pump interaction with pulse A cancels its spectral phase, leaving a contribution that depends only on the energy deposited by the pump rather than on its phase. Physically, pulse A excites the rod dipole out of equilibrium. Pulse B, delayed by τ, reads out the current amplitude remaining in the rod at that time. As τ increases, the rod current has had more time to relax, and the signal decreases monotonically. The theoretical contour in Figure 6.7b reproduces this behavior faithfully. At fixed real time $t = 1.2$ ps, the τ-trace is fitted by

$$E_{pp}(\tau) = A_1 \exp\left(-\tau/T_1\right), \tag{6.12}$$

giving the bright-mode relaxation time $T_1 = 1.96 \pm 0.11$ ps, as shown in Figure 6.7c.

6.6.3 Coherence Lifetime from the Photon-Echo Signal

Figure 6.7a and 6.7b show the $A_{pu}-B_{pr}$ contour for experiment and theory respectively. The signal is strictly non-oscillatory along τ: the amplitude simply decreases as the delay increases. This is the direct consequence of the phase cancellation described above. Figure 6.7c shows the τ-trace extracted at $t = 1.2$ ps. The single exponential fit is excellent over the full delay range measured, and the extracted value $T_1 = 1.96 \pm 0.11$ ps represents

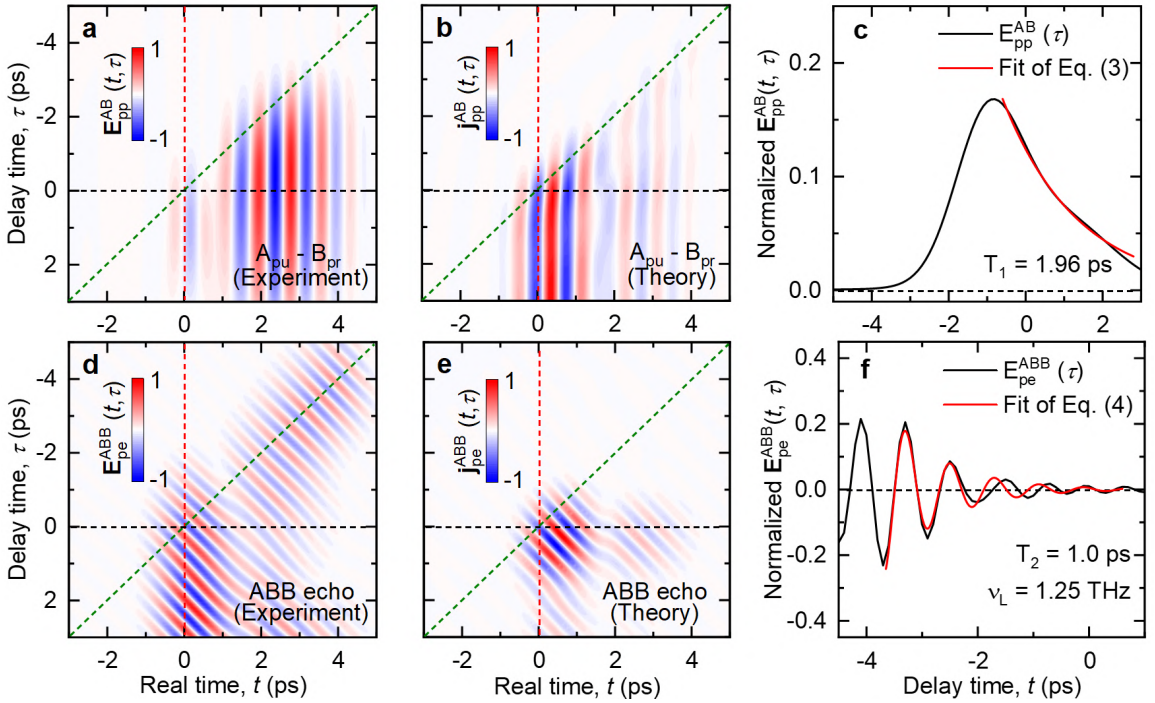

Figure 6.7: **(a)** Experimental $\mathbf{E}_{\mathrm{pp}}^{\mathrm{AB}}(t,\tau)$ and **(b)** theoretical $j_{\mathrm{pp}}^{\mathrm{AB}}(t,\tau)$ for the $\mathrm{A_{pu}}-\mathrm{B_{pr}}$ pump-probe signal. **(c)** Temporal trace at $t = 1.2\,\mathrm{ps}$ with single-exponential fit (red) giving $T_1 = 1.96 \pm 0.11\,\mathrm{ps}$. **(d)** Experimental $\mathbf{E}_{\mathrm{pe}}^{\mathrm{ABB}}(t,\tau)$ and **(e)** theoretical $j_{\mathrm{pe}}^{\mathrm{ABB}}(t,\tau)$ for the ABB photon-echo signal. **(f)** Temporal trace at $t = 4.5\,\mathrm{ps}$ with damped-sinusoid fit (red) giving $T_2 = 1.0 \pm 0.1\,\mathrm{ps}$. Taken from Ref. [28].

the characteristic timescale over which the radiative energy stored in the bright rod dipole dissipates through ohmic losses and radiative re-emission.

Figure 6.7d shows the ABB photon-echo contour. In contrast with the pump-probe signal in Figure 6.7a, the ABB echo oscillates along both t and τ. The oscillations along t reflect emission at the EIT resonance frequency 1.27 THz, consistent with all other signals. The oscillations along τ have a fundamentally different origin. In the $\mathbf{E}_{\mathrm{B}}^{2}\mathbf{E}_{\mathrm{A}}^{*}$ interaction, the phase of pulse A is reversed by the complex conjugation rather than cancelled by it. The signal therefore retains memory of the phase of pulse A across the delay τ. This memory is the coherence of the $|1\rangle$-$|2\rangle$ superposition: the coupled resonator system maintains a well-defined phase relationship between the bright and dark modes for a finite duration. As long

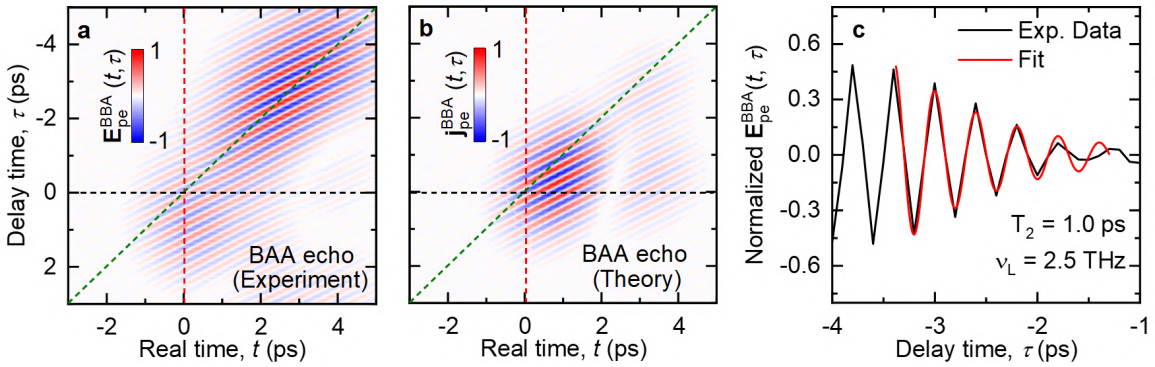

Figure 6.8: **(a)** Experimental $\mathbf{E}_{\mathrm{pe}}^{\mathrm{BAA}}(t,\tau)$ and **(b)** theoretical $\mathbf{j}_{\mathrm{pe}}^{\mathrm{BAA}}(t,\tau)$ 2D contour plots of the inverse Fourier transformed signals, respectively. Here, the green- and red-dashed lines correspond to the propagation wavefront of the driving THz fields $\mathbf{E}_{\mathrm{A}}$ and $\mathbf{E}_{\mathrm{B}}$, respectively. The black-dashed line indicates the zero delay time. **(c)** The temporal trace of $\mathbf{E}_{\mathrm{pe}}^{\mathrm{BAA}}(t,\tau)$ at a fixed real time of $t = 4.5$ ps. The red-solid curve depicts the numerical fit of Equation 6.13 of the main manuscript. Taken from Ref. [28].

as this coherence persists, the destructive interference between the two excitation pathways remains operative and the EIT window exists. When T_2 has elapsed, the phase relationship is lost and the two resonators behave as incoherently coupled oscillators. The decay of the τ-oscillation envelope directly measures how long this coherence lasts. Figure 6.7e shows that the theoretical model reproduces the oscillatory contour with high fidelity. Figure 6.7f shows the τ-trace at $t = 4.5$ ps, fitted by a damped sinusoid,

$$E_{\mathrm{pe}}^{\mathrm{ABB}}(\tau) = A_2 \sin(2\pi\nu_L\tau + \varphi)\exp\left(-\tau/T_2\right), \tag{6.13}$$

giving $T_2 = 1.0 \pm 0.1$ ps.

The BAA echo at $(\nu_0, -2\nu_0)$ gives an independent measurement of T_2 from the reversed field-ordering sequence $\mathbf{E}_{\mathrm{A}}^2\mathbf{E}_{\mathrm{B}}^*$. Fitting the same damped sinusoid to the BAA τ-trace at $t = 4.5$ ps returns $T_2 = 1.0 \pm 0.1$ ps, identical to the ABB result. The two echo signals are generated by physically distinct pulse sequences, so their convergence to the same coherence lifetime is a stringent self-consistency check. The BAA analysis is shown in Figure 6.8.

6.6.4 The Hierarchy of Timescales: T_1, T_2, and T_φ

The timescales T_1, T_2, and T_φ are defined in Chapter 2, along with the relation $1/T_2 = 1/(2T_1) + 1/T_\varphi$. The measured values are $T_1 = 1.96 \pm 0.11\,\text{ps}$ and $T_2 = 1.0 \pm 0.1\,\text{ps}$. Substituting gives $T_\varphi = 1.34 \pm 0.18\,\text{ps}$. This is consistent with the pure dephasing rate $\gamma_\varphi = 0.8\,\text{ps}^{-1}$ used in the Lindblad model, providing a direct validation of the theoretical framework. The inequality $T_2 < 2T_1$ confirms that pure dephasing is a dominant decoherence mechanism beyond population relaxation alone. Different unit cells have slightly different resonance frequencies due to lithographic variations. This distributes the phases of contributions from different unit cells, reducing the ensemble coherence faster than the energy decays in any individual resonator. These timescales place the system in the moderately coherent regime. The coherence time $T_2 \approx 1\,\text{ps}$ is long enough to sustain the destructive interference that produces the EIT window, since it exceeds the oscillation period $1/\nu_0 \approx 0.8\,\text{ps}$. At the same time, T_2 is significantly shorter than T_1, meaning the phase relationship between the two modes collapses before the energy has fully dissipated. This is characteristic of room-temperature metallic metamaterials and contrasts with cold-atom or cryogenic solid-state EIT systems where T_2 can approach or exceed $2T_1$.

Before proceeding to the dressed-state analysis, it is useful to summarize how each model parameter shapes a distinct aspect of the nonlinear response, and to establish that the extracted values are not unduly sensitive to small parametric uncertainties. The structural coupling strength g_s primarily controls the frequency splitting between the two hybridized modes and therefore sets the spectral separation between the nonlinear features in the 2D map. Varying g_s shifts the peak positions but leaves the overall topology of the spectrum intact. The population relaxation time T_1 governs the temporal decay of the pump-probe response: a longer T_1 sustains the pump-probe signal over a wider delay range, while a shorter T_1 causes it to collapse more rapidly toward zero. The coherence lifetime T_2, by

contrast, controls the visibility and spectral sharpness of the photon-echo and cross-peak features. When T_2 is short relative to the oscillation period, the echo fringes wash out and the cross-peaks broaden; when T_2 is sufficiently long, both features are well resolved. Importantly, the cross-peak signatures remain clearly visible over a coupling strength variation of $\pm 5\%$ around the fitted value of g_s (see Appendix Figure A.5), provided the coupling exceeds the dephasing rate. This robustness confirms that the dynamical parameters T_1 and T_2 extracted in this chapter reflect genuine physical properties of the EIT metamaterial and are not artefacts of a specific parameter choice.

6.7 Dressed-State Structure of the ABB Photon-Echo

The most structurally revealing result in this chapter is the multi-peak nature of the ABB photon-echo in the 2D frequency domain. For a simple two-level system, the echo would appear as a single peak at (ν_0, ν_0). The EIT metamaterial is different. The near-field coupling g_s between the bright and dark modes splits the bright-mode state into two dressed states separated by $2g_s$ around the unperturbed bright-mode frequency. Transitions involving these dressed states produce the EIT window in the linear spectrum and a multi-peak pattern in the 2D echo spectrum, because each dressed state contributes its own emission and excitation frequencies. Figure 6.9a shows the experimental ABB echo in the 2D frequency plane. Instead of the single peak expected for an uncoupled system, four distinct peaks are visible. The horizontal and vertical gray-dashed lines in the figure mark $\nu_\tau = 1.27$ THz and $\nu_t = 1.27$ THz respectively. At the intersection of these lines, where a simple two-level echo peak would be centered, there is instead a spectral hole. This hole is the direct consequence of the EIT destructive interference: at the transparency frequency, the dressed-state transition amplitudes cancel and no echo is emitted. On either side of this hole along ν_t are peaks from the lower dressed state at $\nu_t < 1.27$ THz and the upper dressed state at $\nu_t > 1.27$ THz.

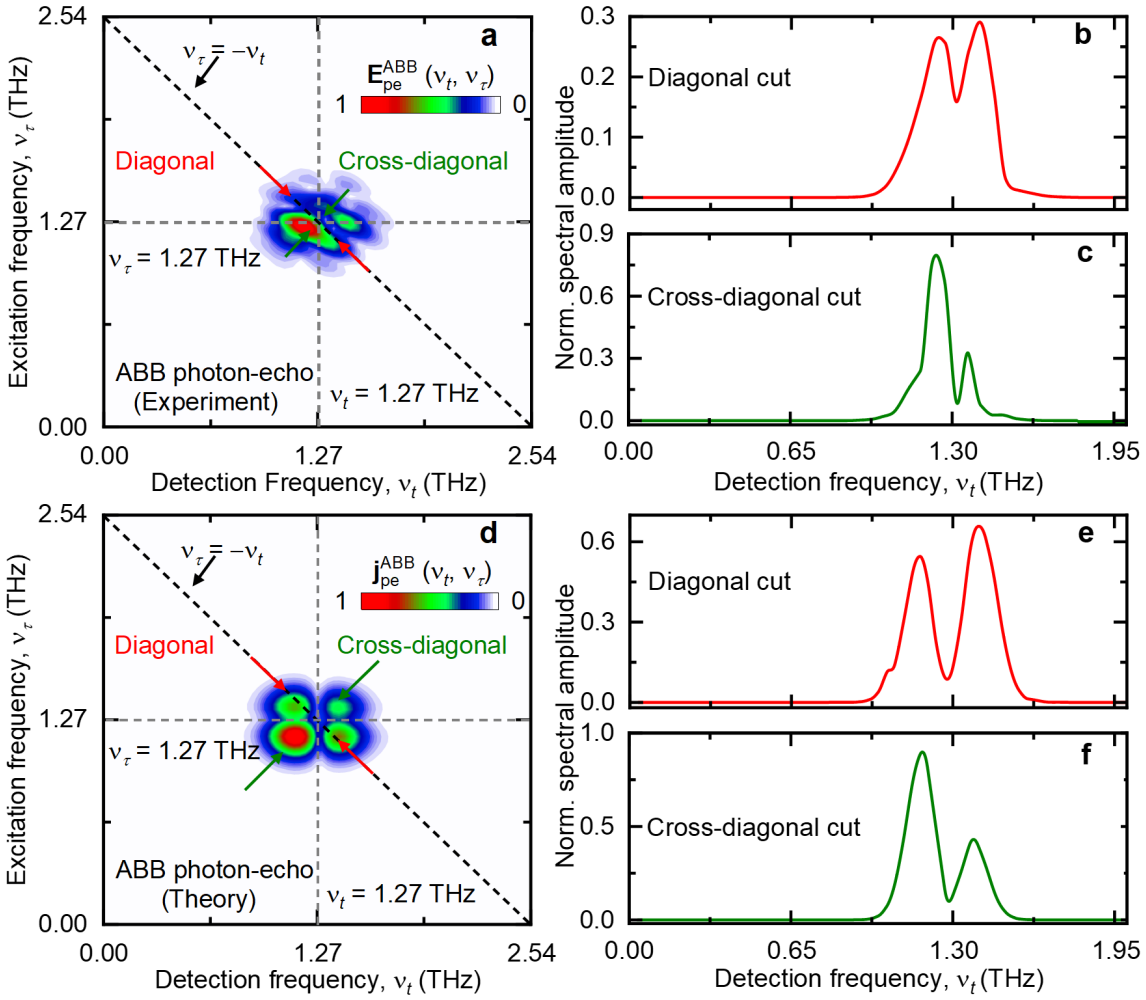

Figure 6.9: **(a)** Experimental ABB photon-echo in the 2D frequency domain showing the four-peak structure. Black-dashed diagonal: $\nu_\tau = -\nu_t$. Gray-dashed lines: $\nu_\tau = 1.27\,\mathrm{THz}$ and $\nu_t = 1.27\,\mathrm{THz}$. **(b)** Diagonal and **(c)** cross-diagonal slices from (a). **(d)** Theoretical ABB echo reproducing the four-peak pattern. **(e)** Diagonal and **(f)** cross-diagonal slices from (d). Taken from Ref. [28].

The off-diagonal structure of the four-peak pattern, visible on both sides of the black-dashed $\nu_\tau = -\nu_t$ diagonal, encodes the correlations between excitation and emission frequencies that are unique to coherently coupled multi-level systems. The theoretical simulation, as shown in Figure 6.9d reproduces this four-peak pattern with remarkable fidelity, including the spectral hole position, the dressed-state peak separations, and the relative amplitudes of all four peaks.

Figures 6.9b and 6.9c show the diagonal and cross-diagonal spectral slices extracted from the experimental echo. The diagonal slice, as depicted in Figure 6.9b is taken along the $\nu_\tau = -\nu_t$ line indicated by the black-dashed diagonal. Two peaks are resolved, corresponding to the lower and upper dressed states. The width of this slice is broad. It reflects the total spread of resonance frequencies across the fabricated metamaterial array: unit cells with slightly different lithographic dimensions have slightly different resonance frequencies, and this spread broadens the diagonal linewidth as a cumulative effect across the array. The cross-diagonal slice, as shown in Figure 6.9c is taken perpendicular to the diagonal. Its width is visibly narrower than the diagonal linewidth. This narrower width reflects only the homogeneous broadening, which is the natural lifetime broadening that results from the finite lifetimes T_1 and T_2 and that is the same for every individual unit cell regardless of its resonance frequency. The anisotropy between the diagonal and cross-diagonal linewidths is therefore the direct spectroscopic signature of inhomogeneous broadening dominating over homogeneous broadening. Figures 6.9e and 6.9f show that the theoretical model reproduces both linewidths quantitatively. This quantitative agreement confirms that the Lindblad model, with its single pure dephasing rate γ_φ, correctly partitions the total EIT linewidth into its homogeneous and inhomogeneous components.

The relative amplitudes of these four peaks are not equal. A slight spectral asymmetry between the upper and lower dressed-state peaks, present in both the experimental and theoretical echo spectra, as shown in Figure 6.9. This asymmetry has a straightforward physical origin. The bare bright and dark mode frequencies are not perfectly degenerate; a finite detuning of $\Delta = 0.05\,\mathrm{THz}$ exists between them. As a result, the two dressed states do not carry equal admixtures of the bright and dark mode characters. The dressed state with the larger bright-mode contribution couples more efficiently to the incident THz field and therefore acquires a greater spectral weight in the photon-echo signal, while the other dressed state, being more dark-mode-like, appears comparatively weaker. To verify this interpreta-

tion, the detuning was numerically set to zero in the simulation. Under this condition, the two dressed states carry identical bright-mode character, and the resulting echo spectrum becomes nearly symmetric, regardless of the damping rates assigned to either mode (see Appendix Figure A.4). An additional contribution to the asymmetry comes from the center frequency of the incident THz pulse, which is set at $f_0 = 1.0$ THz and is itself detuned from the bare bright-mode resonance at 1.20 THz. This spectral offset means that the two dressed states are not driven with equal pulse weight, further tilting the balance of the observed peak amplitudes.

This decomposition is inaccessible to any one-dimensional spectroscopic method. A conventional transmittance spectrum shows a single EIT peak whose total linewidth is the sum of both contributions, but cannot separate them. The 2D echo measurement provides the breakdown directly. The practical implication is clear. Since inhomogeneous broadening is found to dominate, improving the lithographic resolution and dimensional uniformity of the fabrication process would narrow the EIT linewidth without requiring any modification to the resonator geometry.

It is instructive to connect this dressed-state picture to the polariton physics established in Chapter 5. There, the single EIT window was split into two by introducing a phonon mode that hybridized the bright and dark resonators into upper and lower polaritons. The splitting was governed by the Rabi splitting Ω_{R}, set by the phonon-photon coupling strength. In the present chapter, no phonon is present, yet the 2D echo already reveals a doublet structure within the single EIT window. This doublet is the dressed-state pair formed by the near-field coupling g_{s} alone, before any phonon hybridization. The linear transmittance spectrum only shows the net effect of this doublet as a single transparency peak. The 2D photon-echo reveals the doublet directly. The phonon-polariton splitting of Chapter 5 is therefore a second-order modification of a dressed-state structure that already exists in the bare metamaterial. Understanding these bare dressed states provides the necessary founda-

tion for interpreting the more complex phonon-coupled system.

6.8 Conclusion

This chapter presented the first application of 2D-THz spectroscopy to an EIT metamaterial in a substrate-excitation-free configuration. By driving the coupled rod-SRR system with phase-locked THz pulse pairs and isolating the third-order nonlinear response through the three-measurement subtraction scheme, the coherent dynamics that sustain the EIT transparency window were accessed directly and independently of any substrate contribution. From the temporal decay of the $\mathrm{A_{pu}} - \mathrm{B_{pr}}$ pump-probe signal, the bright-mode relaxation time $T_1 = 1.96 \pm 0.11\,\mathrm{ps}$ was extracted. This measures how long the radiative energy stored in the rod dipole persists before it is dissipated through ohmic losses and radiative re-emission. From the oscillatory decay of the ABB and BAA photon-echo signals, the coherence lifetime $T_2 = 1.0 \pm 0.1\,\mathrm{ps}$ was determined from two independent measurements. The agreement between the two echo results is a stringent self-consistency check on the experiment. The inequality $T_2 < 2T_1$ established the presence of pure dephasing, with $T_\varphi = 1.34 \pm 0.18\,\mathrm{ps}$, attributable to structural inhomogeneity across the fabricated array. These timescales place the system in the moderately coherent regime. The near-field coupling g_s sustains the bright-dark coherence long enough for the destructive interference to produce a well-defined transparency window, but pure dephasing limits the coherence to a duration well below T_1. This is characteristic of room-temperature metallic metamaterials and reflects the inevitable structural disorder that accompanies large-area lithographic fabrication. The multi-peak structure of the ABB photon-echo in the 2D frequency domain provided a direct visualization of the dressed-state doublet that underlies the EIT transparency window. The diagonal versus cross-diagonal linewidth anisotropy quantitatively separated the homogeneous and inhomogeneous contributions to the EIT linewidth, a decomposition

inaccessible to conventional one-dimensional spectroscopy. This analysis identified structural disorder as the dominant broadening mechanism, pointing to lithographic improvement as the most effective route to sharper, higher-amplitude EIT responses.

The density matrix model based on the three-level Λ-type Hamiltonian with Lindblad dissipation reproduced all observed features quantitatively: the nonlinear time-domain signal, the 2D frequency spectrum, the pump-probe decay, the echo oscillations, and the four-peak echo structure. The agreement between the independently determined T_φ and the model parameter γ_φ validates the theoretical framework and confirms that all sources of decoherence in the system are captured by a single dephasing channel.

Chapter 7

Conclusion and Outlook

7.1 Conclusion

This thesis set out to answer two questions about EIT-like phenomena in THz metamaterials. The first was whether the single transparency window of a bright-dark mode metamaterial could be qualitatively transformed, not merely shifted or suppressed, by integrating it with a phonon-active material. The second was what coherent timescales actually sustain the transparency window, and how those timescales relate to the structural and material properties of the device. Both questions have now been answered through experiment and through theoretical models that describe the same physical system from complementary perspectives.

The first study investigated a hybrid platform in which a thin film of $MAPbI_3$ perovskite was deposited onto a fabricated rod-SRR EIT metamaterial. The $MAPbI_3$ film supports a TO phonon near 0.97 THz. When the metamaterial resonances are spectrally aligned with this phonon mode, both the rod and the SRR individually enter the strong coupling regime. The interaction potential between the phonon and the SRR resonance reaches $V = 0.538$ meV, which exceeds the strong coupling threshold $V_{\mathrm{st}} = 0.294$ meV. This confirms coherent hybridization rather than a perturbative frequency shift. Both resonators independently form upper and lower polariton branches separated by Rabi splittings of approximately 0.31 THz and 0.37 THz for the rod and SRR respectively. These overlapping polaritonic states reorganize the interference pathways responsible for the EIT window. The result is a dual EIT-like response with transparency peaks near 0.9 THz and 1.2 THz, in place of the original single window at 1.3 THz. The normalized in-plane electric field

distributions confirmed that both peaks carry genuine EIT character: the rod dipole is deactivated and the field is concentrated in the SRR gaps at both transparency frequencies, exactly as in the bare EIT structure. The group delay measurement showed that both windows retain the steep dispersion associated with EIT-like slow-light behavior. The original single delay peak of approximately 1.5 ps splits into multiple delay features, confirming that slow-light behavior is preserved and even enriched in the hybrid configuration. The rod-SRR geometry also provides intrinsic tunability. Rotating the metamaterial relative to the incident polarization switches the system continuously from the three-oscillator dual-EIT regime to a two-oscillator SRR-phonon Rabi splitting, without any structural modification. Translating the SRR along the rod length accesses the complementary rod-phonon regime. These two control parameters together demonstrate that the full range of coupled-resonator behaviors in this platform can be accessed geometrically.

The second study turned to the coherent dynamics of the bare EIT metamaterial. 2D-THz spectroscopy was applied to the same rod-SRR structure, without the $MAPbI_3$ film, in a configuration where the THz pulses themselves drive the metallic resonators directly. Because THz photon energies lie below the quartz bandgap, no substrate carriers are generated, and the nonlinear signals originate entirely from the coupled resonator system. The 2D frequency spectrum revealed four distinct third-order nonlinear signals: two pump-probe signals at $(\nu_0, 0)$ and $(\nu_0, -\nu_0)$, and two photon-echo signals at (ν_0, ν_0) and $(\nu_0, -2\nu_0)$. From the exponential decay of the pump-probe signal, the bright-mode relaxation time $T_1 = 1.96 \pm 0.11$ ps was extracted. From the oscillatory decay of the ABB and BAA photon-echo signals, the coherence lifetime $T_2 = 1.0 \pm 0.1$ ps was determined independently from two echo channels, with full mutual agreement. The relation $1/T_2 = 1/(2T_1) + 1/T_\varphi$ then gives a pure dephasing time $T_\varphi = 1.34 \pm 0.18$ ps, consistent with the dephasing rate parameter used in the Lindblad model. The inequality $T_2 < 2T_1$ confirms that phase coherence between the bright and dark modes is lost before the stored electromagnetic energy

fully dissipates. The dominant source of this additional dephasing is structural inhomogeneity: lithographic variations across the array distribute the resonance frequencies of individual unit cells, randomizing their phase contributions without dissipating their energy. The multi-peak structure of the ABB photon-echo in the 2D frequency domain provided direct visualization of the dressed-state doublet that underlies the EIT transparency window. The diagonal linewidth of this echo signal is broader than its cross-diagonal linewidth, a signature of inhomogeneous broadening exceeding the homogeneous lifetime broadening. This decomposition is inaccessible to conventional one-dimensional spectroscopic methods and establishes lithographic improvement as the most effective route to sharper, higher-contrast EIT responses.

The two studies are complementary in a precise sense. The first establishes that the spectral character of the EIT response can be fundamentally transformed through strong phonon-polariton hybridization. The second establishes what sets the temporal and spectral quality of that response in its bare form. Together they define both the ceiling and the floor of EIT performance in this metamaterial platform: the ceiling is set by the tunability and dual-window behavior made possible by phonon coupling, and the floor is set by the pure dephasing that structural disorder imposes on the coherence lifetime. The moderately coherent regime identified in the second study, where $T_2 \approx 1\,\mathrm{ps}$ is long enough to sustain EIT interference but short enough relative to T_1 to reflect significant dephasing, is characteristic of room-temperature lithographically fabricated metamaterials. Any improvement in device performance, whether in group delay, modulation depth, or transparency contrast, must ultimately address this dephasing floor. The 2D spectroscopic framework demonstrated here provides the direct measurement tool for quantifying that floor and tracking how it changes as the geometry, material, or operating conditions are varied.

7.2 Outlook

The results presented in this thesis open several concrete directions for future investigation.

The most immediate next step is to apply 2D-THz spectroscopy directly to the phonon-hybridized EIT system characterized spectrally in Chapter 5. The frequency-domain study established that the hybrid system operates in the strong coupling regime and produces dual transparency. What it could not access is how the phonon hybridization modifies the coherent timescales. Whether T_2 increases or decreases relative to the bare value of 1.0 ps when the polariton branches replace the original resonances is an open question. The $MAPbI_3$ film may introduce additional surface disorder that increases γ_φ, or the stronger effective coupling in the polaritonic branches may reduce the sensitivity to inhomogeneity and extend T_2. Distinguishing these scenarios requires a direct pump-probe and photon-echo measurement on the hybrid structure. The experimental infrastructure demonstrated in Chapter 6 is directly applicable to this experiment, and the density matrix model can be extended to a five-level system incorporating the polariton states. This single experiment would complete the dynamic picture of the hybrid platform and connect the spectral tunability of Chapter 5 to the time-resolved coherence physics of Chapter 6.

A second direction concerns the active control of the dual transparency. The $MAPbI_3$ phonon frequency is sensitive to temperature, hydrostatic pressure, and halide composition. Varying the temperature shifts the TO phonon mode, which changes the spectral alignment between the phonon and the metamaterial resonances. This provides a route to continuously tune the separation between the two transparency windows without changing the metamaterial geometry. Substituting iodide with bromide or chloride in the perovskite shifts the phonon frequency further, offering a chemical route to wider spectral coverage. Replacing $MAPbI_3$ with a polar crystal that has a narrower phonon linewidth, such as lithium niobate, would increase the Q-factor of the phonon mode and sharpen the polaritonic branches. This

would produce narrower dual transparency windows with larger group delays and stronger slow-light enhancement.

A third direction follows from the linewidth decomposition established in Chapter 6. The 2D photon-echo analysis showed that inhomogeneous broadening is the dominant limitation on EIT linewidth in the current fabrication. Improving the lithographic resolution of the maskless photolithography system, reducing the gap size tolerance below 3 μm, and tightening the uniformity of the aluminum deposition would each reduce the spread of resonance frequencies across the array. The 2D-THz measurement provides a direct diagnostic: repeated measurement of the diagonal and cross-diagonal echo linewidths as fabrication parameters are varied would quantify the improvement in homogeneity without requiring any change to the measurement infrastructure.

More broadly, the combination of engineered light-matter coupling and multidimensional THz spectroscopy demonstrated here provides a framework for investigating a wider class of phenomena. Bound states in the continuum (BICs) in THz metasurfaces produce high-Q resonances through a different interference mechanism from EIT, but they share the same bright-dark mode language and could be characterized by the same 2D-THz approach to extract their coherence properties. Near-field 2D-THz spectroscopy, in which a near-field probe is scanned across the metamaterial surface while the nonlinear signal is recorded, would give spatially resolved access to the coherence at sub-unit-cell length scales. This would directly image which regions of the fabricated array contribute homogeneously and which are responsible for the excess inhomogeneous dephasing.

In summary, THz metamaterials have emerged in this thesis as dynamic platforms where interference, coherence, and hybridization are deliberately engineered and quantitatively characterized. The integration of strong phonon-polariton coupling with two-dimensional nonlinear THz spectroscopy establishes a foundation for coherence-driven THz photonic technologies. The work presented here is a step toward a broader program in which the

spectral design freedom of metamaterials and the dynamic measurement power of multidimensional spectroscopy are used together to uncover and control the coherent physics of engineered light-matter systems.

The results presented in this thesis demonstrate that THz metamaterials provide a versatile platform for investigating coherent light-matter interaction at ultrafast timescales. While the present work has focused on phonon mediated strong-coupling and nonlinear coherent dynamics in hybrid metamaterial systems, the underlying concepts have broader implications that extend beyond the scope of this study. Recent developments in photonics and quantum science suggest several promising directions for future research.

One important direction is the exploration of coherent control in quantum information processing. Although the present experiments were performed on a classical metamaterial platform, the observation of coherent energy exchange, together with the experimentally measured population relaxation and coherence lifetimes, demonstrates the ability to generate, manipulate, and probe coherent hybrid states on picosecond timescales. Similar concepts form the basis of quantum coherent control in cavity quantum electrodynamics and other quantum photonic platforms. Future studies combining THz spectroscopy with low temperature measurements or quantum materials may provide new opportunities for investigating coherent quantum phenomena in the THz frequency range [134–136].

Another emerging research direction is cavity-free quantum electrodynamics, where strong light-matter interaction is achieved without the use of conventional optical cavities. Instead, highly confined electromagnetic fields produced by metallic nanostructures or metamaterials enable coherent coupling with material excitations. The phonon polariton coupling demonstrated in Chapter 5 represents an example of this approach, where the engineered metamaterial resonance interacts directly with the optical phonon of the $MAPbI_3$ layer. Such systems provide an attractive platform for investigating strong-coupling in compact photonic structures and may facilitate the development of miniaturized THz de-

vices [3, 137].

The tunability of the EIT response also offers interesting possibilities for topological photonics. The independently controlled transparency windows and slow light characteristics demonstrated in this thesis could be integrated with topological photonic architectures to realize robust THz waveguiding and protected transport of electromagnetic energy. Although such investigations are beyond the scope of the present work, recent advances in THz topological photonics indicate that combining engineered metamaterials with topological concepts may enable compact and low loss THz communication systems with enhanced functionality [138–140].

Another promising direction is the development of integrated THz photonic technologies. The ability to engineer resonance frequencies, quality factors, and coupling strengths through structural design makes metamaterials attractive building blocks for compact THz components. Hybrid integration of semiconductors, perovskites, phase-change materials, and other functional materials may enable actively tunable filters, modulators, sensors, and slow-light devices operating in the THz frequency range. Together with recent advances in integrated photonic platforms, these developments could contribute to future THz communication, imaging, and sensing technologies [141–143].

Overall, the concepts developed in this thesis establish a foundation for future investigations of coherent light-matter interaction using engineered THz metamaterials. By combining strong coupling, ultrafast spectroscopy, and hybrid material systems, this platform offers opportunities to explore both fundamental physical phenomena and practical device applications. Future research along these directions is expected to further strengthen the role of THz metamaterials in modern photonics and quantum technologies.

References

[1] D. G. Baranov, M. Wersall, J. Cuadra, T. J. Antosiewicz, and T. Shegai. Novel nanostructures and materials for strong light-matter interactions. *ACS Photonics*, 5(1):24–42, 2018.

[2] D. S. Dovzhenko, S. V. Ryabchuk, Y. P. Rakovich, and I. R. Nabiev. Light-matter interaction in the strong coupling regime: configurations, conditions, and applications. *Nanoscale*, 10(8):3589–3605, 2018.

[3] F. J. Garcia-Vidal, C. Ciuti, and T. W. Ebbesen. Manipulating matter by strong coupling to vacuum fields. *Science*, 373(6551):eabd0336, 2021.

[4] P. Törmä and W. L. Barnes. Strong coupling between surface plasmon polaritons and emitters: a review. *Reports on Progress in Physics*, 78(1):013901, 2015.

[5] S. E. Harris. Electromagnetically induced transparency. *Physics Today*, 50(7):36–42, 1997.

[6] C. L. Garrido Alzar, M. A. G. Martinez, and P. Nussenzveig. Classical analog of electromagnetically induced transparency. *American Journal of Physics*, 70(1):37–41, 2002.

[7] L. V. Hau, S. E. Harris, Z. Dutton, and C. H. Behroozi. Light speed reduction to 17 metres per second in an ultracold atomic gas. *Nature*, 397(6720):594–598, 1999.

[8] B.-W. Shiau, M.-C. Wu, C.-C. Lin, and Y.-C. Chen. Low-light-level cross-phase modulation with double slow light pulses. *Physical Review Letters*, 106(19):193006, 2011.

[9] L.-M. Kuang, G.-H. Chen, and Y.-S. Wu. Nonlinear optical properties of an electromagnetically induced transparency medium interacting with two quantized fields. *Journal of Optics B: Quantum and Semiclassical Optics*, 5(4):341–348, 2003.

[10] D. F. Phillips, A. Fleischhauer, A. Mair, R. L. Walsworth, and M. D. Lukin. Storage of light in atomic vapor. *Physical Review Letters*, 86(5):783–786, 2001.

[11] C. Liu, Z. Dutton, C. H. Behroozi, and L. V. Hau. Observation of coherent optical information storage in an atomic medium using halted light pulses. *Nature*, 409(6819):490–493, 2001.

[12] M. Fleischhauer and M. D. Lukin. Quantum memory for photons: Dark-state polaritons. *Physical Review A*, 65(2):022314, 2002.

[13] V. M. Datsyuk, I. M. Sokolov, D. V. Kupriyanov, and M. D. Havey. Electromagnetically induced optical anisotropy of an ultracold atomic medium. *Physical Review A*, 77(3):033823, 2008.

[14] S. Bhushan, V. S. Chauhan, and R. K. Easwaran. Ultracold rydberg atoms for efficient storage of terahertz frequency signals using electromagnetically induced transparency. *Physics Letters A*, 382(48):3500–3504, 2018.

[15] A. Haldar, K. V. Goyal, R. V. Puranik, V. Dwij, S. Maity, K. R. Khator, S. Ghosh, B. S. Chouhan, G. Kumar, S. P. Senanayak, et al. Phonon-polariton mediated dual electromagnetically induced transparency-like response in a THz metamaterial. *Advanced Quantum Technologies*, 9(2):e00368, 2026.

[16] L. Zhu and L. Dong. Electromagnetically induced transparency metamaterials: theories, designs, and applications. *Journal of Physics D: Applied Physics*, 55(26):263003, 2022.

[17] Z. Xu, Y. Wang, S. Liu, J. Ma, S. Fang, and H. Wu. Metamaterials with analogous electromagnetically induced transparency and related sensor designs–a review. *IEEE Sensors Journal*, 23(7):6378–6396, 2023.

[18] P. Tassin, L. Zhang, T. Koschny, E. N. Economou, and C. M. Soukoulis. Planar designs for electromagnetically induced transparency in metamaterials. *Optics Express*, 17(7):5595–5601, 2009.

[19] H. S. Kim, N. Y. Ha, J.-Y. Park, S. Lee, D.-S. Kim, and Y. H. Ahn. Phonon-polaritons in lead halide perovskite film hybridized with thz metamaterials. *Nano Letters*, 20(9):6690–6696, 2020.

[20] Q. Zhang, M. Lou, X. Li, J. L. Reno, W. Pan, J. D. Watson, M. J. Manfra, and J. Kono. Collective non-perturbative coupling of 2D electrons with high-quality-factor terahertz cavity photons. *Nature Physics*, 12(11):1005–1011, 2016.

[21] Z. Zhang, H. Hirori, F. Sekiguchi, A. Shimazaki, Y. Iwasaki, T. Nakamura, A. Wakamiya, and Y. Kanemitsu. Ultrastrong coupling between THz phonons and photons caused by an enhanced vacuum electric field. *Physical Review Research*, 3(3):L032021, 2021.

[22] Y. Roh, M. Chae, J. Oh, W. Kim, M.-Y. Ryu, M. Seo, and J. Jeong. Ultrastrong coupling enhancement with squeezed mode volume in terahertz nanoslots. *Nano Letters*, 23(15):7086–7091, 2023.

[23] H. S. Kim, A. A. Khan, J.-Y. Park, S. Lee, and Y. H. Ahn. Mechanical control of polaritonic states in lead halide perovskite phonons strongly coupled in thz microcavity. *The Journal of Physical Chemistry Letters*, 14(46):10318–10327, 2023.

[24] S. Hu, W. He, M. Tong, Z. Xu, Y. Hu, X.-A. Cheng, and T. Jiang. Dual-dimensional EIT manipulation for angle-multiplexed ultrafast terahertz switching. *ACS Photonics*, 10(7):2182–2191, 2022.

[25] W. X. Lim, M. Manjappa, Y. K. Srivastava, L. Cong, A. Kumar, K. F. MacDonald, and R. Singh. Ultrafast all-optical switching of germanium-based flexible metaphotonic devices. *Advanced Materials*, 30(9):1705331, 2018.

[26] Y. Deng, Q. Zhou, P. Zhang, N. Jiang, T. Ning, W. Liang, and C. Zhang. Heterointerface-enhanced ultrafast optical switching via manipulating metamaterial-induced transparency in a hybrid terahertz graphene metamaterial. *ACS Applied Materials & Interfaces*, 13(11):13565–13575, 2021.

[27] Y. Hu, M. Tong, X.-A. Cheng, J. Zhang, H. Hao, J. You, X. Zheng, and T. Jiang. Bi_2Se_3-functionalized metasurfaces for ultrafast all-optical switching and efficient modulation of terahertz waves. *ACS Photonics*, 8(3):771–780, 2021.

[28] A. Haldar, S. Prabhu, and S. Pal. Unveiling nonlinearities of electromagnetically induced transparency in a THz metamaterial. *Advanced Functional Materials*, page e75422, 2026.

[29] R. Loudon. *The quantum theory of light*. Oxford University Press, Great Britain, 2000.

[30] M. O. Scully and M. S. Zubairy. *Quantum optics*. Cambridge University Press, Cambridge, 1997.

[31] H. Deng, H. Haug, and Y. Yamamoto. Exciton-polariton bose-einstein condensation. *Reviews of Modern Physics*, 82(2):1489–1537, 2010.

[32] O. Bitton, S. N. Gupta, and G. Haran. Quantum dot plasmonics: from weak to strong coupling. *Nanophotonics*, 8(4):559–575, 2019.

[33] D. Wang. Cavity quantum electrodynamics with a single molecule: Purcell enhancement, strong coupling and single-photon nonlinearity. *Journal of Physics B: Atomic, Molecular and Optical Physics*, 54(13):133001, 2021.

[34] X. Yu, Y. Yuan, J. Xu, K.-T. Yong, J. Qu, and J. Song. Strong coupling in microcavity structures: principle, design, and practical application. *Laser & Photonics Reviews*, 13(1):1800219, 2019.

[35] A. Canales, O. Kotov, and T. Shegai. Perfect absorption and strong coupling in supported MoS_2 multilayers. *ACS Nano*, 17(4):3401–3411, 2023.

[36] K. Hirai, J. A. Hutchison, and H. Uji-i. Molecular chemistry in cavity strong coupling. *Chemical Reviews*, 123(13):8099–8126, 2023.

[37] Z. He, C. Xu, W. He, J. He, Y. Zhou, and F. Li. Principle and applications of multimode strong coupling based on surface plasmons. *Nanomaterials*, 12(8):1242, 2022.

[38] L. Qiu, A. Mandal, O. Morshed, M. T. Meidenbauer, W. Girten, P. Huo, A. N. Vamivakas, and T. D. Krauss. Molecular polaritons generated from strong coupling between CdSe nanoplatelets and a dielectric optical cavity. *The Journal of Physical Chemistry Letters*, 12(20):5030–5038, 2021.

[39] B. Xiang and W. Xiong. Molecular polaritons for chemistry, photonics, and quantum technologies. *Chemical Reviews*, 124(5):2512–2552, 2024.

[40] S. Haroche and J.-M. Raimond. *Exploring the Quantum: Atoms, Cavities, and Photons*. Oxford University Press, Oxford, 2006.

[41] J. A. Gyamfi. Fundamentals of quantum mechanics in liouville space. *European Journal of Physics*, 41(6):063002, 2020.

[42] G. Kiršanskas, M. Franckié, and A. Wacker. Phenomenological position- and energy-resolving lindblad approach to quantum kinetics. *Physical Review B*, 97(3):035432, 2018.

[43] J.-Y.-R. Jin, H.-Y. Zhang, Y.-X. Yao, R.-H. Chen, and Q. Ai. Observing quantum coherent oscillations in a three-level atom via electromagnetically induced transparency by two-dimensional spectroscopy. *The Journal of Chemical Physics*, 162(1):014112, 2025.

[44] J. Raab, C. Lange, J. L. Boland, I. Laepple, M. Furthmeier, E. Dardanis, N. Dessmann, L. Li, E. H. Linfield, A. G. Davies, et al. Ultrafast two-dimensional field spectroscopy of terahertz intersubband saturable absorbers. *Optics Express*, 27(3):2248–2257, 2019.

[45] Y.-C. Liu, B.-B. Li, and Y.-F. Xiao. Electromagnetically induced transparency in optical microcavities. *Nanophotonics*, 6(5):789–811, 2017.

[46] W. Huang, S. Liu, S. Cao, C. Guo, S. Yin, X. Du, and W. Zhang. Quantum master equation for coupling mechanism of metamaterial. *Results in Physics*, 34:105262, 2022.

[47] X.-H. Deng, E. Barnes, and S. E. Economou. Robustness of error-suppressing entangling gates in cavity-coupled transmon qubits. *Physical Review B*, 96(3):035441, 2017.

[48] J. B. Pendry, A. J. Holden, D. J. Robbins, and W. J. Stewart. Magnetism from conductors and enhanced nonlinear phenomena. *IEEE Transactions on Microwave Theory and Techniques*, 47(11):2075–2084, 1999.

[49] N. I. Zheludev. The road ahead for metamaterials. *Science*, 328(5978):582–583, 2010.

[50] R. A. Shelby, D. R. Smith, S. C. Nemat-Nasser, and S. Schultz. Microwave transmission through a two-dimensional, isotropic, left-handed metamaterial. *Applied Physics Letters*, 78(4):489–491, 2001.

[51] N. Meinzer, W. L. Barnes, and I. R. Hooper. Plasmonic meta-atoms and metasurfaces. *Nature Photonics*, 8(12):889–898, 2014.

[52] B. Wood. Structure and properties of electromagnetic metamaterials. *Laser & Photonics Reviews*, 1(3):249–259, 2007.

[53] M. G. Silveirinha. Metamaterial homogenization approach with application to the characterization of microstructured composites with negative parameters. *Physical Review B*, 75(11):115104, 2007.

[54] W. J. Padilla, A. J. Taylor, C. Highstrete, M. Lee, and R. D. Averitt. Dynamical electric and magnetic metamaterial response at terahertz frequencies. *Physical Review Letters*, 96(10):107401, 2006.

[55] Y. Liu and X. Zhang. Metamaterials: a new frontier of science and technology. *Chemical Society Reviews*, 40(5):2494–2507, 2011.

[56] D. R. Smith, J. B. Pendry, and M. C. K. Wiltshire. Metamaterials and negative refractive index. *Science*, 305(5685):788–792, 2004.

[57] V. G. Veselago. The electrodynamics of substances with simultaneously negative values of ε and μ. *Soviet Physics Uspekhi*, 10(4):509–514, 1968.

[58] J. C. Bose. On the rotation of plane of polarisation of electric wave by a twisted structure. *Proceedings of the Royal Society of London*, 63:146–152, 1898.

[59] D. T. Emerson. The work of jagadis chandra bose 100 years of mm-wave research. *IEEE Transactions on Microwave Theory and Techniques*, 45(12):2267–2273, 1997.

[60] J. B. Pendry, A. J. Holden, W. J. Stewart, and I. Youngs. Extremely low frequency plasmons in metallic mesostructures. *Physical Review Letters*, 76(25):4773, 1996.

[61] J. B. Pendry, A. J. Holden, D. J. Robbins, and W. J. Stewart. Low frequency plasmons in thin-wire structures. *Journal of Physics: Condensed Matter*, 10(22):4785–4809, 1998.

[62] R. A. Shelby, D. R. Smith, and S. Schultz. Experimental verification of a negative index of refraction. *Science*, 292(5514):77–79, 2001.

[63] D. R. Smith, W. J. Padilla, D. C. Vier, S. C. Nemat-Nasser, and S. Schultz. Composite medium with simultaneously negative permeability and permittivity. *Physical Review Letters*, 84(18):4184, 2000.

[64] W. Cai and V. M. Shalaev. *Optical metamaterials: fundamentals and applications*. Springer, New York, 2016.

[65] R. Singh, I. Al-Naib, D. R. Chowdhury, L. Cong, C. Rockstuhl, and W. Zhang. Probing the transition from an uncoupled to a strong near-field coupled regime between bright and dark mode resonators in metasurfaces. *Applied Physics Letters*, 105(8), 2014.

[66] J. Wallauer, A. Bitzer, S. Waselikowski, and M. Walther. Near-field signature of electromagnetic coupling in metamaterial arrays: a terahertz microscopy study. *Optics Express*, 19(18):17283–17292, 2011.

[67] M.-L. Wan, J.-N. He, Y.-L. Song, and F.-Q. Zhou. Electromagnetically induced transparency and absorption in plasmonic metasurfaces based on near-field coupling. *Physics Letters A*, 379(30–31):1791–1795, 2015.

[68] P. Pitchappa, M. Manjappa, C. P. Ho, Y. Qian, R. Singh, N. Singh, and C. Lee. Active control of near-field coupling in conductively coupled microelectromechanical system metamaterial devices. *Applied Physics Letters*, 108(11), 2016.

[69] L. Wang, X. Guo, Y. Zhang, X. Zhou, L. Yuan, P. Zhang, S. Liang, F. Lan, H. Zeng, T. Zhang, et al. Enhanced THz EIT resonance based on the coupled electric field dropping effect within the undulated meta-surface. *Nanophotonics*, 8(6):1071–1078, 2019.

[70] B.-X. Wang, Y. Sun, W. Zhou, Y. Chen, G. Yang, H. Xiong, and Z. Huang. Metamaterial-based electromagnetically induced transparency. *Advanced Functional Materials*, 35(47):2508025, 2025.

[71] K.-J. Boller, A. Imamoglu, and S. E. Harris. Observation of electromagnetically induced transparency. *Physical Review Letters*, 66(20):2593, 1991.

[72] J. P. Marangos. Electromagnetically induced transparency. *Journal of Modern Optics*, 45(3):471–503, 1998.

[73] M. Fleischhauer, A. Imamoglu, and J. P. Marangos. Electromagnetically induced transparency: optics in coherent media. *Reviews of Modern Physics*, 77(2):633–673, 2005.

[74] G. Liu, A. S. Sizhuk, and K. E. Dorfman. Selective elimination of homogeneous broadening by multidimensional spectroscopy in the electromagnetically induced transparency regime. *The Journal of Physical Chemistry Letters*, 11(14):5504–5509, 2020.

[75] I. Novikova, R. L. Walsworth, and Y. Xiao. Electromagnetically induced transparency-based slow and stored light in warm atoms. *Laser & Photonics Reviews*, 6(3):333–353, 2012.

[76] S. Zhang, D. A. Genov, Y. Wang, M. Liu, and X. Zhang. Plasmon-induced transparency in metamaterials. *Physical Review Letters*, 101(4):047401, 2008.

[77] P. Tassin, L. Zhang, T. Koschny, E. N. Economou, and C. M. Soukoulis. Low-loss metamaterials based on classical electromagnetically induced transparency. *Physical Review Letters*, 102(5):053901, 2009.

[78] R. Singh, C. Rockstuhl, F. Lederer, and W. Zhang. Coupling between a dark and a bright eigenmode in a terahertz metamaterial. *Physical Review B*, 79(8):085111, 2009.

[79] S.-Y. Chiam, R. Singh, C. Rockstuhl, F. Lederer, W. Zhang, and A. A. Bettiol. Analogue of electromagnetically induced transparency in a terahertz metamaterial. *Physical Review B*, 80(15):153103, 2009.

[80] X. Liu, J. Gu, R. Singh, Y. Ma, J. Zhu, Z. Tian, M. He, J. Han, and W. Zhang. Electromagnetically induced transparency in terahertz plasmonic metamaterials via dual excitation pathways of the dark mode. *Applied Physics Letters*, 100(13), 2012.

[81] Y. Ling, L. Huang, W. Hong, T. Liu, J. Luan, W. Liu, J. Lai, and H. Li. Polarization-controlled dynamically switchable plasmon-induced transparency in plasmonic metamaterial. *Nanoscale*, 10(41):19517–19523, 2018.

[82] R. Degl'Innocenti, H. Lin, and M. Navarro-C'ıa. Recent progress in terahertz metamaterial modulators. *Nanophotonics*, 11(8):1485–1514, 2022.

[83] T.-T. Kim, H.-D. Kim, R. Zhao, S. S. Oh, T. Ha, D. S. Chung, Y. H. Lee, B. Min, and S. Zhang. Electrically tunable slow light using graphene metamaterials. *ACS Photonics*, 5(5):1800–1807, 2018.

[84] H. Wang, Y. Zhang, F. Hu, M. Jiang, L. Zhang, W. Zhang, and J. Han. Active dual-control terahertz electromagnetically induced transparency analog in VO_2 metasurface. *Applied Physics Letters*, 123(6), 2023.

[85] C. Li, W. Li, S. Duan, J. Wu, B. Chen, S. Yang, R. Su, C. Jiang, C. Zhang, B. Jin, et al. Electrically tunable electromagnetically induced transparency in superconducting terahertz metamaterials. *Applied Physics Letters*, 119(5), 2021.

[86] P. Q. Liu, I. J. Luxmoore, S. A. Mikhailov, N. A. Savostianova, F. Valmorra, J. Faist, and G. R. Nash. Highly tunable hybrid metamaterials employing split-ring resonators strongly coupled to graphene surface plasmons. *Nature Communications*, 6(1):8969, 2015.

[87] G. Li, J. Yang, Z. Zhang, Y. Tao, L. Zhou, H. Huang, Z. Zhang, and Y. Han. Double electromagnetically induced transparency and its slow light application based on a guided-mode resonance grating cascade structure. *Materials*, 13(17):3710, 2020.

[88] Serge Haroche and J-M Raimond. *Exploring the quantum: atoms, cavities, and photons*. Oxford University Press, 2006.

[89] H Jeff Kimble. Strong interactions of single atoms and photons in cavity qed. *Physica Scripta*, 1998(T76):127–137, 1998.

[90] Claude Weisbuch, Mr Nishioka, A Ishikawa, and Yasuhiko Arakawa. Observation of the coupled exciton-photon mode splitting in a semiconductor quantum microcavity. *Physical Review Letters*, 69(23):3314, 1992.

[91] Alexandre Blais, Ren-Shou Huang, Andreas Wallraff, Steven M Girvin, and R Jun Schoelkopf. Cavity quantum electrodynamics for superconducting electrical circuits: An architecture for quantum computation. *Physical Review A—Atomic, Molecular, and Optical Physics*, 69(6):062320, 2004.

[92] María Barra-Burillo, Unai Muniain, Sara Catalano, Marta Autore, Fèlix Casanova, Luis E Hueso, Javier Aizpurua, Ruben Esteban, and Rainer Hillenbrand. Microcavity phonon polaritons from the weak to the ultrastrong phonon–photon coupling regime. *Nature Communications*, 12(1):6206, 2021.

[93] Sirak M Mekonen, Deepti Jain, Seongshik Oh, and NP Armitage. Coupled metamaterial–phonon terahertz range polaritons in a topological insulator. *ACS Photonics*, 11(6):2242–2246, 2024.

[94] Peter Hamm and Martin T Zanni. *Concepts and methods of 2D infrared spectroscopy*, volume 1. Cambridge University Press Cambridge, 2011.

[95] A. Dutta, P. Shee, A. Haldar, and S. Pal. 2D-THz spectroscopy: exploring the nonlinear dynamics in quantum materials. *Journal of Physics: Condensed Matter*, 37(20):203002, 2025.

[96] Albert Liu. Multidimensional terahertz probes of quantum materials. *npj Quantum Materials*, 10(1):18, 2025.

[97] Y.-S. Lee. *Principles of terahertz science and technology*. Springer, 2009.

[98] M. Kozina, M. Fechner, P. Marsik, T. van Driel, J. M. Glownia, C. Bernhard, M. Radovic, D. Zhu, S. Bonetti, U. Staub, et al. Terahertz-driven phonon upconversion in $SrTiO_3$. *Nature Physics*, 15(4):387–392, 2019.

[99] H. Han, B. Li, S. Volz, and Y. A. Kosevich. Ultracompact interference phonon nanocapacitor for storage and lasing of coherent terahertz lattice waves. *Physical Review Letters*, 114(14):145501, 2015.

[100] S. Sheng, M. Abdo, S. Rolf-Pissarczyk, K. Lichtenberg, S. Baumann, J. A. J. Burgess, L. Malavolti, and S. Loth. Terahertz spectroscopy of collective charge density wave dynamics at the atomic scale. *Nature Physics*, 20(10):1603–1608, 2024.

[101] C.-J. Yang, J. Li, M. Fiebig, and S. Pal. Terahertz control of many-body dynamics in quantum materials. *Nature Reviews Materials*, 8(8):518–532, 2023.

[102] N. M. Burford and M. O. El-Shenawee. Review of terahertz photoconductive antenna technology. *Optical Engineering*, 56(1):010901, 2017.

[103] S. Lepeshov, A. Gorodetsky, A. Krasnok, E. Rafailov, and P. Belov. Enhancement of terahertz photoconductive antenna operation by optical nanoantennas. *Laser & Photonics Reviews*, 11(1):1600199, 2017.

[104] X.-C. Zhang, X.-F. Ma, Y. Jin, T.-M. Lu, E. P. Boden, P. D. Phelps, K. R. Stewart, and C. P. Yakymyshyn. Terahertz optical rectification from a nonlinear organic crystal. *Applied Physics Letters*, 61(26):3080–3082, 1992.

[105] A. Rice, Y. Jin, X.-F. Ma, X.-C. Zhang, D. Bliss, J. Larkin, and M. Alexander. Terahertz optical rectification from $\langle 110 \rangle$ zinc-blende crystals. *Applied Physics Letters*, 64(11):1324–1326, 1994.

[106] A. Nahata, A. S. Weling, and T. F. Heinz. A wideband coherent terahertz spectroscopy system using optical rectification and electro-optic sampling. *Applied Physics Letters*, 69(16):2321–2323, 1996.

[107] Y. Kang, T. Li, Z. Wang, Y. Wang, C. Yu, W. Yin, Z. Gao, H. Xu, H. Luo, X. Wang, et al. Continuous terahertz band coverage through precise electron-beam tailoring in free-electron lasers. *Nature Photonics*, 20(1):96–101, 2026.

[108] C. Walther, M. Fischer, G. Scalari, R. Terazzi, N. Hoyler, and J. Faist. Quantum cascade lasers operating from 1.2 to 1.6 THz. *Applied Physics Letters*, 91(13):131122, 2007.

[109] G. Scalari, C. Walther, M. Fischer, R. Terazzi, H. Beere, D. Ritchie, and J. Faist. THz and sub-THz quantum cascade lasers. *Laser & Photonics Reviews*, 3(1–2):45–66, 2009.

[110] P. R. Smith, D. H. Auston, and M. C. Nuss. Subpicosecond photoconducting dipole antennas. *IEEE Journal of Quantum Electronics*, 24(2):255–260, 1988.

[111] R. W. Boyd. *Nonlinear Optics*. Academic Press, 2020.

[112] I. Wilke and S. Sengupta. Nonlinear optical techniques for terahertz pulse generation and detection: optical rectification and electro-optic sampling. In *Terahertz Spectroscopy*. CRC Press, 2017.

[113] P. C. M. Planken, H.-K. Nienhuys, H. J. Bakker, and T. Wenckebach. Measurement and calculation of the orientation dependence of terahertz pulse detection in ZnTe. *Journal of the Optical Society of America B*, 18(3):313–317, 2001.

[114] O. Hatem. Peak emission of terahertz waves from (110)-oriented ZnTe by interacting phase-matched phonon resonances. *Journal of the Optical Society of America B*, 36(4):1144–1149, 2019.

[115] T. Elsaesser, K. Reimann, and M. Woerner. *Concepts and applications of nonlinear terahertz spectroscopy*. IOP Publishing, 2024.

[116] W. Kuehn, K. Reimann, M. Woerner, T. Elsaesser, and R. Hey. Two-dimensional THz correlation spectra of electronic excitations in semiconductor quantum wells. *The Journal of Physical Chemistry B*, 115(18):5448–5455, 2011.

[117] W. Kuehn, K. Reimann, M. Woerner, T. Elsaesser, R. Hey, and U. Schade. Strong correlation of electronic and lattice excitations in GaAs/AlGaAs semiconductor quantum wells revealed by two-dimensional THz spectroscopy. *Physical Review Letters*, 107(6):067401, 2011.

[118] S. Markmann, M. Franckié, S. Pal, D. Stark, M. Beck, M. Fiebig, G. Scalari, and J. Faist. Two-dimensional spectroscopy on a THz quantum cascade structure. *Nanophotonics*, 10(1):171–180, 2020.

[119] J. Lu, X. Li, H. Y. Hwang, B. K. Ofori-Okai, T. Kurihara, T. Suemoto, and K. A. Nelson. Coherent two-dimensional THz magnetic resonance spectroscopy of collective spin waves. *Physical Review Letters*, 118(20):207204, 2017.

[120] Z. Zhang, F. Y. Gao, J. B. Curtis, Z.-J. Liu, Y.-C. Chien, A. von Hoegen, M. T. Wong, T. Kurihara, T. Suemoto, P. Narang, et al. THz field-induced nonlinear coupling of two magnon modes in an antiferromagnet. *Nature Physics*, 20(5):801–806, 2024.

[121] A. Gómez Salvador, P. E. Dolgirev, M. H. Michael, A. Liu, D. Pavicevic, M. Fechner, A. Cavalleri, and E. Demler. Principles of two-dimensional THz spectroscopy of collective excitations: the case of josephson plasmons in layered superconductors. *Physical Review B*, 110(9):094514, 2024.

[122] B. Cheng, D. Cheng, K. Lee, M. Mootz, C. Huang, L. Luo, Z. Chen, Y. Lee, B. Y. Wang, I. E. Perakis, et al. Observation of cuprate-like nonlinear THz responses in superconducting infinite-layer nickelates via two-dimensional coherent spectroscopy. *Physical Review B*, 111(1):014519, 2025.

[123] F. Gerken, T. Posske, S. Mukamel, and M. Thorwart. Unique signatures of topological phases in two-dimensional THz spectroscopy. *Physical Review Letters*, 129(1):017401, 2022.

[124] T. G. H. Blank, K. A. Grishunin, K. A. Zvezdin, N. T. Hai, J. C. Wu, S.-H. Su, J.-C. A. Huang, A. K. Zvezdin, and A. V. Kimel. Two-dimensional THz spectroscopy of nonlinear phononics in the topological insulator $MnBi_2Te_4$. *Physical Review Letters*, 131(2):026902, 2023.

[125] T. Weiland, M. Timm, and I. Munteanu. A practical guide to 3D simulation. *IEEE Microwave Magazine*, 9(6):62–75, 2008.

[126] M. Manjappa. *Elucidating the effects of radiant and sub-radiant interactions in terahertz metamaterials*. PhD thesis, Nanyang Technological University, 2018.

[127] W.-Z. Yuan, Y. Guo, C.-L. Zhou, and H.-L. Yi. Radiative thermal diode driven by the synergy between isotope engineering and lattice thermal expansion. *Physical Review B*, 110(16):165412, 2024.

[128] T. Fujii, A. Ando, and Y. Sakabe. Characterization of dielectric properties of oxide materials in frequency range from ghz to THz. *Journal of the European Ceramic Society*, 26(10–11):1857–1860, 2006.

[129] C. L. Davies, J. B. Patel, C. Q. Xia, L. M. Herz, and M. B. Johnston. Temperature-dependent refractive index of quartz at THz frequencies. *Journal of Infrared, Millimeter, and Terahertz Waves*, 39(12):1236–1248, 2018.

[130] M. Sendner, P. K. Nayak, D. A. Egger, S. Beck, C. Müller, B. Epding, W. Kowalsky, L. Kronik, H. J. Snaith, A. Pucci, and R. Lovrinčić. Optical phonons in methylammonium lead halide perovskites and implications for charge transport. *Materials Horizons*, 3(6):613–620, 2016.

[131] S. R. Konda, Y. Lin, R. A. Rajan, W. Yu, and W. Li. Measurement of optical properties of $CH_3NH_3PbX_3$ (X = Br, I) single crystals using terahertz time-domain spectroscopy. *Materials*, 16(2):610, 2023.

[132] A. K. Azad and W. Zhang. Resonant terahertz transmission in subwavelength metallic hole arrays of sub-skin-depth thickness. *Optics Letters*, 30(21):2945–2947, 2005.

[133] A. Baydin, M. Manjappa, S. S. Mishra, H. Xu, J. Doumani, F. Tay, D. Kim, P. H. O. Rappl, E. Abramof, R. Singh, et al. Terahertz cavity phonon polaritons in lead telluride in the deep-strong coupling regime. *arXiv preprint*, 2025.

[134] H Jeff Kimble. The quantum internet. *Nature*, 453(7198):1023–1030, 2008.

[135] Alexandre Blais, Arne L Grimsmo, Steven M Girvin, and Andreas Wallraff. Circuit quantum electrodynamics. *Reviews of Modern Physics*, 93(2):025005, 2021.

[136] David D Awschalom, Ronald Hanson, Jörg Wrachtrup, and Brian B Zhou. Quantum technologies with optically interfaced solid-state spins. *Nature Photonics*, 12(9):516–527, 2018.

[137] Frank Schlawin, Dante M Kennes, and Michael A Sentef. Cavity quantum materials. *Applied Physics Reviews*, 9(1), 2022.

[138] Mikhail I Shalaev, Wiktor Walasik, Alexander Tsukernik, Yun Xu, and Natalia M Litchinitser. Robust topologically protected transport in photonic crystals at telecommunication wavelengths. *Nature Nanotechnology*, 14(1):31–34, 2019.

[139] Yihao Yang, Yuichiro Yamagami, Xiongbin Yu, Prakash Pitchappa, Julian Webber, Baile Zhang, Masayuki Fujita, Tadao Nagatsuma, and Ranjan Singh. Terahertz topological photonics for on-chip communication. *Nature Photonics*, 14(7):446–451, 2020.

[140] Abhishek Kumar, Manoj Gupta, Prakash Pitchappa, Nan Wang, Pascal Szriftgiser, Guillaume Ducournau, and Ranjan Singh. Phototunable chip-scale topological photonics: 160 gbps waveguide and demultiplexer for thz 6g communication. *Nature Communications*, 13(1):5404, 2022.

[141] Daniel M Mittleman. Twenty years of terahertz imaging. *Optics Express*, 26(8):9417–9431, 2018.

[142] Joel Yuen-Zhou and Wei Xiong. Strong coupling of organic molecules 2023 (scom23), 2024.

[143] Dmitri N Basov, Ana Asenjo-Garcia, P James Schuck, Xiaoyang Zhu, and Angel Rubio. Polariton panorama. *Nanophotonics*, 10(1):549–577, 2020.

[144] D. Strickland and G. Mourou. Chirped pulse amplification. *Optics Communications*, 56:219–221, 1985.

[145] H. Kiriyama, A. S. Pirozhkov, M. Nishiuchi, Y. Fukuda, A. Sagisaka, A. Kon, Y. Miyasaka, K. Ogura, N. P. Dover, K. Kondo, et al. Petawatt femtosecond laser pulses from titanium-doped sapphire crystal. *Crystals*, 10(9):783, 2020.

[146] K. F. Wall and A. Sanchez. Titanium sapphire lasers. *Lincoln Laboratory Journal*, 3:3–15, 1989.

[147] T. Brabec, C. Spielmann, P. F. Curley, and F. Krausz. Kerr lens mode locking. *Optics Letters*, 17(18):1292–1294, 1992.

[148] D. E. Spence, P. N. Kean, and W. Sibbett. 60-fsec pulse generation from a self-mode-locked ti:sapphire laser. *Optics Letters*, 16(1):42–44, 1991.

[149] P. F. Moulton. Spectroscopic and laser characteristics of Ti:Al_2O_3. *Journal of the Optical Society of America B*, 3(1):125–133, 1986.

[150] W. R. Rapoport and C. P. Khattak. Titanium sapphire laser characteristics. *Applied Optics*, 27(13):2677–2684, 1988.

Appendix A

Chapter 5 & 6: Supplementary Data

Role of Phonon Activation in Metamaterial

To isolate the effect of the phonon mode on the metamaterial response, we perform systematic numerical simulations of the individual resonators (rod and SRR) as well as the coupled EIT configuration using CST Microwave Studio. The simulations are carried out under two distinct conditions: (i) with the phonon response deactivated, where the perovskite layer is treated as a passive dielectric medium, and (ii) with the phonon mode activated through the inclusion of a Lorentz oscillator centered around 1 THz. This approach allows us to clearly distinguish between purely dielectric effects and genuine phonon-mediated interactions.

In the absence of the phonon mode, the presence of the perovskite layer modifies the

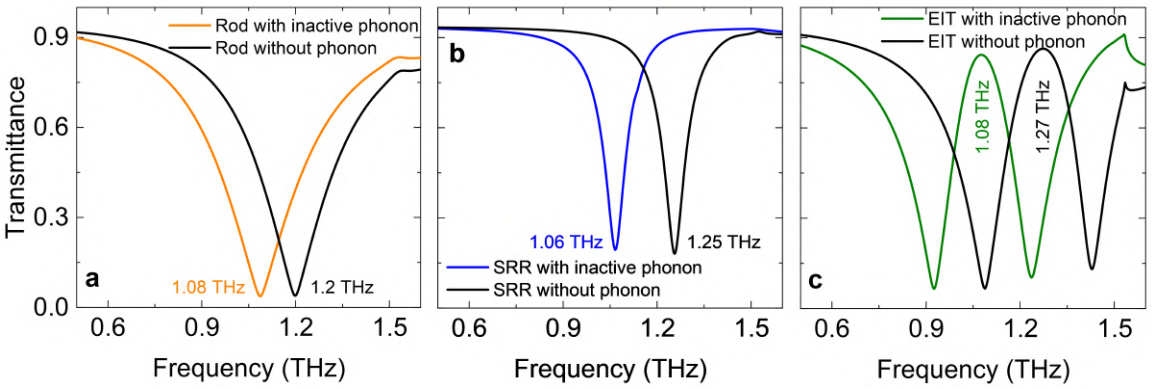

Figure A.1: Simulated transmittance spectra of **(a)** rod resonator, **(b)** split-ring resonator (SRR), and **(c)** the coupled EIT metamaterial system obtained using CST Microwave Studio, shown for two cases: with the phonon mode deactivated (passive dielectric response) and with the phonon mode activated at 1 THz. In the absence of phonon activity, the perovskite layer acts as a dielectric medium, leading to a redshift of the resonance frequencies due to an increase in the effective refractive index. Upon activation of the phonon mode, the spectral response deviates from this dielectric-shifted baseline, indicating the influence of phonon-mediated interactions. The effect is consistently observed across the individual resonators as well as the coupled EIT configuration.

local electromagnetic environment primarily through its dielectric permittivity. This leads to a systematic redshift of the resonance frequencies of both the rod and the SRR, consistent with the increase in the effective refractive index experienced by the resonators, as shown in Figure A.1. Such dielectric-induced shifts have been discussed in the Chapter 5, where even without phonon activation, the metamaterial resonances are observed to move to lower frequencies due to the altered cavity conditions. The effect is observed consistently across the individual resonators and the coupled EIT system. For the rod and SRR, the resonance dips shift when the phonon is inactive, reflecting the dielectric loading of the structure. In the coupled system, the EIT window also undergoes a corresponding shift, demonstrating that both the bright and dark modes are influenced by the same environmental modification. When the phonon is activated, the spectral response of the EIT system deviates further, indicating the onset of phonon-mediated interaction beyond simple refractive index effects.

Resonance Modes and Near-Field Distributions

To build a clearer physical picture of the bright-dark mode coupling mechanism underpinning the EIT-like response, we present the simulated transmittance spectra and the corresponding near-field electric field distributions for the individual and coupled resonator configurations. When the isolated rod resonator is excited by a y-polarised THz field, it exhibits a strong dipole resonance at $f_{\mathrm{rod}} = 1.2\,\mathrm{THz}$ with near-complete absorption, consistent with its role as the radiative bright mode, as shown in Figure A.2a, green curve. The isolated SRR pair, by contrast, is completely non-responsive under y-polarised excitation, as shown in Figure A.2a black curve, but displays a well-defined LC-type resonance at $f_{\mathrm{SRR}} = 1.25\,\mathrm{THz}$ when the incident field is oriented along the x-direction, as depicted in Figure A.2a blue curve. This polarisation selectivity confirms that the SRR acts as a dark mode under the experimental excitation geometry. The spatial profiles of the in-plane electric field magnitude $|E|$ at the respective resonance frequencies further reinforce this picture. At f_{rod}, the field is predominantly distributed along the length of the rod, exhibiting the characteristic dipolar pattern of a half-wave antenna, as shown in Figure A.2b. At f_{SRR}, the field energy is tightly localised at the capacitive gaps of the split rings, with negligible field at the rod, depicted in Figure A.2c.

When the rod and SRR pair are brought into proximity within the near-field coupling regime, the transmittance spectrum of the combined structure changes substantially. Two pronounced absorption dips appear at frequencies f_1 and f_2, creating a transparency peak at $f_{\mathrm{p}} = 1.27\,\mathrm{THz}$, as shown in Figure A.2d. These spectral features correspond to the lower dressed state, the EIT transparency peak, and the upper dressed state of the hybridised system, respectively. The near-field distributions at these three frequencies provide a direct view of the underlying mode hybridisation. At both f_1 and f_2, the electric field is simulta-

neously enhanced at the rod extremities and the SRR gaps (Figures A.2e and A.2g), indicating that both resonators contribute to the electromagnetic response at these frequencies. These are hallmarks of hybridised bright-dark superpositions. At the transparency peak f_p, however, the picture changes dramatically: the rod field is markedly suppressed while the SRR gap fields remain strongly excited, as displayed in Figure A.2f. This redistribution of near-field energy away from the rod and into the dark mode is the direct electromagnetic manifestation of destructive interference. The SRR near-field effectively cancels the rod's dipole radiation, channelling the stored energy into the subradiant mode and opening the transparency window.

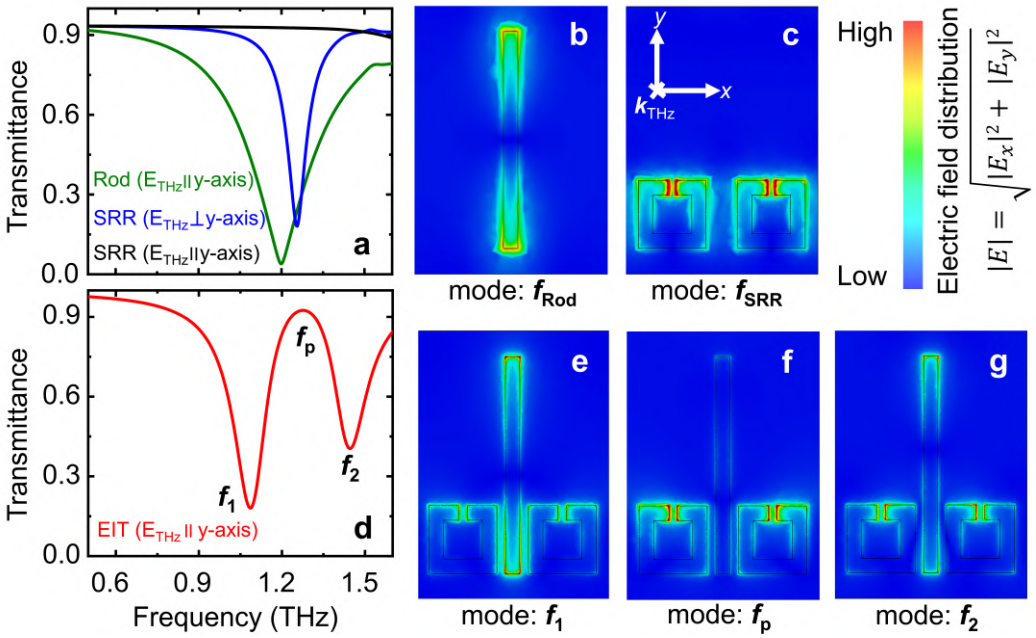

Figure A.2: Simulated transmission spectra and the corresponding near-field electric field distributions of the individual and EIT metamaterial resonators. **(a)** The transmittance spectra of the rod resonator (green curve), the split-ring resonator (blue and black curves). Here, the blue and black curves represent the SRR response when the incident E_{THz} is parallel and perpendicular to the $y-$ direction, respectively. The spatial distribution of the in-plane electric field magnitude $|E|$, highlighting the strong localization of the fields along **(b)** the rod, consistent with a radiative bright mode, and **(c)** the capacitive gaps. **(d)** Transmittance spectrum of the coupled EIT system. Here, the f_1, f_2, and f_p represent the lower-, upper-dressed states, and the EIT peak frequency of the system. **(e-g)** The near-field distribution corresponding to f_1, f_p, and f_2, respectively. Taken from Ref. [28]

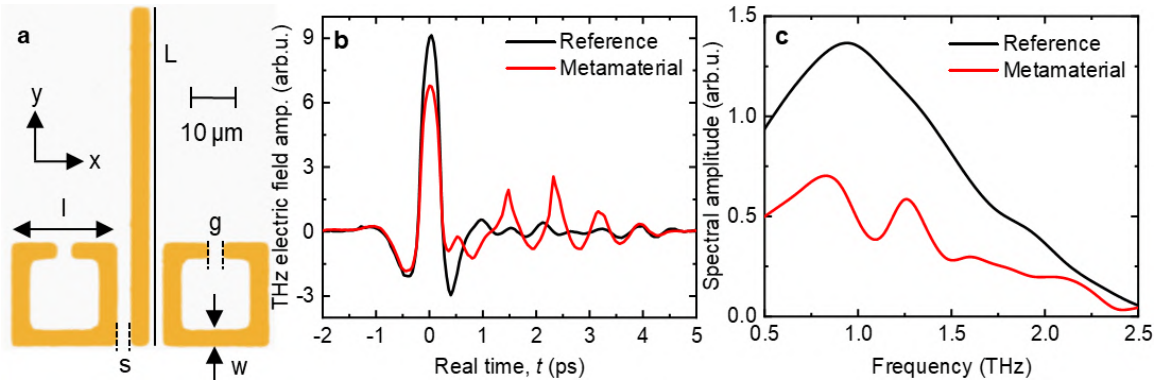

Figure A.3: **(a)** Optical microscopic image showing the unit cell of EIT meta-structure. The EIT-*like* metamaterial unit cell consists of a central rod resonator accompanied by a pair of split-ring resonators (SRRs) positioned symmetrically on either side of the rod. The geometric parameters of the metamaterial structure are as follows: $L = 75\,\mu$m, $l = 23.5\,\mu$m, $w = 5\,\mu$m, $g = 3\,\mu$m, $s = 3\,\mu$m with periodicity of 67 μm and 93 μm, along the x- and y-directions, respectively. The metamaterial structures are patterned in aluminium (Al) with a film thickness of 120 nm. **(b)** THz electric-field transients transmitted through the substrate and the metamaterial sample, and **(c)** the corresponding THz spectra. Taken from Ref. [28]

Metamaterial Linear THz Characterisation

Figure A.3a shows an optical microscope image of the fabricated EIT meta-structure unit cell. The unit cell consists of a central rod resonator positioned symmetrically by a pair of split-ring resonators (SRRs) on either side. The fabricated array is uniform over an area considerably larger than the THz beam waist at the sample plane, ensuring spatially homogeneous illumination during all spectroscopic measurements. The THz time-domain characterisation of the sample is presented alongside the optical microscope image. The electric-field transients transmitted through the bare z-cut quartz substrate and the metamaterial-on-substrate are shown in Figure A.3b, with the corresponding amplitude spectra obtained via Fourier transformation shown in Figure A.3c. The incident THz polarisation is oriented along the y-direction, i.e., parallel to the rod resonator. A pronounced suppression of the transmitted spectral amplitude is visible near the EIT window frequency.

Origin of Spectral Asymmetry in the ABB Photon-Echo Signal

A slight but reproducible spectral asymmetry is evident between the upper and lower dressed state peaks in the experimental ABB photon-echo signal. To determine the physical mechanisms responsible for this asymmetry, we performed a series of controlled numerical simulations in which individual model parameters were varied while keeping the rest fixed. In the first simulation, as shown in Figures A.4a–c, the bare mode detuning was set to $\Delta = 0$ with unequal damping rates ($\gamma_1 \neq \gamma_2$) and a pulse centre frequency of $f_0 = 1.0\,\mathrm{THz}$. Despite the detuning being zero, which implies that both dressed states should contain equal bright-mode character. In principle, this should lead to equal spectral weights. However, a pronounced asymmetry is observed, with the lower-frequency dressed state appearing considerably more intense. The origin of this asymmetry is spectral: the driving pulse, centred at 1.0 THz, has greater overlap with the lower dressed state and preferentially excites it, resulting in an intensity imbalance that is unrelated to any intrinsic asymmetry in the coupling. In the second simulation, as shown in Figures A.4d–f, the pulse centre was shifted to $f_0 = 1.2\,\mathrm{THz}$ to bring it into resonance with the bare bright mode, while maintaining $\Delta = 0$ and $\gamma_1 \neq \gamma_2$. The asymmetry is substantially reduced under these conditions, directly confirming that the unequal spectral excitation of the two dressed states in the first case was a consequence of the off-resonant pulse rather than any structural asymmetry in the system. In the third simulation, as depicted in Figures A.4g–i, both the detuning and the damping asymmetry were simultaneously removed ($\Delta = 0$, $\gamma_1 = \gamma_2, f_0 = 1.2\,\mathrm{THz}$). The two dressed state peaks now appear with nearly equal spectral amplitudes in both the diagonal and cross-diagonal cuts, confirming that the system is inherently symmetric when neither detuning nor differential damping is present.

Taken together, these simulations establish that the asymmetry observed in the experimental ABB photon-echo signal has two distinct physical origins. The first is the offset of the incident pulse centre frequency ($f_0 = 1.0\,\mathrm{THz}$) from the bright mode resonance at 1.20 THz, which causes the two dressed states to receive unequal spectral excitation. The second is a finite energy detuning of $\Delta = 0.05\,\mathrm{THz}$ between the bare bright and dark mode resonances of the fabricated structure, which breaks the symmetry of the dressed state mixing and causes the state with the larger bright-mode admixture to appear with greater spectral weight in the photon-echo response. The structural coupling g_s determines the separation between the dressed states but plays no role in setting their relative spectral intensities.

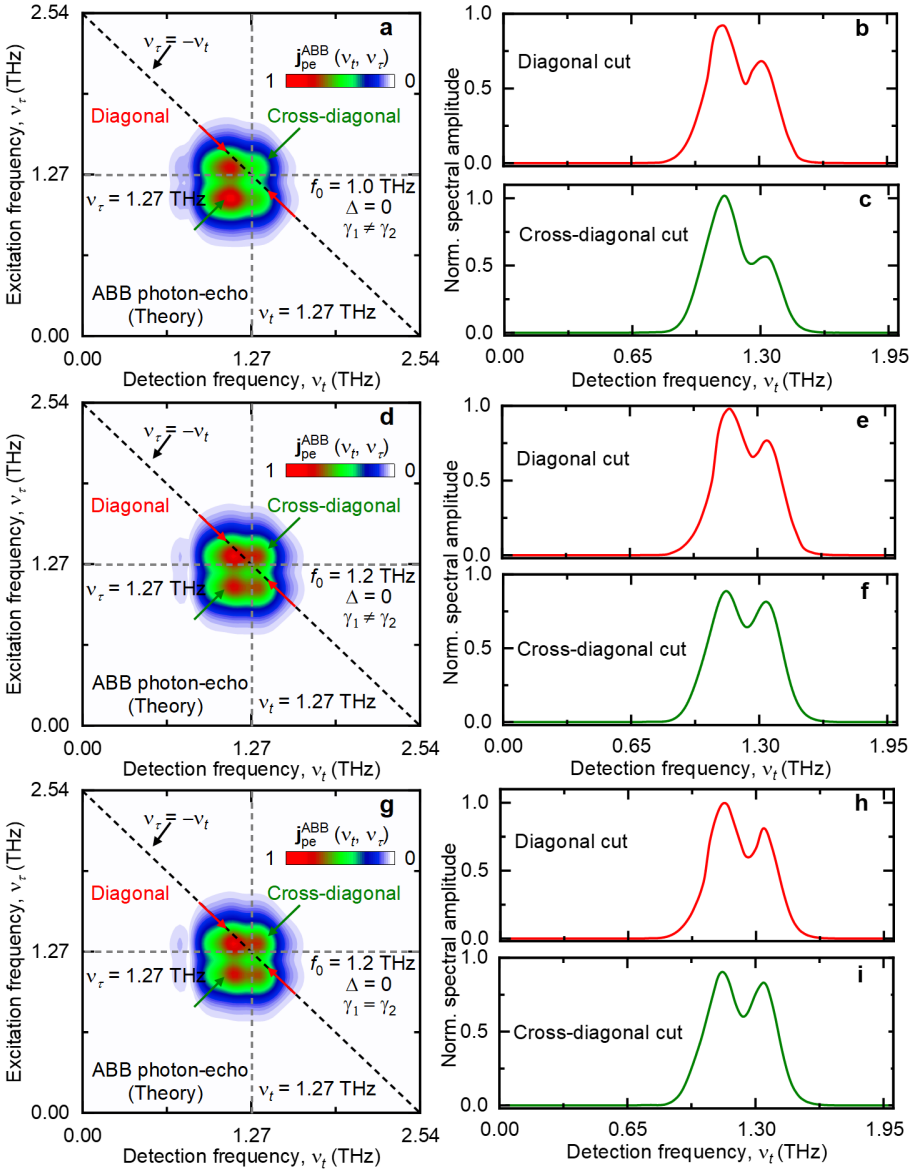

Figure A.4: Theoretical ABB photon-echo signal $\mathbf{j}_{\mathrm{pe}}^{\mathrm{ABB}}(\nu_t, \nu_\tau)$ under different model conditions. **(a-c)** Strong asymmetry, with $f_0 = 1.0\,\mathrm{THz}$, $\Delta = 0$, $\gamma_1 \neq \gamma_2$. **(d–f)** Reduced asymmetry, with $f_0 = 1.2\,\mathrm{THz}$, $\Delta = 0$, $\gamma_1 \neq \gamma_2$. **(g–i)** Nearly symmetric, with $f_0 = 1.2\,\mathrm{THz}$, $\Delta = 0$, $\gamma_1 = \gamma_2$. Taken from Ref. [28]

Robustness of the Density Matrix Model Parameters

To verify that the extracted dynamical parameters are not critically sensitive to the precise value of the structural coupling strength g_s, we performed additional simulations in which

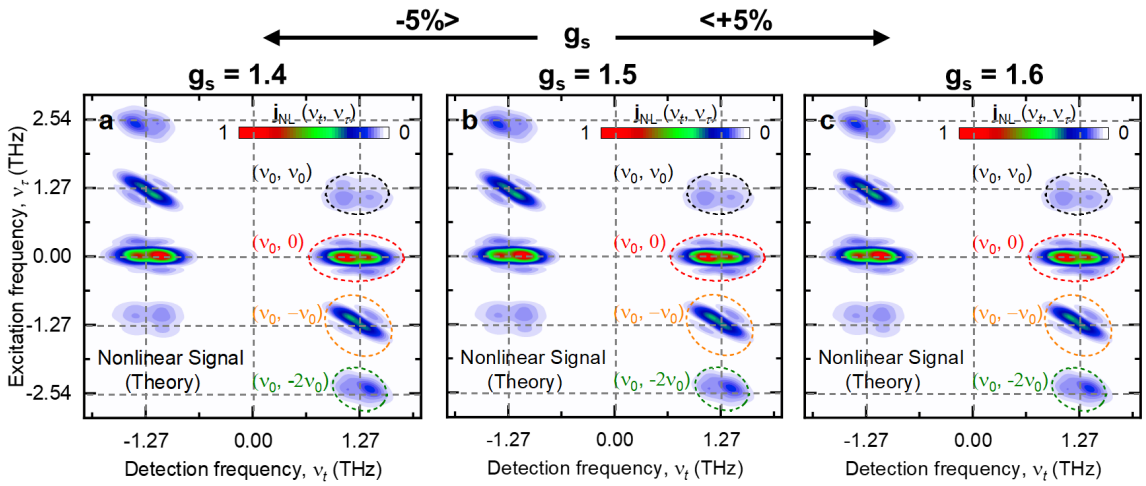

Figure A.5: Theoretical 2D nonlinear frequency maps $\mathbf{j}_{\mathrm{NL}}(\nu_t, \nu_\tau)$ simulated for three values of the structural coupling strength: **(a)** $g_s = 0.14\,\mathrm{rad\,ps^{-1}}$ (-5%), **(b)** $g_s = 0.15\,\mathrm{rad\,ps^{-1}}$ (original), and **(c)** $g_s = 0.16\,\mathrm{rad\,ps^{-1}}$ $(+5\%)$, with all other parameters kept fixed. The positions and relative intensities of all four nonlinear signals pump-probe at $(\nu_0, 0)$ and $(\nu_0, -\nu_0)$, and photon-echo at (ν_0, ν_0) and $(\nu_0, -2\nu_0)$ - remain essentially unchanged across the three cases, confirming the robustness of the 2D spectral features against small variations in g_s. Taken from Ref. [28]

g_s was varied by $\pm 5\%$ around its optimal value of $2\pi \times 0.15\,\mathrm{rad\,ps^{-1}}$, with all other Lindblad parameters held fixed. Figure A.5 shows the resulting 2D nonlinear frequency maps for $g_s = 2\pi \times 0.14$, 0.15, and $0.16\,\mathrm{rad\,ps^{-1}}$. Across all three cases, the positions and relative intensities of the four nonlinear signals such as the pump-probe features at $(\nu_0, 0)$ and $(\nu_0, -\nu_0)$, and the photon-echo features at (ν_0, ν_0) and $(\nu_0, -2\nu_0)$, remain essentially unchanged. This insensitivity of the spectral peak positions to small changes in g_s confirms that the 2D frequency map is robustly constrained by the experimental data and does not depend critically on fine-tuning of the coupling parameter. Beyond $\pm 5\%$ variation, the nonlinear signals begin to show meaningful deviations from the experimental observations.

The extracted relaxation and coherence timescales are equally stable within experimental uncertainty across this parameter range. The relaxation times T_1 obtained for the three values of g_s span $1.74 - 1.8$ ps, and the coherence times T_2 lie between 1.06 and 1.1 ps, both well within the respective fitting uncertainties. There is a natural decoupling between the spectral peak structure and the temporal decay dynamics. The spectral peaks are governed primarily by g_s, while the decay envelopes are controlled by γ_1, γ_2, and γ_φ. This separation demonstrates that all model parameters are independently and robustly constrained by the data.

It is worth noting that the metamaterial structures were fabricated using a Heidelberg

maskless laser lithography system, which achieves a dimensional resolution on the order of $\sim 1\ \mu$m. At this resolution, the SRR gap size and the rod–SRR separation are the geometric parameters most directly linked to g_s. These features may carry small fabrication-induced variations across the array. Such variations can produce slight shifts in resonance frequency and modest changes in coupling strength. However, because the EIT transparency window arises from the interference between the coupled modes rather than from precise geometric matching, the overall EIT character is preserved even under realistic fabrication tolerances. The coherence time T_2 is somewhat more susceptible to fabrication-induced disorder, since structural inhomogeneities introduce additional dephasing pathways and can broaden the resonance linewidth. The relaxation time T_1, being determined primarily by radiative and ohmic losses, is comparatively less sensitive to such variations. The qualitative conclusions drawn from the density matrix model are therefore expected to remain robust across the sample.

Model Parameters

The parameters used in the time-resolved density matrix model are summarized in Table A.1. These values are chosen based on the experimentally observed resonance frequencies and decay dynamics of the system. They provide a consistent framework for capturing both the coherent coupling and dissipative processes in the THz regime.

Table A.1: Parameters used in the time-resolved density matrix model.

Symbol	**Value**	**Description**
Hamiltonian parameters		
$E_0,\ E_1,\ E_2$	$0.0,\ 1.20,\ 1.25$ THz	Bare energy levels
g_s	$2\pi \times 0.15$ rad ps^{-1}	Structural coupling strength
Lindblad decay rates		
γ_1	0.15 ps^{-1}	Decay $\|1\rangle \rightarrow \|0\rangle$
γ_2	0.05 ps^{-1}	Decay $\|2\rangle \rightarrow \|1\rangle$
γ_φ	0.8 ps^{-1}	Pure dephasing rate
Extracted timescales		
$T_1,\ T_2,\ T_\varphi$	$1.96,\ 1.0,\ 1.34$ ps	Relaxation, coherence, and dephasing times
THz pulse parameters		
f_0	1.0 THz	Central frequency
σ	0.35 ps	Pulse width
γ	1.6 ps	Chirp parameter
$\|\mathbf{E}_\mathrm{A}\|,\ \|\mathbf{E}_\mathrm{B}\|$	$20,\ 40$ kV cm^{-1}	THz field amplitudes

Appendix B

Astrella Ti:Sapphire Laser System

The ultrafast laser system, as shown in Figure B.1, used in this thesis, is a Coherent Astrella regenerative amplifier based on a Ti:Sapphire gain medium. The system consists of four main subsystems. The seed oscillator is a Vitara Ti:Sapphire cavity pumped by a Verdi-G continuous wave diode-pumped solid-state laser operating at 532 nm with a specified output power of 5 W. In our system, the Verdi-G operates at 4.7 W. The Vitara produces ultrashort seed pulses at 800 nm with a pulse duration of approximately 20 fs, a repetition rate of 80 MHz, and a pulse energy of 7.6 nJ at 610 mW average power. These seed pulses are stretched in time by a grating stretcher before entering the regenerative amplifier cavity. The amplifier is pumped by a Revolution Nd:YLF laser producing 532 nm pulses of

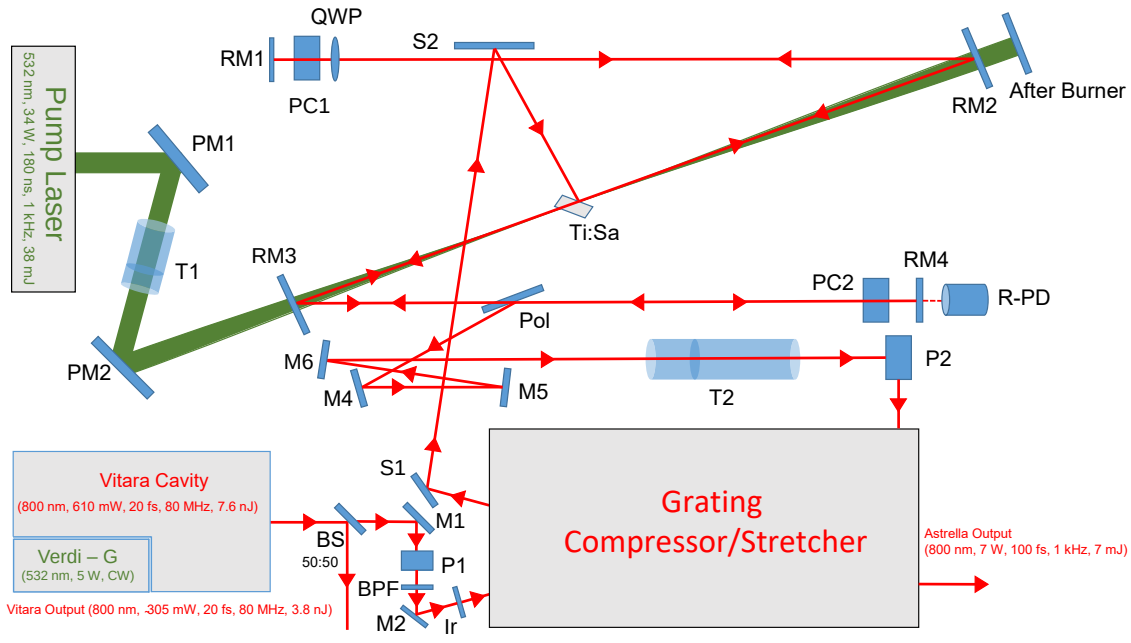

Figure B.1: Schematic of the Coherent Astrella ultrafast laser system: M1-6 (mirrors); RM1-4 (regen amplifier mirrors); S1-2 (seed mirrors); PM1-2 (pump mirrors); T1-2 (telescope); PC1-2 (pockels cell); QWP (quarter wave plate); Pol (polarizer); R-PD (regen photo-diode); BS (beam splitter); BPF (bandpass filter); Ir (iris); P1-2 (periscope); Ti:Sa (titanium-sapphire).

approximately 180 ns duration at a repetition rate of 1 kHz and a specified average power of 38 W. After amplification and recompression in the grating compressor, the Astrella delivers pulses at 800 nm with a pulse duration of 100 fs, a repetition rate of 1 kHz, a specified pulse energy of 7 mJ, and a specified average output power of 7 W.

Working Principle of the Astrella System

The Astrella operates on the principle of chirped-pulse amplification (CPA) [144], a technique developed by Strickland and Mourou that makes it possible to amplify ultrashort pulses to high energies without destroying the gain medium or the optical components along the beam path. The core problem CPA solves is straightforward. A 100 fs pulse with millijoule-level energy carries a peak power in the tens of gigawatts (GW). If such a pulse were amplified directly inside a laser crystal, the intensity would exceed the damage threshold of any known optical material. CPA resolves this by separating the amplification process into three distinct stages: the pulse is first stretched in time by several orders of magnitude to reduce its peak power to safe levels, then amplified to the target energy, and finally recompressed back to its original duration. The individual components of the CPA system, namely the oscillator (Vitara), pump lasers, stretcher, amplifier, and compressor, are discussed in detail in the following subsections, with emphasis on their respective roles in achieving high energy ultrashort pulse generation. The overall layout and working principle of the chirped pulse amplification scheme used in the Astrella system are illustrated in Figure B.2.

As shown in Figure B.2, an ultrashort pulse generated by the Ti:Sapphire oscillator is first directed into a grating-based stretcher, where different spectral components experience different optical path lengths, resulting in a temporally stretched, chirped pulse with reduced peak power. This stretched pulse is subsequently amplified in the gain medium, where its energy is increased while the chirped temporal profile is preserved. The amplified chirped pulse is then sent to a grating-based compressor, which introduces dispersion of opposite sign and recombines the spectral components in time. As a result, the pulse is restored to its original short duration while retaining the amplified energy, thereby producing a high peak power output.

Ti:Sapphire as a gain medium. The gain medium of both the oscillator (Vitara) and the regenerative amplifier is a Ti:Sapphire crystal. When titanium ions in the 3^+ oxidation state are substituted into a sapphire (Al_2O_3) host lattice, the result is a vibronic laser medium whose gain bandwidth spans roughly 650 to 1100 nm, with peak gain near 800 nm [145]. This exceptionally broad bandwidth arises because the optical transition of the Ti^{3+} ion is strongly coupled to the phonon modes of the surrounding lattice. The electronic transition does not occur at a single sharp frequency but is broadened across a wide range of vibrational

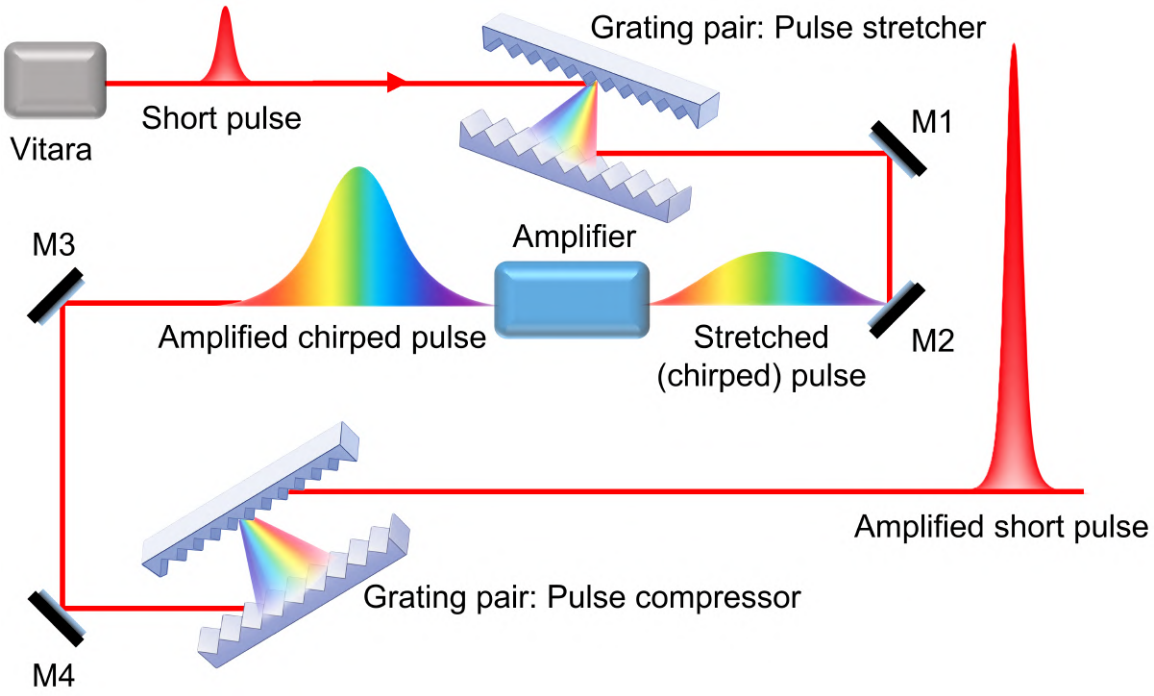

Figure B.2: Schematic representation of chirped pulse amplification. An ultrashort pulse generated by the Ti:Sapphire oscillator (Vitara) is temporally stretched using a grating-based stretcher, where different spectral components acquire different optical path lengths, resulting in a chirped pulse with reduced peak power. The stretched pulse is then amplified in the gain medium, increasing its energy while maintaining the chirped temporal profile. Finally, a grating-based compressor introduces dispersion of opposite sign, recombining the spectral components in time and restoring the pulse to its original short duration, thereby producing an amplified high-peak-power pulse. The rainbow color representation in the stretcher and compressor stages is used for illustrative purposes to indicate the spectral bandwidth and dispersion of different frequency components; in practice, the laser operates in the near-infrared region and the beam does not appear as visible rainbow light.

sublevels [146]. It is this bandwidth that supports the generation and amplification of pulses as short as a few tens of femtoseconds. Beyond its spectral properties, Ti:Sapphire has a relatively large stimulated emission cross-section, high thermal conductivity, and good mechanical hardness, allowing reliable operation over a wide range of repetition rates and pulse energies at room temperature. These combined properties make Ti:Sapphire the most widely used gain medium for ultrafast laser systems based on chirped pulse amplification.

The Verdi-G oscillator pump. The Ti:Sapphire oscillator (Vitara) in the Astrella system is optically pumped by a continuous wave green laser source provided by the Verdi-G laser. The Verdi-G has a specified output of 5 W at 532 nm, and in our system it operates at 4.7 W, which is used to excite the Ti:Sapphire gain medium, as shown in Figure B.1.

The Verdi-G operates based on optically pumped semiconductor laser technology, in which semiconductor quantum well structures are optically excited by high power laser diodes to generate intracavity infrared radiation. This radiation is subsequently converted to green output through second harmonic generation in a nonlinear crystal. The resulting continuous wave beam is directed into the Ti:Sapphire crystal, where it excites Ti^{3+} ions and establishes the population inversion required for laser operation. The high beam quality and low intensity noise of the pump source are essential for stable oscillator performance and consistent femtosecond pulse generation.

The Vitara oscillator and Kerr-lens mode-locking. The Vitara oscillator produces ultrashort seed pulses through Kerr-lens mode-locking (KLM) [147,148]. The optical Kerr effect causes the refractive index of the Ti:Sapphire crystal to increase slightly in proportion to the local intensity of the light passing through it. For a beam with a Gaussian spatial profile, this creates a weak but real focusing lens whose focal length depends on the instantaneous intensity. When the intracavity power is high, as it is during a short pulse, this nonlinear lens focuses the beam and improves its spatial overlap with the pump region. A continuous wave beam, having lower peak intensity, is focused less efficiently and experiences greater loss at the intracavity aperture. The cavity therefore self-selects for pulsed operation: once the system is briefly perturbed into a pulsed state, the nonlinear lens stabilises it there. The resulting mode-locked output is a coherent superposition of all the resonant longitudinal modes of the cavity, all oscillating with the same phase. This produces a train of ultrashort pulses separated in time by the cavity round-trip period, corresponding to a repetition rate of 80 MHz. Each pulse has a duration of approximately 20 fs and carries an energy of 7.6 nJ at an average power of 610 mW, as shown in Figure B.1.

Pulse selection from the oscillator train. The mode-locked Ti:Sapphire oscillator (Vitara) generates a continuous train of ultrashort pulses at a repetition rate of approximately 80 MHz. However, as indicated in the system schematic, the downstream regenerative amplifier operates at a significantly lower repetition rate of 1 kHz. Therefore, it is necessary to reduce the repetition rate of the oscillator output by selecting only a single pulse from every 80,000 pulses. As shown in the Figure B.1, the pulse selection stage is implemented using an electro-optic pulse picker consisting of two Pockels cells (PC1 and PC2) in conjunction with polarization optics, including a polarizer (Pol) and waveplate elements. The oscillator output is first incident on the polarization control stage, after which it passes through the first Pockels cell (PC1). In the absence of an applied voltage, the polarization state of the pulses remains unchanged, and they are rejected by the downstream polarizer. When a high-voltage trigger signal is applied to PC1, synchronized with the system timing electronics, the induced birefringence rotates the polarization of a selected pulse, allowing it to pass through the polarizer and continue along the optical path. The second Pockels cell (PC2) further refines the temporal gating and ensures precise selection and routing of the pulse toward the stretcher and regenerative amplifier chain. This two-stage configuration

improves the extinction ratio and enhances the stability of the pulse picking process. The timing of the Pockels cells is controlled by an external delay generator, ensuring that the selected pulse arrives at the amplifier at the correct time relative to the pump pulse.

The pulse stretcher. The selected seed pulse enters a grating-based pulse stretcher prior to amplification. In this stage, diffraction gratings introduce angular dispersion such that different spectral components of the pulse traverse different optical path lengths. As a result, the spectral components become temporally separated, producing a positively chirped pulse in which the instantaneous frequency varies monotonically with time. The pulse duration increases from approximately 100 fs to several hundred picoseconds, leading to a reduction in peak power by several orders of magnitude. Although the total pulse energy is approximately conserved, it is now distributed over a much longer time, ensuring that the peak intensity remains well below the damage threshold of the Ti:Sapphire crystal and other optical components during amplification.

The regenerative amplifier. The stretched seed pulse is injected into a regenerative amplifier cavity, where it circulates multiple times through a pumped Ti:Sapphire gain medium. During each round trip, the pulse extracts energy from the population inversion via stimulated emission, leading to a gradual increase in pulse energy. The detailed processes of pulse injection, amplification, and ejection are described in the following section.

The after-burner. After the seed pulse is injected into the regenerative amplifier cavity and begins circulating through the Ti:Sapphire gain medium, a portion of the green pump light passes through the crystal without being absorbed and leaks out from the back. The afterburner is a mirror-lens assembly positioned behind the crystal that captures this transmitted green light, reflects it, and refocuses it back into the Ti:Sapphire gain medium. By recycling the otherwise wasted pump photons, the afterburner increases the effective population inversion available within the crystal during amplification. This leads to a higher stored energy and, consequently, a greater pulse energy at the output. The afterburner does not involve a separate gain medium or an additional amplification pass of the seed pulse; it acts solely on the pump beam, improving the efficiency with which the green pump energy is converted into population inversion in the primary crystal.

The pulse compressor. Following amplification, the temporally stretched pulse is directed into a grating-based compressor, which is designed to compensate the dispersion introduced by the stretcher. The compressor employs diffraction gratings arranged to introduce negative group delay dispersion, thereby reversing the positive chirp acquired during stretching. This process realigns the spectral components in time and recompresses the pulse toward its transform-limited duration. In practice, precise adjustment of the grating separation and incidence angle is required to optimize the compensation of both second-order and higher-order dispersion terms. When properly aligned, the system produces pulses of approximately 100 fs duration with an energy of 7.5 mJ and an average power of

7.5 W at a repetition rate of 1 kHz. The corresponding peak power reaches approximately 75 GW, enabling efficient nonlinear processes such as terahertz generation via optical rectification.

Regenerative Amplification

The regenerative amplifier provides the primary energy gain in the system, amplifying the stretched seed pulse from the nanojoule level to the millijoule level, corresponding to an overall gain on the order of 10^6. This is achieved by trapping the pulse within a resonant cavity, allowing it to pass multiple times through the pumped Ti:Sapphire gain medium and extract energy during each round trip.

The Revolution pump laser and population inversion. Before the arrival of the seed pulse, the Ti:Sapphire crystal inside the regenerative amplifier must be prepared with a significant population inversion. This is achieved using the Revolution laser, a Q-switched solid-state laser based on a neodymium-doped yttrium lithium fluoride (Nd:YLF) gain medium. The gain medium is optically pumped by diode bars operating near 806 nm. During Q-switched operation, the intracavity losses are initially kept high, preventing lasing while the population inversion builds up. As a result, the inversion reaches a level significantly higher than that achievable under steady-state lasing conditions. When the cavity losses are rapidly reduced, the stored energy is released in the form of a short, intense pulse. In the Astrella system, this process generates pulses at 532 nm through second harmonic generation, with a pulse duration on the order of 180 ns and a repetition rate of 1 kHz. Each pulse carries an energy of approximately 38 mJ, corresponding to an average power of about 38 W. These pump pulses are synchronised with the system timing electronics to arrive at the Ti:Sapphire crystal just before the injection of the seed pulse, ensuring optimal population inversion for amplification.

The 532 nm pump photons are absorbed by the Ti:Sapphire crystal, exciting Ti^{3+} ions from the ground state to higher-lying vibronic levels of the excited electronic manifold. This excitation is followed by rapid phonon-assisted relaxation within the excited manifold, occurring on a picosecond timescale, which brings the population down to the lowest vibrational levels of the excited state. The ions then accumulate in this state for the fluorescence lifetime of approximately 3.2 μs [149, 150]. During this time interval, a substantial population inversion is established between the excited state and the lower vibronic levels of the ground state manifold. When a seed photon at approximately 800 nm propagates through the inverted medium, it stimulates the emission of additional photons that are identical in frequency, phase, and direction, leading to optical amplification. The magnitude of the single-pass gain depends on several factors, including the deposited pump energy, the length of the gain medium, and the spatial overlap between the pump and seed beams.

The cavity architecture. The regenerative amplifier is configured as a linear optical resonator containing the Ti:Sapphire gain crystal, a thin-film polarizer (TFP), and a Pockels cell, along with cavity mirrors that define the optical path. The TFP is designed to transmit one linear polarization while reflecting the orthogonal polarization. In the absence of an applied voltage to the Pockels cell, the polarization of an incoming pulse remains unchanged, and the pulse is transmitted through the TFP without being coupled into the resonator. Under this condition, the cavity does not trap the pulse and remains effectively open. Controlled manipulation of the polarization state using the Pockels cell allows selective injection, trapping, and ejection of the pulse within the cavity. This polarization-based switching forms the basis of regenerative amplification.

Injection of the seed pulse. When the stretched seed pulse arrives at the regenerative amplifier, a high-voltage signal is applied to the Pockels cell in synchronisation with the system timing electronics (SDG in the laser system). The Pockels cell operates based on the linear electro-optic effect in birefringent crystals such as potassium dideuterium phosphate (KD*P) or rubidium titanyl phosphate (RTP). The applied electric field modifies the refractive indices along the principal axes of the crystal, introducing a phase delay between orthogonal polarization components of the optical field. By selecting an appropriate voltage, the Pockels cell acts effectively as a waveplate, such that after a double pass through the crystal the polarization of the seed pulse is rotated by 90° . This rotation changes the interaction of the pulse with the thin-film polarizer, causing it to be reflected into the resonator rather than transmitted. In this way, the seed pulse is coupled into the cavity and begins circulating within it.

Round-trip gain and saturation. Once the seed pulse is injected into the regenerative amplifier cavity, it becomes trapped and circulates repeatedly through the Ti:Sapphire gain medium. During each round trip, the pulse passes through the crystal twice and extracts energy from the population inversion via stimulated emission. In the initial stage of amplification, when the inversion is largely undepleted, the pulse energy increases approximately exponentially with the number of round trips. This regime is commonly referred to as the small-signal gain regime, where the gain per pass remains nearly constant. As the pulse energy increases, the interaction with the gain medium becomes progressively stronger, and a significant fraction of the stored inversion is depleted during each pass. Consequently, the gain per round trip decreases, and the amplification gradually transitions into the saturation regime. At this stage, the net gain approaches unity, meaning that further round trips do not result in a substantial increase in pulse energy. The pulse energy therefore approaches the maximum extractable energy determined by the stored inversion and the cavity losses. In typical operation of Ti:Sapphire regenerative amplifiers such as the Astrella system, saturation is reached after a limited number of round trips, generally on the order of 10 to 20. The entire amplification process takes place within a few hundred nanoseconds, which is well within the upper-state lifetime of Ti:Sapphire. This ensures efficient extraction of

the stored energy before significant spontaneous decay of the population inversion can occur [149, 150].

Ejection of the amplified pulse. After the pulse energy has reached saturation, PC2 is switched on by the timing electronics. The applied voltage rotates the polarization of the circulating pulse to vertical. When this vertically polarized pulse reaches the thin-film polarizer, it is reflected out of the cavity rather than transmitted through it, and exits as the amplified output. The timing of injection and ejection is controlled by programmable delay parameters in the SDG, which determine the number of round trips the pulse undergoes within the cavity. These timing parameters are critical for maintaining stable operation, as they directly influence the output pulse energy, efficiency of energy extraction, and overall pulse quality.

Why stretching is essential. The necessity of pulse stretching in chirped pulse amplification can be understood by considering the peak power of the amplified pulse. The final output of the Astrella system corresponds to an energy of approximately 7.5 mJ compressed to a duration of about 100 fs, resulting in a peak power on the order of 75 GW. If such a pulse were directly amplified without temporal stretching, the resulting intensity within the regenerative amplifier would far exceed the optical damage threshold of the Ti:Sapphire crystal and other intracavity components. By stretching the pulse to a duration of several hundred picoseconds prior to amplification, the peak power is reduced by several orders of magnitude, while the total energy remains approximately constant. This reduction in peak intensity ensures safe operation of the amplifier and prevents optical damage. After amplification, the pulse is recompressed to its original duration, restoring the high peak power required for subsequent nonlinear optical applications.

(A) Turning ON Astrella from START

The switch-on and switch-off procedures described below must be followed in the precise sequence given. Departing from the prescribed order risks damage to the Pockels cell crystals, the Ti:Sapphire gain medium, or the pump laser. All operating parameters must be recorded in the laser logbook at the end of every session.

1. Switch ON the chiller power switch, then the switch behind the unit, and then press the start button on the front panel.
2. Wait for 2 – 3 minutes and check the temperature (20 °C) and water flow (15 - 16 LPM).
3. Start the laptop.

4. Start the Revolution using the power switch and then switch ON from the front panel.
5. Start the Revolution software.
6. Go to Settings and click the “Factory” tab.
7. Click the “toggle switch” down to set the LBO temperature to 325.9 °F and verify on the front panel of Revolution that it is effective.
8. Exit and close the Revolution software.
9. Switch OFF the Revolution from the front panel (keep the power **ON**).
10. Wait for 30 – 45 minutes for the temperature to reach the set value.
11. Finally, follow the steps in chronological order as in procedure (**B**) to switch ON.

(B) Switching ON the Astrella: Daily Procedure

1. Before switching on any component, verify the following pre-start conditions:
   (a) The chiller is running and the distilled water temperature is approximately 20 °C.
   (b) The LBO temperature reads 325.9 °F.
   (c) The chiller flow rate is between 15 and 16 LPM (liter per minute).
2. Switch ON the Vitara Power and the Vitara Control using the main switches and/or the back switch.
3. Turn ON the laser laptop.
4. Turn ON the USB Hub.
5. Switch ON the Oscilloscope.
6. Press the REMOTE button in the software.
7. Open the Vitara software on the computer.
8. Press the Vitara SWITCH to ON in the front panel.
9. Press the Diode ON button in the software.
10. Turn the Vitara KEY to ON from the front panel.

11. Switch ON the SDG unit and verify the front panel indicators:
    (a) Press the RESET button on the front panel of the SDG.
    (b) A continuous RED light indicates ERROR. A blinking RED light indicates NO ERROR. Proceed only if the indicator is blinking.
12. Press the SDG delay buttons ON [ENABLE] in the front panel.
13. Turn the Revolution KEY to ON in the front panel.
14. Enable the SDG delay channels in the following order and record the values in the logbook:
    (a) Enable in order: Delay 3 – Delay 2 – Delay 1.
    (b) Verify and record the following delay values:
        i. D1: 5018.50 ns
        ii. D2: 5132.75 ns
        iii. D3: 5187.50 ns
15. Remove the beam block CAP from the Astrella output port and place the power meter head directly in front of the output.
16. Switch ON the external Compressor/Stretcher control unit.
17. Open the Revolution software on the laptop.
18. Press and hold the “RUN” button until you hear the “BEEP” sound. Release the button immediately upon hearing the sound. The current should read 21.2 A. Monitor the software display.
    (a) If a warning dialog appears, click “OK” to dismiss it.
    (b) Confirm that the Q-switch mode is set to “External” by clicking “Evolution Settings” and verifying the selection.
19. Monitor the REGEN build-up on the oscilloscope until the signal is stable.
20. Monitor the power meter. The Revolution output power reading should stabilise at approximately 33.65 W.
21. Monitor the Astrella output power at the power meter head. The reading should be approximately 7 W.
22. Check the Vitara software for the following conditions. All indicators must be GREEN before the system is considered ready:

(a) Lasing, Mode-locked, and Power track indicators are all GREEN.

(b) Wait for stable mode-locking to establish before proceeding.

(c) Confirm that the Pump power displayed in the power supply reads 4.74 W.

(d) Confirm that the Vitara output power is approximately 605 mW.

23. Record the following parameters in the laser logbook and the Excel tracking file before beginning any experiment: Vitara pump power, Revolution power output, D1, D2, D3 delay values, and Astrella output power.

(C) Switching OFF the Astrella: Daily Procedure

1. Click the "STOP" button in the Revolution software.
2. Exit and close the Revolution software. Close it only once.
3. Turn the Revolution KEY to OFF in the front panel.
4. In the SDG front panel, disable the delay channels in the following order:
   - Delay 1 – Delay 2 – Delay 3.
5. Switch OFF the SDG unit using the power switch either on the rear of the unit or on the front panel. **REMEMBER: Do NOT switch off the Revolution power switch at any point during this procedure. Do NOT reverse the delay disable order.**
6. In the Vitara software, press "Diode" OFF.
7. Turn the "Remote" switch OFF in the front panel of the Vitara unit.
8. Turn the "Key" OFF in the front panel of the Vitara unit.
9. Exit the Vitara software.
10. Press the "STOP" button in the Revolution software.
11. Switch OFF the Vitara Control and Vitara Power units by switching off the power points.
12. Switch OFF the external Stretcher/Compressor control unit.
13. Shut down the laptop.
14. Switch OFF the power meter.

15. Place the beam block CAP back over the Astrella output port.
16. Switch OFF the USB Hub. **REMEMBER: Do NOT switch off the chiller power switch. The chiller must remain running.**
17. Switch OFF the Oscilloscope.
18. Keep the chiller running and verify the coolant temperature is stable.
19. Leave the Revolution power supply in standby mode. Do not switch it off.

(D) Shutting Down Astrella Completely

After following all the steps in the chronological order as in (**C**), follow the following procedure:

1. Switch ON the Revolution from the front panel (NOT the "KEY"!).
2. Start the Revolution software.
3. Go to Revolution Settings and click the "Factory" tab.
4. Click the "toggle switch" up to set the LBO temperature to 75 °F and verify on the front panel that it is effective.
5. Exit and close the software.
6. In the meantime, you can shut down the laptop.
7. Switch OFF the Revolution from the front panel (BUT keep the power ON).
8. Wait for 30 – 45 minutes for the temperature to reach 75 °F. Once reached, you can switch OFF the Revolution completely using the power switch.
9. Switch OFF the chiller: first from the front panel, then the switch behind, and finally the main power switch.

Notes on Safe Operation

The step sequences in both procedures are strictly prescribed and must not be modified. The most critical requirement in the switch-on procedure is the order in which the SDG delay channels are enabled: Delay 3 must be enabled first, followed by Delay 2, and then Delay 1. On shutdown, this order must be exactly reversed. The reason for this is that the delay channels control the timing of the Pockels cell switching pulses relative to the pump laser pulse. Enabling or disabling the channels out of order can expose the Pockels cell crystals to high-voltage switching events outside the safe timing window, which causes permanent damage to the crystals. Replacing Pockels cell crystals is an expensive and time-consuming process that requires realignment of the full regenerative amplifier cavity.

The Revolution power switch must never be turned off during the daily shutdown. The unit is designed to remain in standby between sessions, and switching off the mains power disrupts the thermal equilibrium of the Nd:YLF, which takes several hours to restabilise. The chiller must remain running at all times while the laser is on and must not be switched off until the Ti:Sapphire crystal and the pump optics have returned to room temperature. All numerical parameters listed in Step 22 of the switch-on procedure must be recorded in the laser logbook at every session. Systematic logging is the most reliable way to detect gradual performance degradation before it affects experimental results.

Appendix C

Laser Chiller Cleaning Procedure

The Ti:Sapphire laser system is water-cooled by a recirculating chiller unit. Over time, biological growth and particulate contamination accumulate within the chiller tank and internal tubing. This reduces cooling efficiency, raises the distilled water temperature, and risks thermal damage to the laser head. Periodic cleaning of the chiller with an alkaline detergent solution, followed by thorough rinsing and refilling with fresh distilled water, is therefore essential for maintaining stable laser performance. The procedure below should be carried out whenever visible contamination, discolouration, or foaming is observed in the distilled water, or as part of scheduled preventive maintenance.

Materials Required

- Distilled water (a minimum of 100 litres should be available to ensure adequate rinsing)
- Alconox laboratory detergent powder (70 g per cleaning cycle)
- Optishield Plus coolant additive
- One replacement chiller filter
- Clean containers for preparing and mixing the detergent solution

Procedure

1. Prepare the cleaning solution by dissolving 70 g of Alconox detergent powder in 7 litres of distilled water. Stir continuously until all powder is completely dissolved and no particles remain suspended in the solution. Do not proceed if undissolved particles are present.
2. Drain the chiller tank completely.

3. Fill the chiller tank with the Alconox solution prepared in Step 1. Set the chiller thermostat to 26 °C and start the chiller unit.
4. Allow the chiller to run continuously for approximately 12 hours. This circulates the hot detergent solution through the full internal tubing circuit and dissolves accumulated biological and particulate deposits.
5. Drain the chiller tank completely.
6. Fill the tank with fresh distilled water and run the chiller for 10 minutes to flush detergent residue from the circuit.
7. Drain the tank completely. Repeat Steps 6 and 7 for a total of 12 to 15 cycles, until the drained water runs completely clear with no visible foam. Thorough rinsing at this stage is critical. Detergent residue remaining in the circuit will react with the Optishield additive and may promote corrosion of the aluminium laser head components.
8. Replace the chiller filter with a new unit.
9. Fill the chiller tank with fresh distilled water and add the Optishield as specified by the manufacturer.
10. Set the chiller thermostat to 20 °C and run the chiller for 3 hours to allow the distilled water with Optishield mixture to fully circulate and stabilise throughout the circuit.
11. After 3 hours, check the distilled water flow rate and verify that the flow meter output is within the normal operating range specified by the chiller manufacturer. Record the flow reading in the laser maintenance logbook.

Notes

The 12 to 15 rinse cycles specified in Step 7 are a minimum guideline. The criterion for stopping is visual: the drained water must be clear and completely free of foam, regardless of how many cycles this requires. If foam persists after 15 cycles, the likely causes are either an excess detergent concentration in Step 1 or a heavy contamination load in the circuit. In the latter case, a second full detergent soak should be performed before rinsing is repeated. Optishield should not be substituted with alternative coolant additives. Many commercially available additives are incompatible with the aluminium alloys used in the laser head and the chiller heat exchanger. An incompatible additive can accelerate corrosion and cause irreversible damage. The manufacturer’s recommended concentration ratio for Optishield should be followed precisely, as both under-concentration and over-concentration reduce its effectiveness as a biocide and corrosion inhibitor.

Data Accessibility

The data shown in this thesis is archived at **\UTHD-Members\Amit Haldar (PhD 2021-2026)\My Thesis** in the UTHD group's internal server. The folder is organized according to the Chapters of this thesis. All data supporting the findings of this thesis are available from the author upon reasonable request.

Amit Haldar

PhD Candidate

amit.haldar@niser.ac.in | (+91) 9163590924 | Google Scholar | LinkedIn

Research Profile

My doctoral research centred on THz metamaterials, with a focus on strong light-matter coupling and the nonlinear dynamics that follow on ultrafast timescales. The work moved through design, fabrication, and spectroscopic characterisation as a single cycle, with each step feeding the next. A large part of the effort went into building the THz spectroscopy laboratory at NISER from scratch. The facility supports THz time domain spectroscopy, optical pump-THz probe measurements, and two-dimensional THz spectroscopy, all built around a Coherent Astrella laser. On the design side, I use CST and COMSOL for full-wave electromagnetic simulation, together with density matrix modelling to capture the coupled quantum response.

Education

Ph.D. in Physics | Supervisor: Prof. Shovon Pal — Jan 2021 – May 2026
School of Physical Sciences, NISER, HBNI — Odisha, India
Thesis: *Strong Coupling Effects and Nonlinear Dynamics in a THz-EIT Metamaterial*

M.Sc. in Physics — Jun 2017 – Jun 2019
Jawaharlal Nehru University (JNU) — New Delhi, India

B.Sc. in Physics — Jun 2014 – Jun 2017
Asutosh College, University of Calcutta — West Bengal, India

Professional Experience

R&D Engineer — May 2026 – Present
TeraLumen Solutions (India's first THz hardware startup) — India

- THz instrumentation development: system architecture, feasibility analysis, and leading next-generation compact THz-TDS platform development.

Doctoral Researcher — Jan 2021 – May 2026
Ultrafast THz Dynamics Lab, NISER — Odisha, India

- Designed, fabricated (Heidelberg DWL maskless lithography), and characterised split-ring-resonator metamaterial arrays for THz-EIT studies.
- Built the complete THz spectroscopy infrastructure from scratch: THz-TDS, Optical-pump THz-probe, and 2D THz-TDS around a Coherent Astrella system.
- Demonstrated phonon-polariton-mediated dual EIT in the strong-coupling regime using perovskite-coupled metamaterials.
- Mapped nonlinear dynamics of EIT metamaterials using 2D THz spectroscopy, extracting dephasing/relaxation timescales via coupled-oscillator and Lindblad density-matrix models.
- Developed Python analysis: Different conductivity fitting model, Tinkham thin-film analysis, and 2D Fourier spectroscopy.
- Full-wave electromagnetic simulations (CST Microwave Studio, COMSOL RF Module).

Publications

First Author / Co-first Author

1. **A. Haldar**, S. Prabhu, and S. Pal, "Unveiling Nonlinearities of Electromagnetically Induced Transparency in a THz Metamaterial," *Advanced Functional Materials*, e75422, 2026.
2. **A. Haldar***, K. V. Goyal*, R. V. Puranik, V. Dwij, S. Maity, K. R. Khator, S. Ghosh, B. S. Chouhan, G. Kumar, S. P. Senanayak, S. Prabhu, and S. Pal, "Phonon-Polariton Mediated Dual Electromagnetically Induced Transparency in a THz Metamaterial," *Advanced Quantum Technologies*, e00368, 2025. (*equal contribution)

Contributing Author

3. A. Dutta, P. Shee, **A. Haldar**, S. Pal, "2D-THz Spectroscopy: Exploring Nonlinear Dynamics in Quantum Materials," *J. Phys.: Condens. Matter*, 37(20), 203002, 2025.
4. K. Mondal, **A. Haldar** et al., "Enhanced Femtosecond Nonlinear Optical Susceptibility and THz Conductivity in $MoSe_2$–Noble Metal Nanocomposites," *Adv. Opt. Mater.*, 12(23), 2401138, 2024.
5. B. S. Kumar, B. Pal, Y. Potla, **A. Haldar** et al., "Structural Reorganization Drives Exciton Relaxation Pathways in Layered 2D Ruddlesden–Popper," *Small*, e09142, 2026.
6. K. R. Khator, D. Acharejee, **A. Haldar** et al.,"Nanoscale Facet Engineering Stabilizes α-$FAPbI_3$ and Suppresses Ion Migration to Realize Ambient Stable Perovskite Transistors," *Small*, e00022, 2026.

Conference Proceedings

7. **A. Haldar**, J. Li, C.-J. Yang, K. Saha, and S. Pal, "Carrier Dynamics and Transport Properties of Ge using Optical–Pump Terahertz–Probe Spectroscopy," *Frontiers in Optics*, JW5A.48, Optica Publishing Group, 2024.

Under Review

8. K. Mondal, **A. Haldar** et al.,"Intensity-Driven Mott-like Transition in a 2D Ruddlesden–Popper Perovskite," (under review, *Small*).

Technical Skills

Experimental: THz-TDS, 2D THz-TDS, Optical-pump THz-probe spectroscopy, maskless photolithography (Heidelberg DWL), liftoff, cryogenics, Z-Scan
Simulation: CST Microwave Studio (frequency/time-domain), COMSOL Multiphysics (RF Module)
Programming: Python, MATLAB, LabVIEW, LaTeX

Supervision & Mentoring

Kshitij V. Goyal – Strong-coupling-mediated EIT in metamaterials (M.Sc. thesis); *now PhD, EPFL* 2023–2025
Swayam Panda – Excitonic dynamics in 2D perovskites via OPTP & Z-Scan (M.Sc. thesis); *now PhD, U. Luxembourg* 2024–2025
Soumya P. Jena – Magnon dynamics in THz metamaterial systems (M.Sc. thesis, ongoing) 2024–present

Honours & Awards

HBNI Travel Grant (Boston) | Career Accelerator Grant (Washington) 2025
Outstanding Poster Award, Ultrafast Optical Phenomena, FiO+LS (top 6 of all presenters) 2024
FiO+LS Incubic Milton Chang Travel Grant (awarded to 6 participants) 2024
CSIR-UGC JRF: All-India Rank 306 / 28 135 2022
JEST: All-India Rank 211 / 13 489 2020
Merit-cum-Means Scholarship, Jawaharlal Nehru University 2017–2019

Service & Leadership

President, Optica Student Chapter, NISER 2024–2025
Core Organizer, Ultrafast Sciences (UFS) 2024, NISER 2024

Languages

English (professional) | Bengali (native) | Hindi (fluent)

References

Prof. Shovon Pal
Reader-F, NISER,
Bhubaneswar, India
shovon.pal@niser.ac.in

Prof. Shriganesh Prabhu
Senior Professor, TIFR,
Mumbai, India
prabhu@tifr.res.in

Prof. Satyaprasad P. Senanayak
Reader-F, NISER,
Bhubaneswar, India
satyaprasad@niser.ac.in